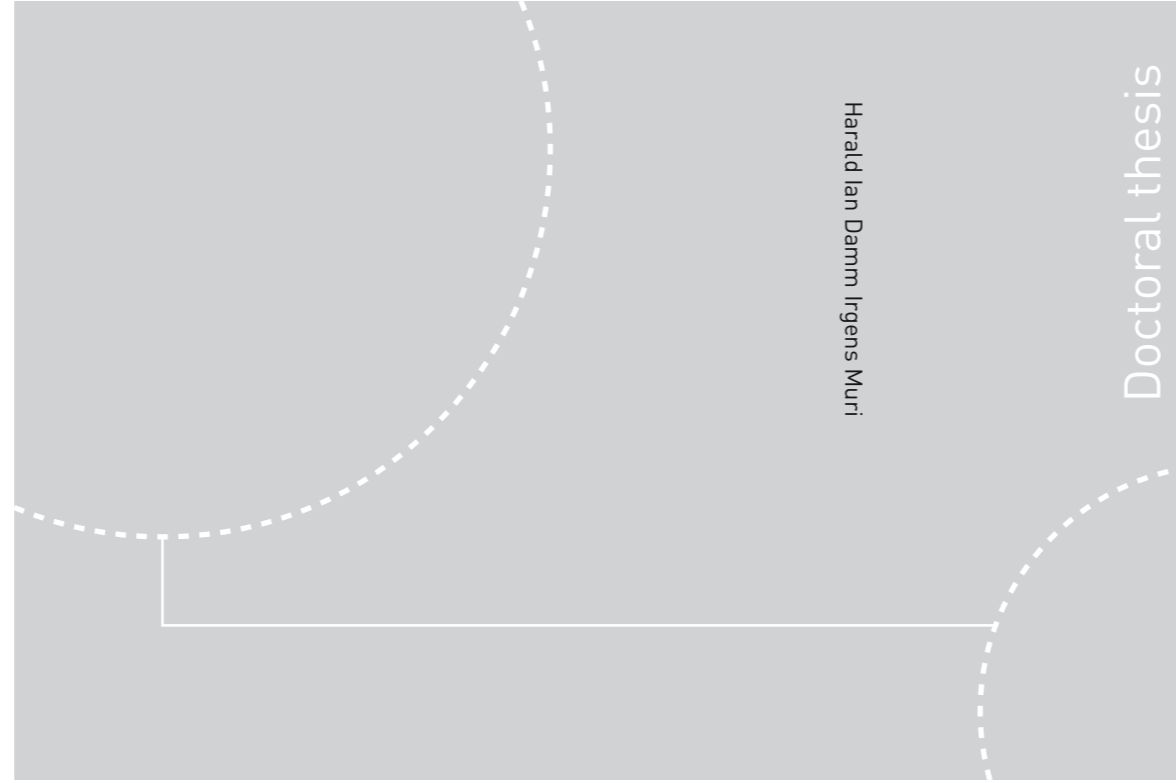


ISBN 978-82-326-3572-6 (printed ver.)
ISBN 978-82-326-3573-3 (electronic ver.)
ISSN 1503-8181



Harald Ian Damm Irgens Muri

Doctoral thesis

Doctoral theses at NTNU, 2018:392

Harald Ian Damm Irgens Muri

Novel Fiber Optic Biosensors Based on Nanoplasmonic and Interferometric Modalities



Norwegian University of
Science and Technology



Doctoral theses at NTNU, 2018:392

NTNU
Norwegian University of Science and Technology
Thesis for the Degree of
Philosophiae Doctor
Faculty of Information Technology and Electrical
Engineering
Department of Electronic Systems



Norwegian University of
Science and Technology

Harald Ian Damm Irgens Muri

Novel Fiber Optic Biosensors Based on Nanoplasmonic and Interferometric Modalities

Thesis for the Degree of Philosophiae Doctor

Trondheim, December 2018

Norwegian University of Science and Technology
Faculty of Information Technology and Electrical Engineering
Department of Electronic Systems



Norwegian University of
Science and Technology

NTNU

Norwegian University of Science and Technology

Thesis for the Degree of Philosophiae Doctor

Faculty of Information Technology and Electrical Engineering
Department of Electronic Systems

© Harald Ian Damm Irgens Muri

ISBN 978-82-326-3572-6 (printed ver.)
ISBN 978-82-326-3573-3 (electronic ver.)
ISSN 1503-8181

Doctoral theses at NTNU, 2018:392

Printed by NTNU Grafisk senter

Abstract

New and improved monitoring of complex multivariable environments often relies on the diversity and implementation of new sensor technologies. Before and after the worldwide recession, the sensor market showed to have a growth around 10% per year. This suggests that there is a substantial need of tools for real-time detection of various chemical compounds and biochemical entities in various applications. These application areas may be as diverse as monitoring of energy storing or energy production processes, monitoring of biohazard or human-made chemical contaminants, or monitoring of biomarkers for medical diagnostics and treatments. Different types of sensors are often made for specific applications in mind such as to work in high temperatures, in corrosive environments, or with the possibility for miniaturization. Biochemical sensor development is often driven by certain functionalities such as label-free, selective and high sensitivity sensing with possibilities for miniaturization to obtain fast diffusion times and sensor response. Optical fiber (OF) based waveguide sensors have shown to be a popular platform for miniaturization with possibility for sensor insertion into small volumes, tissues or vessels. Also, the sensing with OFs can be multiplexed by using the free-variables of light properties of frequency, amplitude, phase, and polarization.

This thesis presents novel fiber optic (FO) sensor architectures based on interferometric or localized surface plasmon resonance (LSPR) modalities for multianalyte label-free sensing at a single point. The sensor consists of a stimuli-responsive hydrogel that represents a low-finesse Fabry-Perot (FP) cavity embedded with noble metal nanoparticles (NMNP) that exhibit LSPR. The sensing modalities were interrogated in reflection by spectroscopic measurements in visible (VIS) and infrared (IR) light frequencies. The interferometric sensing was performed by detecting chemically induced length changes of the FP cavity from the phase change measurements of the sinusoidal spectra in IR light frequencies. The LSPR sensing was performed by detecting the change in the local refractive index (RI) on the NMNP surfaces from the resonance frequency change measurements of the Lorentzian spectra in VIS-IR light frequencies. Proof-of-concept demonstrations of the FO sensor system show that the LSPR wavelength changes of the NMNP for deswelling hydrogels were dominated by local RI variations for low number densities (ND), while for high NDs, the LSPR wavelength changes for deswelling hydrogels were dominated by plasmon coupling. The interferometric sensor was negligibly influenced by the NDs used with a signal and a response comparable to previous work. At optimized NDs, the LSPR wavelength changes were small for gold nanorods (GNR) in different hydrogel swelling equilibriums, whereas for receptor-analyte recombinations on the GNR surface significant LSPR changes were observed. The proof-of-concept sensor systems presented in this thesis introduces some general aspects for obtaining multiparameter sensing in a single point as well as models for understanding the response of the sensing modalities. With further optimization, the FO designs may prove to be a highly selective, sensitive and a fast label-free monitoring device of specific biomarkers for biological or medical applications.

Acknowledgement

The work in this thesis has been carried out at the Department of Electrical Systems, from 2013 to 2018, at The Norwegian University of Science and Technology (NTNU), Trondheim, Norway, in the photonics lab of Professor Dag Roar Hjelme. I am grateful for the financial support received from NTNU, the Energy and Sensor Systems group (ENERSENSE), as well as for the external financial support from Interreg, the EU funded Sweden-Norway program that promotes social and economic integration across borders through regional cooperation.

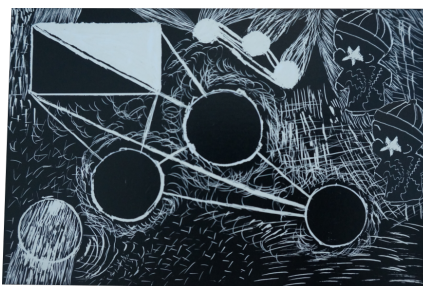
I want to primarily thank my supervisor Professor Dag Roar Hjelme for letting me carrying out this work in his laboratory. My constant progress in this study was greatly ensured by his teachings, motivation and encouraging supervision. I also want to thank him for introducing me to very fascinating research environments and entrepreneurship both in Norway and abroad as well as for the attendance we had in fascinating and inspirational conferences. If the reader were looking for projects in photonic systems, I would highly recommend you to get in contact with Prof. Hjelme. I want to further direct a special thanks to the following; my co-supervisor Professor Astrid Aksnes for introducing me to her photonic group, sharing her knowledge in photonic biosensing, and for lending me her book for 4 years; the table-fussball champion Markus Wahl for our constructive collaboration and discussion in making revolutionary sensor technologies, and for proofreading my thesis; søta bror Krister Hammarling and his group in Mid-Sweden University for our extremely efficient research activities and discussions in Trondheim and Sundsvall; the mountain Dr. Jacob Lamb for sharing very helpful insight into biosensing in efficient energy production and for proofreading my thesis; the instrumental genius Dominik Osinski for your work in promoting efficient use of the National Instruments toolkits in laboratory work.

The time at Kalvskinnet-IES and at Gløshaugen-IES has been an effective and exciting experience with very exciting conversations, fascinating research and priceless laughter. The latter I think has been quite critical to overcome the hair-tearing situations that often occur in PhD studies. For the vast social activities and the outstanding positive vibes I want to thank my fellow table-fussball-mates in the ENERSENSE group, Markus Wahl, Jacob Lamb, Dominik Osinski, Robert Bock, Kjersti Krakhella, Zohreh Jalili, Felix Kelberlau, Laura Feliuss, Sayed Hashemi, Ellen Skilbred, Yash Raka, Ailo Aasen, Shiplu Sarker, Md Hujjatul Islam and the leader of ENERSENSE group, Professor Odne Burheim, for spending enormous effort in bringing different science fields together as well as for conducting collaborative, cross-disciplinary research activities with the aim of making the world renewable again. I would also like to thank the masterstudents involved in this project, Andon Bano and Pål Langø. It has been a pleasure working with you, and I hope this experience has spread the passion for photonics into a wider periphery. Furthermore, I would like to acknowledge the cellular and molecular imaging core facility (CMIC) at NTNU for the access to their facilities and the accommodating staff. I would like

to direct special thanks to the Senior-Engineer Linh Hoang at CMIC for very helpful support in developing preparation methods for characterizing hydrogels in electron microscopes.

I am forever grateful for the support that I have received from my family. Thank you father Harald, mother Grete and my sisters, Ina and Henriette (with Knut), for showing patience during my school years (as I instead wanted to go skiing or play in rock-bands instead of listening to the monotonous teachers) and supporting greatly everything that I do with my life without having any doubts. Without your endless support I would not be where I am today. I would also like to thank my friends, traveling long distance, as well my close friends here in Trondheim for letting me disconnect from PhD studies by making me experience Låftene at Samfundet again or by taking me out to dark, bright or blurred concerts, festivals, swimming pools, cabins in the mountains or deep into the steep fjords and other recreational jests.

Finally yet importantly, I want to express absolute gratitude to my wife **Tatyana Sherstova**, and to my two sons **Leo Loki** and **Miron Bor** for making my life perfect and complete. You are all I have ever wanted, and this thesis is definitely dedicated to you. Thank you Tatyana (pictured as a cat in the left image below that she made herself) for being a cool cat during this last hectic year, for being a supermom taking care of two kids when I was constrained to finish the thesis, being my best friend, being my wise yoga teacher and most importantly, thank you for being my wife! я тебя люблю. Thank you Miron and Leo (pictured in the right image below made by me) for giving me healthy distractions, seeing the world from your perspective with curious and brand new eyes, making me believe that the need for sleep is nothing but an illusion and for making me smile and laugh everyday that shaped my PhD experience as a joyful ride. I hope that one day; you will understand why your father would pursue something self-destructing but extremely rewarding and passionate work as the PhD studies are.



” *My goal is simple. It is a complete understanding of the universe, why it is like it is, and why it exists at all.*

— **Stephen Hawking**

Stephen Hawking passed away around the same time as this thesis was submitted. His famous book "A Brief History of Time" was important for the initiation of my glowing interest in science and technology during my high school studies.

List of Papers

The following publications are included in this thesis:

- (I) **LSPR Coupling and Distribution of Interparticle Distances between Nanoparticles in Hydrogel on Optical Fiber End Face**
Muri, H.I.D.I., and Hjelme, D.R.
Sensors, 2017, 12, 2723.
Harald Ian Muri and Dag Roar Hjelme conceived and designed the experiments; Harald Ian Muri performed the experiments; Harald Ian Muri and Dag Roar Hjelme analyzed the data; Harald Ian Muri and Dag Roar Hjelme wrote the paper. All authors contributed in the revision of the paper.
- (II) **A Single Point, Multi-Parameter, Fiber Optic Sensor Based on a Combination of Interferometry and LSPR**
Muri, H.I.D.I., Bano, A. and Hjelme, D.R.
Journal of Lightwave Technology, 2018, 36, 4
Harald Ian Muri, Andon Bano and Dag Roar Hjelme conceived and designed the experiments; Harald Ian Muri and Andon Bano performed the experiments; Harald Ian Muri, Andon Bano and Dag Roar Hjelme analyzed the data; Harald Ian Muri and Dag Roar Hjelme wrote the paper. Harald Ian Muri and Dag Roar Hjelme contributed in the revision of the paper.
- (III) **LSPR and Interferometric Sensor Modalities Combined Using a Double-Clad Optical Fiber**
Muri, H.I.D.I., Bano, A. and Hjelme, D.R.
Sensors, 2018, 1, 187.
Harald Ian Muri, Andon Bano and Dag Roar Hjelme conceived and designed the experiments; Harald Ian Muri and Andon Bano performed the experiments; Harald Ian Muri, Andon Bano and Dag Roar Hjelme analyzed the data; Harald Ian Muri and Dag Roar Hjelme wrote the paper. Harald Ian Muri and Dag Roar Hjelme contributed in the revision of the paper.
- (IV) **Mapping the Distribution of Particles in Hydrogel in Use for Nanoplasmonic Biosensors: A Comparison of Preparation Methods**
Muri, H.I.D.I., Hoang, L. and Hjelme, D.R.
Manuscript
Harald Ian Muri, Linh Hoang and Dag Roar Hjelme conceived and designed the experiments; Harald Ian Muri and Linh Hoang performed the experiments; Harald Ian Muri, Linh Hoang and Dag Roar Hjelme analyzed the data; Harald Ian Muri, Linh Hoang and Dag Roar Hjelme wrote the paper.

Conference Papers

1. **Novel localized surface plasmon resonance based optical fiber sensor**
Muri, H.I.D.I., and Hjelme, D.R.
SPIE Proceedings, 2016, 9702.
2. **First step towards an interferometric and localized surface plasmon fiber optic sensor**
Muri, H.I.D.I., Bano, A. and Hjelme, D.R.
Optical Fiber Sensors Conference (OFS), 2017 25th, 2017, 1032323 .
3. **Interferometric and localized surface plasmon based fiber optic sensor**
Muri, H.I.D.I., Bano, A. and Hjelme, D.R.
SPIE Proceedings, 2017, 10058.
4. **Dual parameter fiber optic sensor combining a Fabry-Perot and a Mach-Zehnder interferometer**
Hammarling, K., Muri, H.I.D.I., Wahl, M., Engholm, M. and Hjelme, D.R.
2017 IEEE SENSORS Conference, 2017.

Conference Abstracts

1. **A combined glucose and pH sensor on a single optical fiber for continuous point-of-care testing**
Hammarling, K., Muri, H.I.D.I., Wahl, M., Engholm, M. and Hjelme, D.R.
SPIE Conference, Photonic West, 2018, Optical Fibers and Sensors for Medical Diagnostics and Treatment Applications XVIII, Session 3: Sensors Detectors and Treatment Tools II, 10488-9.

Contents

Abstract	i
Acknowledgement	iii
List of Papers	vii
Contents	ix
List of Abbreviations	xi
1 Introduction	1
1.1 Aim of Thesis	2
2 Background	5
2.1 Sensors Based on Optical Fiber Systems	6
2.1.1 Modefields in Optical Fibers	7
2.1.2 Intrinsic Fiber Optic Sensor	10
2.1.3 Extrinsic Fiber Optic Sensor	13
2.2 Nanoparticles and Hydrogels for Label-Free Sensing	16
2.2.1 Noble Metal Nanoparticles	17
2.2.2 Hydrogels	18
2.3 Fabry-Perot Interferometers	20
2.3.1 Hydrogel – A Micro Fabry-Perot Cavity	20
2.3.2 Interpretation of an Interferometric Signal	22
2.3.3 Sensor Implementation with Single-Mode Optical Fiber	24
2.4 Nanoplasmonic Systems	26
2.4.1 Gold Nanoparticle – A Nano-Probe Sensing the Refractive Index	27
2.4.2 Dipole-Dipole Coupling	31
2.4.3 Change in the Metal Dielectric Function	33
2.4.4 Interpretation of a Plasmon Resonance Signal	35
2.4.5 Sensor Implementation with Multi-Mode Optical Fiber	36
2.5 Multiparametric Sensor Implementation	38
2.5.1 Distribution of Particles in Hydrogel	39
2.5.2 Refractive Index For a Contracting Hydrogel	40
2.5.3 Sensor Implementation with a Double-Clad Optical Fiber	42

2.6	Characterizing Origin of Observed Signals	44
2.6.1	Model for Particle Distributions in Hydrogel	44
2.6.2	Hydrogel and Electron Microscopy – A Few Remarks	45
3	Summary and Discussion of Papers	49
3.1	Summary	49
3.1.1	Paper I	49
3.1.2	Paper II	50
3.1.3	Paper III	51
3.1.4	Paper IV	52
3.2	Discussion	53
4	Conclusion and Outlook	59
	References	63
	Papers	73
	Paper I	73
	Paper II	95
	Paper III	107
	Paper IV	125

List of Abbreviations

BSE	backscattering electrons
CF	confinement factor
CID	chemical interface damping
CPD	critical point drying
DCOF	double-clad optical fiber
DDA	discrete dipole approximation
e-e	end-to-end
EFPI	extrinsic Fabry-Perot interferometer
FBG	fiber Bragg gratings
FIB-SEM	focused ion beam-scanning electron microscope
FO	fiber optic
FOM	figure of merit
FP	Fabry-Perot
FSR	free spectral range
FWHM	full width at half maximum
GNP	gold nanoparticle
GNR	gold nanorods
HMDS	hexamethyldisilazane
IFPI	intrinsic Fabry-Perot interferometer
IR	infrared
LIGO	laser interferometer gravitational-wave observatory
LOD	limit of detection
LP	linear polarized
LPFG	long period fiber gratings
LSPR	localized surface plasmon resonance
ME	Maxwells equations
MM	multi-mode
ND	number density
NMNP	noble metal nanoparticles
NMNS	noble metal nanostructures
NNDF	nearest-neighbor distribution function
OF	optical fiber
PEG	polyethylene glycol
PLE	plasmon ruler equation
RI	refractive index
s-s	side-by-side
SBFSEM	serial block-face scanning electron microscopy
SE	secondary electrons
SEM	scanning electron microscopy
SERS	surface enhanced raman scattering
SM	single-mode
SPP	surface plasmon polaritons
SPR	surface plasmon resonance

TE	transverse electric
TELM	transmission electron microscopy
TEM	transverse electromagnetic
TFBG	tilted fiber Bragg gratings
UV	ultra-violet
VIS	visible

Introduction

1

There is a tremendous need for tools for real-time monitoring of various chemical and biochemical entities in different application areas. The application areas are as diverse as monitoring of biohazardous entities, human-made chemical contaminants, energy storing or energy production processes, or monitoring for medical diagnostics and treatment. This demand for sensor technologies can be reflected from the worldwide recession, where the sensor market happened to be unaffected, with a continual growth around 10% a year [1]. Controlling and regulating complicated chemical processes may improve and open up new possibilities in many areas such as increasing the life cycle of commercial hydrogen fuel cells, efficient energy production from waste, or faster treatment methods for patients in intensive care units. Optical microscope techniques are among the most powerful methods used to identify and quantify the presence of specific molecules in complex fluid environments. These techniques are so far not directly applicable to real-time monitoring or for monitoring outside the laboratory setting. Optical waveguides or electrical sensors may offer the unique features required for highly specific and precise measurements in the field and point-of-monitoring settings.

The monitoring of complex multivariable environments often relies on the diversity and the implementation of new sensor technologies. The sensor is often designed as defined by the application in mind with requirements such as fast response times, high selectivity, robustness, multiplexing possibilities, remote sensing possibilities, label-free chemical sensing, or possibility for miniaturization. A library of sensor designs is thus useful for finding balanced solutions between the minimum requirements needed and the cost-effectiveness. For biochemical sensors, miniaturization is a vital objective since smaller size leads to fast diffusion times and fast sensor response. For medical applications, miniaturization enables sensor insertion into small sample volumes, tissue or vessels. The drive from objectives such as miniaturization, label-free sensing, multiplexing possibilities and remote sensing capabilities, has led into the development of light-waveguide platforms in a various configuration such as lab-on-a-chip [2], or distributed fiber optic (FO) sensors [3]. Optical fiber (OF) waveguides in particular, prove to be a popular technology platform concerning remote sensing capabilities, label-free sensing and miniaturization [4]–[9]. OF based sensors are also immune to electro-magnetic interference and can monitor in high temperatures or corrosive environments. The light-matter interactions in the sensor integrated on the OF can be measured as a function of amplitude, frequency, polarization or phase. Hence, the modulation of

light properties offer many possibilities for signal multiplexing that can be applied for multiparametric sensing in complex multivariable environments.

The applications of a FO waveguide is defined by size, capability for remote sensing, multiplexed sensing, or defined by the capability of being inert in different environments. Establishing the sensor on the OF end face removes the possibility for distributed sensing, but several parameters can be combined in a single point as demonstrated in [6], [8], [9]. Such types of miniaturized OF sensors offer point-of-monitoring (not specifically medical applications) and may become an important technology platform in both research and industry. Stimuli-responsive hydrogels have been synthesized for various applications but few have been used for label-free biosensing due to the limited sensitivity offered by the interrogation techniques available [10]–[12]. A prime example of OF waveguides as a tool to solve this issue has been demonstrated in [13], which can be customized for a range of applications. The length determinations of responsive gels with OFs have shown to obtain resolutions as low as in the nm range [5].

The use of localized surface plasmon resonance (LSPR) in noble metal nanoparticles (NMNP)s are also promising candidates for label-free sensing since they have fast response times, high sensitivity, and high selectivity [14]. Biofunctionalization of NMNP surfaces is simple and can be used for detecting receptor-analyte recombinations. The label-free sensing of analytes can, in addition, be multi-parametric by resolving the different LSPR observed for NMNP of different size and shapes [9], [15]. This thesis focuses on utilizing stimuli-responsive hydrogels and LSPR of NMNPs with FO architectures for label-free sensing applications demonstrated in proof-of-concept experiments. The proof-of-concept sensor systems are timely demonstrated and limited to laboratory tests without having to use resources to optimize the materials for one specific application in mind. By conducting sensor experiments in this manner, it is possible to understand the fundamental origin and features for the interferometric and LSPR sensing modalities.

1.1 Aim of Thesis

This thesis aimed to develop new and innovative FO architectures in reflection for label-free sensing of specific molecular entities. The FO sensor systems were based on using stimuli-responsive hydrogels and based on using LSPR of NMNPs as continued development of the OF sensors constructed in [13].

The secondary objectives used for reaching the overall objective above can be itemized as follows:

- Develop, demonstrate, and characterize LSPR based OF sensor in reflection by using NMNPs embedded in hydrogel immobilized on the OF end face.

- Explore the features of the LSPR sensing modality concerning inducing plasmon coupling or inducing changes in the local refractive index (RI) on the NMNP surfaces and establish a model from the results obtained.
- Investigate the influence of MNPs on the extrinsic Fabry-Perot interferometer (EFPI) FO sensor developed in [13] and develop an FO architecture combining interferometric and LSPR sensing modalities.
- Characterize and demonstrate the FO sensor in reflection mode that combines the interferometric and LSPR sensing modalities as well as establishing a model for the observations made.
- Understand the LSPR response of the proof-of-concept sensor systems from the characterization of NMNP distributions in the hydrogel.

The following chapter presents the theoretical background necessary for discussing the results obtained in this work. The background chapter presents modefields in OFs, extrinsic or intrinsic FO systems, label-free sensing with hydrogel and MNPs, Fabry-Perot (FP) interferometers, the theory of nanoplasmonic systems, particle distribution functions, and implementation challenges concerning the utilization of plasmonic or interferometric sensor systems. Subsequently, the publications included in this thesis are summarized and discussed. The summary and discussion are presented given the aims above and relates the different papers to one another. The papers are not listed chronologically concerning publication date. To make it easier to follow the ideas presented in the summary and discussion, the papers are presented in a sequence that is the most intuitive for the reader. The last chapter contains the conclusion and outlook of the results and discussion presented in this thesis. This chapter is more subjectively presented concerning what the author of this book thinks about the contemporary development in this field as well as concerning some ideas that could lead to new exciting research questions.

New sensor systems offer new possibilities for fast, selective, sensitive and robust monitoring of different types of environments. Sensors can be defined as self-contained devices capable of providing real-time analytical information by recognizing and detecting physical or chemical quantities. The recognition of force, pressure, temperature, pH, ionic strength, or biomolecules are converted into a signal (electrical, optical, or mechanical) by a transducer that can be quantized by a detector. The signal detection can be either passive or active. Active sensing utilizes an excitation signal to detect physical or chemical entities whereas passive sensing omits the excitation signal. The drive for developing new sensor technologies is often based on the possibility for miniaturization, to work in harsh environments (e.g., corrosive, temperature, pressure, and intense electromagnetic fields), or the possibility for remote sensing. This has led to the development of light-waveguide platforms in various configurations such as the lab-on-a-chip [2] or distributed FO sensors [3].

OF waveguides prove to be a popular technology platform for developing miniaturized sensors in remote sensing settings [4]–[7]. The general components of OF sensor systems in transmission or reflection can be illustrated as shown in Fig. 2.1. OF sensors are usually configured for active sensing where the source

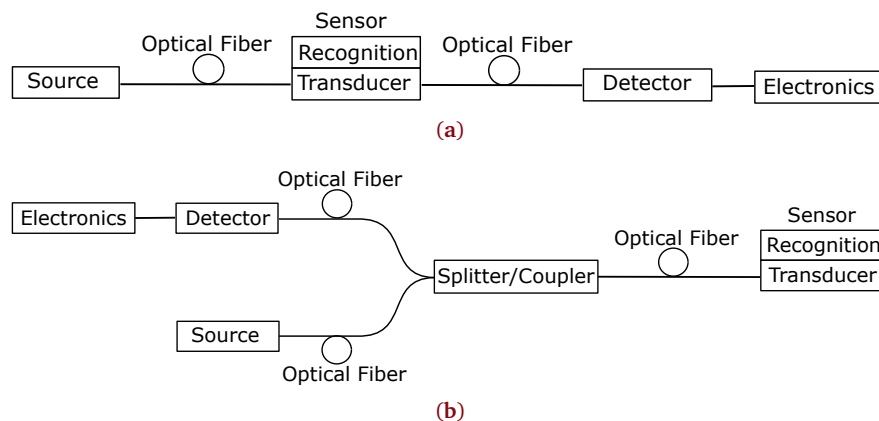


Fig. 2.1: (a) General components of OF sensors in transmission; (b) General components of OF sensors in reflection.

is producing the excitation signal composed of coherent or incoherent, narrow

or broadband light-frequencies. The excitation signal or light properties can be modulated for amplitude, frequency, polarization or phase. Thus, the utilization of light as the excitation signal offers numerous ways for signal multiplexing with possibilities for multiparametric sensing in complex environments. The transducer based on light-material interactions converts the recognition of a physical or chemical quantity. The sensor (recognition and transducer) can be based on OF components such as fiber Bragg gratings (FBG) [16], long period fiber gratings (LPFG) [17] or nanostructured noble metals on OF side or end face [7], [18]. Changes in the light-material interactions in the OF sensor is measured by the detector (e.g., spectroscopic, polarimetry, interferometric, or changes in intensity) that is controlled by electronics. For OF sensors in transmission shown in Fig. 2.1(a), light is guided by OF from source to sensor to the detector. For OF sensors in reflection (as shown in Fig. 2.1(b)), light is guided by OF from the source to the splitter/coupler to the sensor and back to the splitter/coupler and then to the detector. The splitter is based on integrated waveguides on a substrate whereas couplers are based on fusing OF cores together, so the light is coupled between the two fibers. Some losses are thus involved by using splitters or couplers for OF sensor systems in reflection.

This chapter presents the sensing modalities used in this project as well as the theoretical background for discussing the results obtained in Chapter 3. Selected FO sensor systems are also presented to demonstrate the extrinsic or intrinsic transduction methods. Furthermore, different types of OF sensor systems are proposed concerning single or multiparametric sensing based on interferometric and nanoplasmonic modalities as well as the sensor functionalities that follows with them. Lastly, a few remarks are mentioned concerning the challenges of preparing sensor materials such as hydrogels embedded with NMNP for electron microscopy since the distributions of NMNPs in hydrogels are partly defining their nanoplasmonic sensor response.

2.1 Sensors Based on Optical Fiber Systems

The monitoring of complex multi-variable environments often relies on the diversity and the implementation of new sensor technologies. Active and passive electrical sensors are continually under development and used in many ways such as for internet-of-things, in smart phones, in computers, in cars and more. Some applications require the sensor system to perform in harsh environments or to be miniaturized. For biochemical sensors, miniaturization is an essential objective as it can be inserted into small sample volumes, tissue or vessels. The functionality of a miniaturized sensor is improved since small size leads to fast diffusion times and fast sensor response [19]. Light confined by waveguides such as OFs is a popular technology platform for developing miniaturized sensors [4]–[7]. Also, to

being immune to electro-magnetic interference, OF sensors can be used in high temperatures and corrosive environments [3], [16].

The recognition of an element converted into a signal by the transducer (see Fig. 2.1) in an optical sensor is based on modulating one or several light properties such as amplitude, frequency, polarization or phase. How light interact with materials can, therefore, be measured by using spectroscopy, polarimetry, interferometry or measured as a function of intensity. In this thesis, spectroscopy and interferometric methods have been used to obtain characteristic reflection signatures of light-matter interactions as well as the phase difference of light by using extrinsic FO sensors. In the following Section 2.1.1, the mode-fields in waveguides are described in such a detail that serves as a foundation for the FO systems presented in this thesis and for the selected FO sensors examples presented in Section 2.1.2 and 2.1.3.

2.1.1 Modefields in Optical Fibers

The light properties of dielectric waveguides can be well described by using Maxwells equations (ME). Light can be expressed as a transverse electromagnetic (TEM) plane wave that creates charges and currents when propagated in dielectric or metal media. The sum of several TEM waves in a dielectric slab can be represented as a total electromagnetic field. The electric and magnetic field vectors for charges and currents in position and time arising from the total electromagnetic field is thus solved by using the ME. For a planar dielectric slab with separation, d , and with RI as, n_1 and n_2 , shown in Fig. 2.2, the total internal electric-field complex amplitude with propagation constant, $\beta_m = n_1 k_0 \cos \theta_m$ and wavelength λ_0 can be expressed as [20]

$$E_x(y, z) = a_m u_m(y) \exp(-i\beta_m z) \quad (2.1)$$

where

$$u_m(y) \propto \begin{cases} \cos(k_T y), & m = 0, 2, 4, \dots \\ \sin(k_T y), & m = 1, 3, 5, \dots \end{cases} \quad (2.2)$$

Here $k_T = \sqrt{n_1^2 k_0^2 - \beta_m^2} = \frac{2\pi}{\lambda} \sin \theta_m$, $-\frac{d}{2} \leq y \leq \frac{d}{2}$, $\lambda = \frac{\lambda_0}{n_1}$, $k_0 = \frac{2\pi}{\lambda_0}$, a_m is a constant, and θ_m is the traveling angles at the modes m . The internal field in medium n_1 from (2.2) is illustrated in Fig. 2.3. The bounce angles, θ_m , will only exist between 0 and the critical angle for total internal reflection, θ_c . In this approach, the self-consistency condition¹ is used to determine the bounce angles of the waveguide modes with appropriate boundary conditions for the inner and outer media. For each reflection in the slab, there will be a phase shift as a function of the angle θ and polarization, which represents an additional traveling distance. By estimating the field confinement in the slab, it is possible to estimate the phase shift or additional

¹a wave reproduces itself after each round trip.

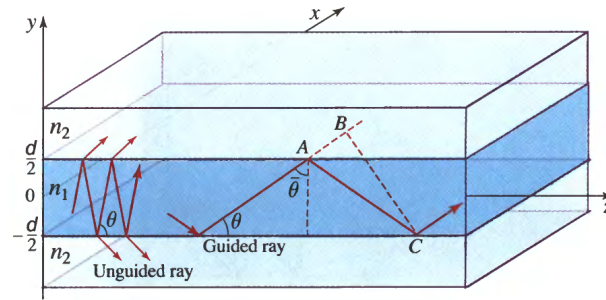


Fig. 2.2: Light guided by a planar dielectric slab with incident angles smaller than the critical angle for total internal reflection. The illustration is from [20].

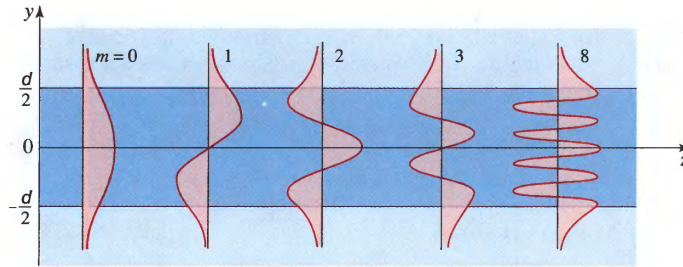


Fig. 2.3: Internal and external field distributions of the transverse electric modes guided by a planar dielectric slab. The illustration is from [20].

traveling distance for each reflection in the dielectric slab. The external field in medium n_2 as illustrated in Fig. 2.3 can be described as

$$u_m(y) \propto \begin{cases} \exp(-\gamma_m y), & y > d/2 \\ \exp(\gamma_m y), & y < -d/2 \end{cases} \quad (2.3)$$

where $\gamma_m = \sqrt{\beta_m^2 - n_2^2 k_0^2}$ is the extinction coefficient [20]. The total electric field in Fig. 2.3 for an arbitrary TEM plane wave guided in the dielectric slab would represent a superposition of its modes $m = 0, 1, 2, \dots$. The ratio of the power in the slab to the total power is often known as the confinement factor (CF).

The CF and number of modes in a waveguide are highly dependent on its size and geometry. For plane dielectric waveguides the number of modes for the transverse electric (TE) wave is, $M = \frac{2d \text{NA}}{\lambda_0}$, where, $\text{NA} = \sqrt{n_1^2 - n_2^2}$, is the numerical aperture [20]. The conditions for guiding one or several modes is then found by choosing, $1 < M < 2$, or, $M > 1$, respectively. For three-dimensional waveguides as shown in Fig. 2.4, the effects from meridional and skewed rays have to be taken into account. For an OF, the TEM plane wave

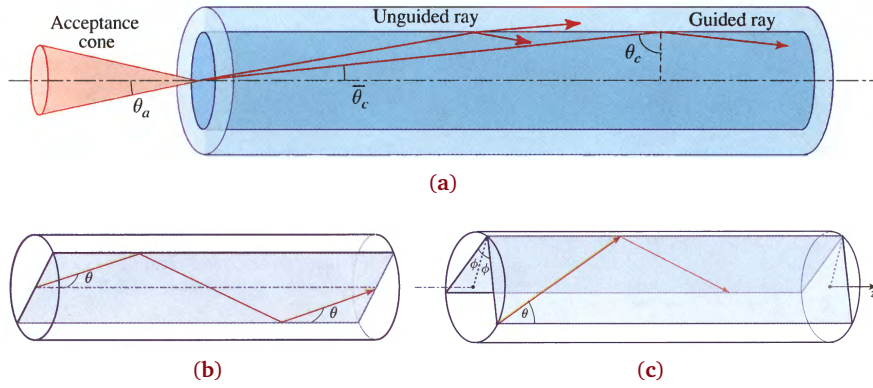


Fig. 2.4: (a) OF with guided and unguided rays as defined by acceptance angle, $\theta_a = \sin^{-1} \text{NA}$, and θ_c ; (b) OF guiding meridional rays; (c) OF guiding skewed rays. The illustration is from [20].

$U(r, \phi, z) = u_{l,m}(r) \exp(-il\phi) \exp(-i\beta_{l,m}z)$ can be solved by the Helmholtz equation in a cylindrical system as shown in Fig. 2.5 to find the radial distribution of the field in the core and cladding for integers $l = 0, \pm 1, \pm 2, \dots$ and $m = 1, 2, 3, \dots$, where $\beta_{l,m}$ is the propagation constant in the z direction. The results from the

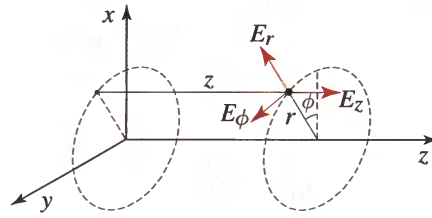


Fig. 2.5: Cylindrical coordinate system for the TEM plane wave. The illustration is from [20].

Helmholtz equation leads to an ordinary differential equation for the radial profile. The differential equations can further be written separately for core and cladding. The solution of these differential equations is found by using the Bessel functions

$$u_{l,m} \propto \begin{cases} J_l(k_T r), & r < a \quad \text{core} \\ K_l(\gamma r), & r > a \quad \text{cladding} \end{cases} \quad (2.4)$$

where $k_T = \sqrt{n_1^2 k_0^2 - \beta_{l,m}^2}$, $\gamma = \sqrt{\beta_{l,m}^2 - n_2^2 k_0^2}$, J_l is the Bessel function of the first kind, and K_l is the modified Bessel function of the second kind [20]. k_T and γ , respectively then determine the change in rate for $u_{l,m}(k_T, \gamma, r)$ in the core and cladding. Noting that, $k_T^2 + \gamma^2 = \text{NA}^2 k_0^2$, is a constant it can be shown that decreasing

k_T increases γ , i.e. the field is more confined to the core, whereas increasing k_T decreases γ , i.e. the field is less confined in the core. By normalizing k_T and γ to the radius of fiber core, a , it is possible to express the V parameter from $\sqrt{k_T^2 a^2 + \gamma^2 a^2}$ as

$$V = a \frac{2\pi}{\lambda_0} \text{NA} \quad (2.5)$$

V is here a design parameter for the OF. By analyzing the continuous derivative at, $r = a$, for the two expressions in (2.4), the values of the V parameters for low order modes can be found. The cut-off wavelength, λ_c , determines the maximum wavelength that can be guided in one or several linear polarized (LP) modes and can be found for the values of V shown in Tab. 2.1. With, $l = 1$, and, $m = 1$, it

Tab. 2.1: V parameter value for the cutoff wavelength for one or several modes $\text{LP}_{l,m}$

$\frac{l}{m}$	1	2	3
0	0	3.832	7.016
1	2.405	5.520	8.654

can be shown that a transverse electric single-mode (SM) plane wave is guided by the OF when $V < 2.405$. NA and a are then OF design parameters to obtain SM propagation at wavelength, λ_0 . For substantial V values, it is possible to relate it to the number of modes as $M \approx \frac{4}{\pi} V^2$.

Different sensor applications require different OF design parameters. Sensor applications using narrow pulse propagation are usually not preferred in multi-mode (MM) OF as each mode in the fiber is traveling with different group velocities, causing the pulse to spread. However, MM OF might have an advantage in fluorescence or absorbance measurements due to the high NA for illumination and collection of light intensities. Similarly, SM OF is usually preferred in applications such as distributed temperature or strain sensing due to the low dispersion of the pulse propagating in the fiber. In other applications where the evanescent field is used to detect or measure concentrations of chemicals, the use of SM OF with removed cladding is sometimes not practical considering that the core is in the range of $\sim 8 \mu\text{m}$. In the following Sections 2.1.2 and 2.1.3 we will have a brief look at different types of OF sensors and what they can offer.

2.1.2 Intrinsic Fiber Optic Sensor

Intrinsic FO sensors probes light-matter interactions in the cladding or core upon external stimuli from the surrounding medium. These light-matter interactions are often based on the light scattering or refraction in the OF. By measuring the change in light scattering or refraction, temperature or pressure can be monitored from changes in strain or compression of an OF [3], [21], [22]. Therefore, FO systems

detecting changes in temperature or strain are often based on FBG components or spontaneous elastic scattering in SM OF.

Fiber Bragg Gratings

FBG is fabricated by inscribing periodic RI modulations in an SM OF by illuminating it with fringes of ultra-violet (UV) light. The reflectance of an FBG can be analyzed by tracking the complex amplitudes of the forward and backward waves traveling through a multi-layered medium $M = M_N \dots M_2 M_1$, where M is known as the transmission matrix, as shown in Fig. 2.6(a)². $M_{1,1}$ of the 2x2 transmis-

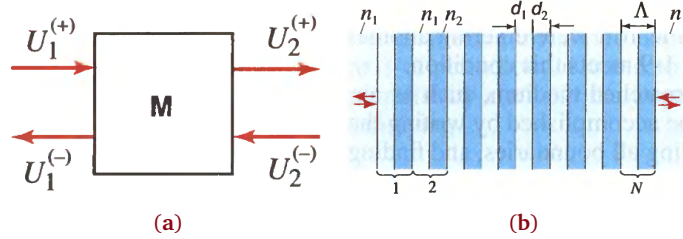


Fig. 2.6: (a) Forward and backward plane waves traveling in through a multi-layered medium represented as the wave-transfer matrix M ; (b) FBG with RI modulation separated by period Λ . The illustration is from [20].

sion matrix is expressed as $1/t^*$, where t^* is the complex (conjugate) amplitude transmittance [20]. The real component of $1/t$ is

$$\text{Re} \left\{ \frac{1}{t} \right\} = \frac{(n_1 + n_2)^2}{4n_1 n_2} \cos(\varphi_1 + \varphi_2) - \frac{(n_2 - n_1)^2}{4n_1 n_2} \cos(\varphi_1 - \varphi_2) \quad (2.6)$$

where $\varphi_1 = n_1 k_0 d_1$ and $\varphi_2 = n_2 k_0 d_2$ is the phase introduced in the grating period, Λ , as shown in Fig. 2.6(b). It follows from the Bragg total reflection regime that, $\text{Re} \left\{ \frac{1}{t} \right\} = \cos \Phi > 1$, where Φ is known as the Bloch phase [20]. To obtain total reflection with $\text{Re} \left\{ \frac{1}{t} \right\} > 1$, it can be shown that the maximum in (2.6) is obtained when the round-trip phase is, $2(\varphi_1 + \varphi_2) = 2k_0(n_1 d_1 + n_2 d_2) = 2\pi$. With $n_{\text{eff}} = (n_1 d_1 + n_2 d_2)/\Lambda$ as the effective RI, the Bragg wavelength is found as

$$\lambda_B = 2n_{\text{eff}} \Lambda \quad (2.7)$$

²Extensive information about using the transmission matrix to characterize photonic components can be found in Chapter 7.1, page 246, in [20]

Hence, a change in temperature or strain will change the period Λ of the FBG and the Bragg wavelength position. The temperature sensitivity of the Bragg wavelength position can be expressed as

$$\Delta\lambda_B = \lambda_B(\alpha_T + \mathfrak{J})\Delta T \quad (2.8)$$

where α_T is the thermal expansion coefficient and \mathfrak{J} is the thermo-optic coefficient [16]. Multiparametric sensing of temperature or strain is feasible by incorporating several FBGs with different Λ and corresponding λ_B [21]. Therefore, each FBG represent a point for temperature or strain sensing.

Distributed Sensing

Distributed temperature or strain sensing is possible by self-correlating the signal from the spontaneous elastic back-scattering in SM OF [3], [22]. This scattering process is known as Rayleigh scattering and is usually considered as a contribution to the attenuation of light in the fiber in telecommunication applications. It is also possible to utilize the inelastic back-scattering in SM OF known as Raman or Brilluoin scattering, which requires simpler processing methods as compared to using the Rayleigh scattering [23].

Rayleigh scattering from a narrow pulse propagating in the OF is useful for obtaining distributed temperature monitoring by measuring the temporal or frequency resolved changes in the scattering amplitude. The Rayleigh scattering coefficient of OF can be expressed as

$$\alpha_R = \frac{8\pi^3}{3\lambda^4} n^8 p^2 \epsilon_c k_B T_F \quad (2.9)$$

where n is the RI, p is the photo-elastic coefficient, k_B is Boltzmann constant, ϵ_c is the isothermal compressibility, and T_F is a fictive temperature of the density fluctuations frozen into the OF when it is cooled in the fabrication process [22]. $\Delta n(t, z)$ with dielectric parameter, $\Delta\epsilon(t, z)$, is fluctuating randomly in time, t , as a result of the random oscillation of electrons clouds from the molecules in the OF. The incident light is reorienting the oscillating electron clouds with a collective response. These collective reorientations of random oscillating electron clouds results in Rayleigh back-scattering with random amplitude intensities that changes with the temperature or strain state of the OF. Therefore, the change in these random collective oscillations and Rayleigh scattering amplitude intensities must be probed to find the change in temperature or strain. The transverse backward wave propagation of the Rayleigh scattering can be expressed as

$$E = \Psi(z, k) \exp(-ikz) \quad (2.10)$$

where $\Psi(z, k)$ is the Rayleigh scattering amplitude that is dependent on the local variations of the dielectric parameter $\Delta\varepsilon(z)$ within the range z [3]. Applying a Fourier transform on the random spatial variations of the permittivity relates the Rayleigh backward scattering signal to $\Psi(z, k) - \Psi(0, k)$. A reference length of the fiber is required to self-correlate the changes in the random fluctuating signal. The spatial resolution for these temperature or strain measurements is proportional to the pulse width propagating in the OF. Signal strength and spatial resolution are therefore often conflicting parameters in distributed OF sensors.

2.1.3 Extrinsic Fiber Optic Sensor

Extrinsic FO sensors probe light-matter interactions in the core-cladding interface or on the fiber end face. These light-matter interactions are often based on absorption or scattering of molecular entities that is used for determining their concentration [24]. Extrinsic FO sensors are also often based on interferometric or surface plasmon resonance (SPR) measurements [25], [26]. For the light-matter interactions occurring on the OF side face, the CF of the TEM wave must be chosen so that the evanescent field is interacting with sensing-medium. To achieve this the cladding can be removed, or gratings can be inscribed into the fiber to excite the TEM mode(s) into the cladding. Some impressive FO systems can be summarized below based on the side face or end face sensing.

Light-Matter Interactions on the Side Face

For cladding removal, MM OF is straight-forward to handle due to its larger core, but will not offer the control over the propagation constant at the fiber-solution interface due to a large number of modes. To use SM OF for side face sensing the TEM modes can be excited into the cladding by the use of LPFG or tilted fiber Bragg gratings (TFBG) [17], [27]. TFBG is similar to FBG as shown in Fig. 2.7(a), but has a grating period projected with an angle so that $\Lambda = \Lambda_g / \cos \theta$ where θ is the tilt angle and Λ_g is the actual period of the grating. As several modes are refracted by the tilted grating into the cladding, the phase of the traveling wave in the cladding and core is matched for each mode. The phase matching condition between mode, i and j , is $\beta_j = \beta_i \pm \beta_G$, with $\beta_G = 2\pi/\Lambda$ as the grating constant. The resonance wavelength λ_l for the phase matching between the core mode and another mode, l , becomes then

$$\lambda_l = \left[n_{\text{eff}}^{\text{core}}(\lambda_l) + n_{\text{eff}}^l(\lambda_l) \right] \Lambda \quad (2.11)$$

where $n_{\text{eff}}^{\text{core}}(\lambda_l)$ is the effective index of the SM guided by the core and $n_{\text{eff}}^l(\lambda_l)$ is the effective index for mode l [27]. The magnitude of the propagation constant β_l with the corresponding λ_l is also possible to control with the polarization of the incident TEM plane wave. These characteristics have resulted in some exciting approaches for FO based SPR biosensors improving its figure of merit (FOM) significantly [29],

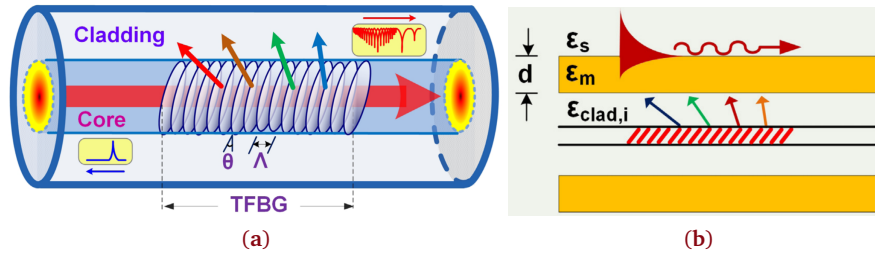


Fig. 2.7: (a) Illustration of a TFBG with tilt angle θ and grating period Λ ; (b) Surface plasmon polaritons (SPP) excited on the gold-coated TFBG by the TEM modes with corresponding propagation constant in the cladding. The illustrations are from [28].

[30]. With a gold layer deposited on the TFBG side face with a thickness in orders of nanometers as shown in Fig. 2.7(b), the propagation constants in the cladding, β_l , can be phase matched with the propagation constant of the surface plasmon polaritons (SPP), β_{SPP} , excited along the gold-solution interface. With $\beta_l = \beta_{\text{SPP}}^l$ it is possible to write

$$k_0 n_{\text{eff}}^l(\lambda_l) \sin \theta_l = k_0 \sqrt{\frac{\epsilon(\lambda_l) \epsilon_m}{\epsilon(\lambda_l) + \epsilon_m}} \quad (2.12)$$

where $\epsilon(\lambda)$ is the dielectric function of the metal and ϵ_m is the dielectric constant of the medium [27], [28], [31]. For TFBG, the SPR is usually excited in the infrared (IR) range, which may improve the sensitivity of SPR sensors providing longer propagation lengths of the SPP [29]. By obtaining the polarization dependent loss spectrum of the TFBG-SPR sensors, the FOM have shown to be higher than 10000, which is much higher than many SPR refractometers, which lie between 10 and 1000; an exciting development of miniaturized SPR sensors [27], [30].

Light-Matter Interactions on the End Face

Various OF sensor systems utilizing light-matter interactions on their end faces in reflection or transmission may also offer suitable solutions for many biosensor applications. For transmission measurements, the absorption of chemical compounds can be determined using one fiber for illumination and another fiber for light collection [32]. MM OF has a larger core and NA than SM OF and may be more convenient to use considering that the fibers have to be aligned. By using Beer-Lambert law, the concentration can be found for a fixed path length of the beam between the two fibers. Interferometric measurements from two OF end faces near each-other may also be used to determine the RI between them. Aligned end faces of two SM OF can be modeled as a dielectric slab with n_1 as the RI of the fiber cores as shown in Fig. 2.8, and with n_2 as the exterior medium. The transmission matrix is composed of three layers, $M = M_3 M_2 M_1$, with M_1 and M_3 as mediums with n_1

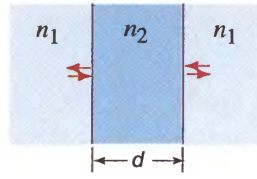


Fig. 2.8: Illustration of dielectric slab modeled as an interferometric RI sensor. The illustration is from [20].

and M_2 as a medium with n_2 . The total transmission is found from the 2x2 matrix M with $M_{2,2}$ as $1/t$. t can then be expressed as

$$t = \frac{4n_1n_2 \exp(-i\varphi)}{(n_1 + n_2)^2 - (n_1 - n_2)^2 \exp(-i2\varphi)} \quad (2.13)$$

where $\varphi = n_2k_0d$, and d is the width of the dielectric slab [20]. For a constant d , the RI of the exterior medium, n_2 , can be monitored as a function of the change in phase φ . FP interferometers used for optical length path measurements are described more in detail in Section 2.3.

Reflection based OF sensor systems may have simpler fabrications methods and a more convenient configuration for insertion into the environment that is monitored. OF RI sensors can be configured to have periodic patterns of noble metals on the facet or to be configured with a gold nanolayer on etched multicores in fiber bundles as shown in Fig. 2.9 and 2.10 [6], [33]. In Fig. 2.9, the incident TEM plane wave

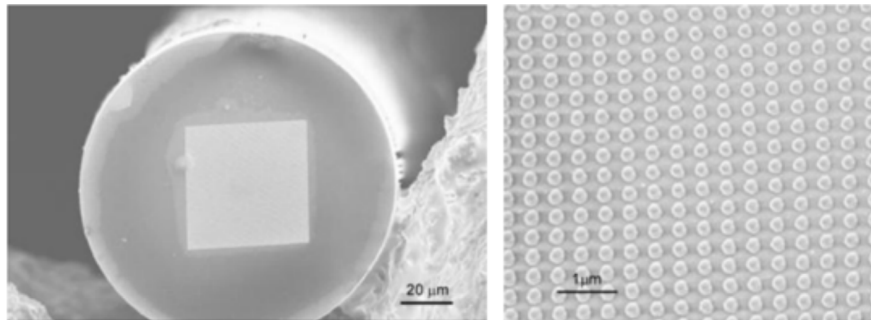


Fig. 2.9: Periodic noble metal structures on SM OF. The image is from [33].

on the periodic noble metal nanostructures (NMNS) on the facet excites localized surface plasmons that can be used for local RI sensing. The mechanisms behind localized surface plasmons are described more in detail in Section 2.4. For the OF bundles in Fig. 2.10, a gold nanolayer is deposited on the spiky end faces of the multicores. Each core represents an SPR sensor where the propagation constant,

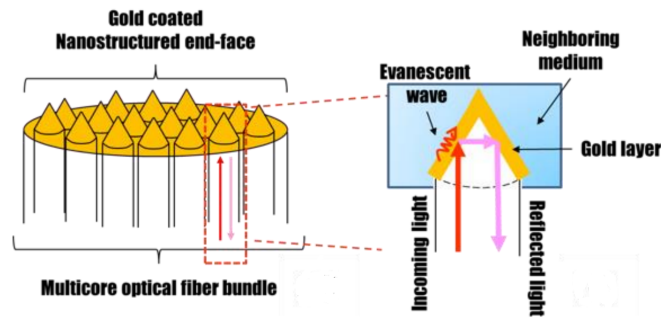


Fig. 2.10: SPR based multicore FO sensor. The illustration is from [6].

$\beta_{1,1}$, incident on the dielectric-gold interface is phase-matched with the propagation constant, β_{SPP} , of the SPP.

$$n_1 k_0 \sin \theta_{\text{cone}} = k_0 \sqrt{\frac{\varepsilon(\lambda) \varepsilon_m}{\varepsilon(\lambda) + \varepsilon_m}} \quad (2.14)$$

where θ_{cone} is the bounce angle of $\beta_{1,1}$ at the dielectric-gold interface [6], [31]. Multiparametric sensing is possible in this configuration since ε_m is measured locally on each of the spiky cores with gold surfaces.

2.2 Nanoparticles and Hydrogels for Label-Free Sensing

Label bound detection methods are often used in optical microscopy with molecules that are fluorescent or chemiluminescent. The molecular label binds to another molecule of interest and its amount can be observed by the intensity of the photons spontaneously emitted by the molecular labels. Label-free detection methods consist of omitting the molecular label only to measure the amount of the molecule of interest directly. By omitting the molecular label it is possible to monitor both the association and dissociation of molecular compounds directly in real time, e.g. as performed in the SPR technique [34], [35]. Label-free detection methods in photonic sensors are often based on the following features: (1) The measurement of light absorption or scattering of specific molecules; (2) The measurement of light interference in responsive dielectric mediums to determine the physical lengths between the RI modulations; and (3) The measurement of changes in the polarizability density³ for the dielectric function of materials and its surroundings. This thesis consists of using all three photonic label-free sensing features in developing novel label-free OF sensor systems. The following Sections 2.2.1 and 2.2.2 describes label-free recognition elements based on hydrogels and NMNPs.

³the material parameter in ME.

2.2.1 Noble Metal Nanoparticles

The NMNPs, made of gold or silver, are widely used in optical applications due to their wavelength dependent light scattering and absorption properties giving intense optical signals that can be observed in, e.g. dark-field optical microscope techniques. Copper has a high susceptibility to oxygen and is less used. The scattering or absorption of NMNPs for different wavelengths is dependent on particle size, particle shape and the RI of the medium surrounding them as shown in Fig. 2.11 [14]. Fig. 2.11(a)

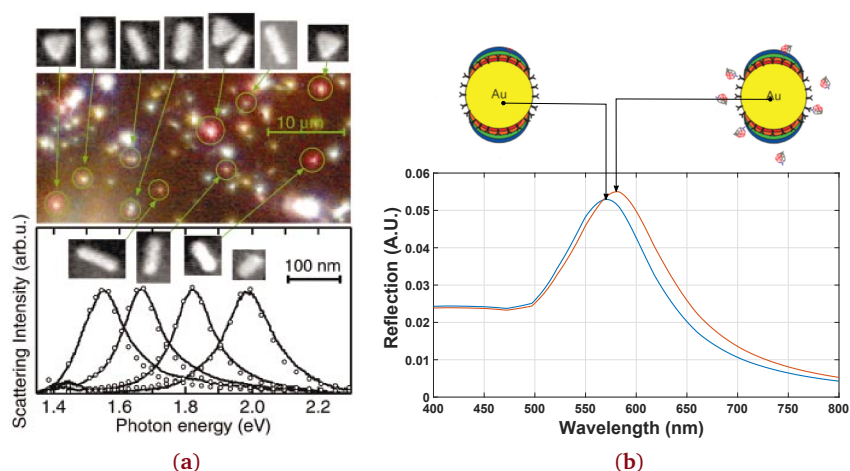


Fig. 2.11: (a) Optical dark field microscopy and scanning electron microscopy (SEM) images of scattered light from different gold nanoparticle (GNP). The images are from [36]; (b) Illustration of the spectral response to RI changes of the LSPR from GNPs. The illustration is from [37].

shows the optical dark-field and SEM images of scattered light from different GNPs, demonstrating the scattering wavelength (or color) dependence on their size and shape. Fig. 2.11(b) illustrates the scattering wavelength dependence on the local RI on the surface of the GNP. The maximum scattering with the corresponding wavelength is redshifted for the recombination of receptor-analyte on the GNP surface. The intense light scattering and absorption of GNP are due to its electron cloud oscillating collectively in resonance with the frequency of the incoming TEM wave. The localized collective oscillation of the electron cloud or LSPR can be considered to be a dipole for small particles with $r < 30$ nm, that have an electric field decaying with center-to-center distance d^{-3} [38]. Due to the intense electric field on the surfaces of NMNPs of different sizes, shapes, and cluster configurations they are also often used for surface enhanced raman scattering (SERS) [14], [31], [39]. The theoretical background for LSPR is described more in detail in Section 2.4.

The analyte-receptor recombination on NMNP surfaces can be described with the Langmuir model as



where $[AR]$ is the molar concentration of the analyte-receptor complex, $[A]$ is the molar concentration of the analyte, $[R]$ is the molar concentration of the receptors, and k_a and k_d are the association and dissociation rate constants, respectively [35], [40]. In the steady-state, we can equate the reaction rates for the association, $v_a = k_a[A][R]$, and dissociation, $v_d = k_d[AR]$, and write $[AR]$ as a function of $[A]$ as

$$[AR] = [R]_0 \frac{[A]}{K_d + [A]} \quad (2.16)$$

where $[R]_0$ is the initial concentration of unbound receptors, and $K_d = K_a^{-1} = \frac{[A][R]}{[AR]} = \frac{k_d}{k_a}$ is the dissociation constant [35], [40]. $[AR]$ increases non-linearly for $[A]$ with a decreasing rate and the analyte binding to receptor will in (2.16) saturate for $[A] \gg K_d$. High K_d would then indicate that the analyte-receptor complex formation is weak, whereas a high K_a would indicate an intense formation of the analyte-receptor complex.

2.2.2 Hydrogels

A hydrogel is a three-dimensional hydrophilic polymer network that contains a substantial volume fraction of water without being dissolved. Due to its ability to contain high amounts of water, hydrogels are widely used in applications such as drug delivery or tissue regeneration, but are however less exploited in biosensor applications [10], [11]. The hydrogel can be synthesized with recognition elements bound to the polymer chains so that the equilibrium for swelling is changed upon external stimuli, as shown in Fig. 2.12. The change in equilibrium swelling can

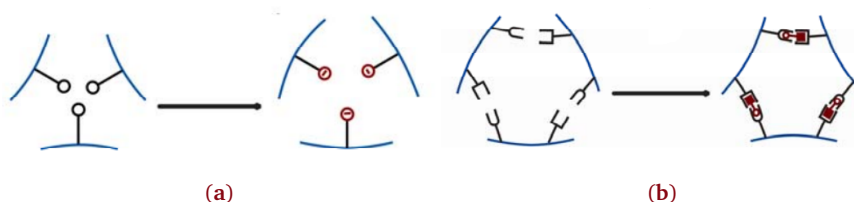


Fig. 2.12: (a) Change in swelling equilibrium for protonation or deprotonation of the recognition element; (b) Change in swelling equilibrium for receptor-analyte recombination. The illustrations are from [12].

be controlled as a function of solvent, pH, temperature, or ionic strength. By incorporating receptors in the hydrogel polymer network, such as an antibody, selective and label-free sensing of antigen can be performed as the recombination

antibody-antigen is contracting the hydrogel [12]. The dynamic swelling of ionic hydrogels can be described by the zero total osmotic pressure Π . The zero total osmotic pressure is composed of Π_{mix} , the free energy arising from mixing the polymer and solvent, Π_{elas} , the elastic force in the polymer chain deformation, and Π_{ion} , the difference in concentration of mobile ions on the inside and outside of the charged polymer chains. $\Pi = \Pi_{\text{mix}} + \Pi_{\text{elas}} + \Pi_{\text{ion}}$ is described as

$$\Pi = \frac{R_{\text{mg}}T}{V_1} (\ln(\phi_1) + \phi_2 + \chi\phi_2^2) + \frac{vR_mT}{V_0} \left(\frac{\phi_2}{2\phi_{2,0}} - \left(\frac{\phi_2}{\phi_{2,0}} \right)^{\frac{1}{3}} \right) + R_{\text{mg}}T\Delta C_{\text{tot}} \quad (2.17)$$

where ϕ_1 and ϕ_2 is the volume fraction of solvent and polymer phase, respectively, v is the molar number of elastic active polymer chains in reference to volume fraction $\phi_{2,0}$, R_{mg} is the molar gas constant, χ is the Fory-Huggins interaction parameter, V_1 is the molar volume of solvent, V_0 is the reference volume of the hydrogel, T is absolute temperature, and ΔC_{tot} is the difference in electrolyte concentration on the inside and outside of hydrogel [12], [41]. The term, Π_{elas} , may describe the swelling equilibrium as a function of cross-linking density due to receptor-analyte recombination. The formation of [AR] complexes that change Π_{elas} can be expressed as in (2.16). For slow diffusion times, the association time constant will be dependent on the spatial distribution of the receptors, i.e., the association time constant will be different for a two dimensional hydrogel than for a three-dimensional hydrogel. The diffusion time can be determined by the use of Fick's first law or the Nernst diffusion layer concept [35], [42]–[44]. In Fick's first law the flux of the analyte, J , is proportional to its diffusion constant, $J \propto D \propto 1/d_h$, where d_h is the hydrodynamic diameter of the analyte. Thus, smaller analytes have faster diffusion times than larger analytes. From the Nernst diffusion layer concept there is a so called diffusion layer creating a concentration gradient in the support-hydrogel-solution interfaces. The mass-transfer resistance of the analyte in the diffusion layer with length, δ , can be described as $r_{\text{anl}} = \delta/D_{\text{anl}}$, where D_{anl} is the diffusion constant of the analyte [35], [44]. With the hydrogel-solution phase as the first diffusion layer and the support-hydrogel phase as the second diffusion layer, there will be a concentration gradient in the support-hydrogel phase dependent on r_{anl} . In the steady state, the analyte flux in the first diffusion layer will be equal to the analyte flux in the second diffusion layer. Hence, the analyte diffusion constant will be smaller, and the concentration gradient will be more substantial in the support-hydrogel phase than in the hydrogel-solution phase.

Transducers used for estimating the change in equilibrium swelling are often based on optical microscope imaging, conductometric, dynamic light scattering, liquid column length or OF sensing [45]–[49]. The feasibility of using hydrogels as label-free sensors is usually limited by the accuracy of the methods used for detecting the change in hydrogel volume [12]. OF sensors may improve the accuracy

of detecting these volumetric changes by monitoring the light interferences in the hydrogel. Such OF sensor systems may be similar to the dielectric slab model expressed in (2.13) for varying width of the slab and constant n_2 . Both hydrogels and NMNPs are used for label-free sensing with OFs in this thesis. The proof-of-concept OF systems with NMNPs and hydrogels are further described in Section 2.3 to 2.6.

2.3 Fabry-Perot Interferometers

Interferometric methods utilizes the interference of light to detect the change in its optical path length as a function of the change in the material properties it is propagating in. The signal-to-noise ratio provided by this technique is really dependent on the instrumental configuration used, as shown from the various laser interferometer gravitational-wave observatory (LIGO) installations around the world, being able to detect ripples in space-time as a result of the gravitational waves made by the merging of black holes [50]–[52]. An OF based FP interferometer may detect the change in the optical path length intrinsically or extrinsically [25]. For intrinsic Fabry-Perot interferometer (IFPI), gratings or disruptions can be introduced in the core of a SM OF so the interference signal is monitored as a function of fiber strain or compression [25], [53]. LPFG, FBG or TFBG are some examples of FO systems that can be categorized as IFPI. FO system based on EFPI may use a mirror or a transparent film on the end face of an OF to create a FP etalon [25], [53]. EFPI based FO sensor may also be aligned with each-other to detect the optical path length or RI changes in a medium with a transmittance as expressed in (2.13). EFPI based OF sensors have been applied commercially for various purposes such as health monitoring of space aircraft, engineering structures, and composites structures. In Section 2.3.1 to 2.3.3, the reflection based FO EFPI sensors are described in detail with respect to characterizing and interpreting interferometric signals and concerning how SM OFs with hydrogels can be used for label-free biosensing.

2.3.1 Hydrogel – A Micro Fabry-Perot Cavity

EFPI based OF sensors in reflection can be analyzed by tracking the complex amplitudes of the forward and backward waves traveling through two partially reflective mirrors separated by distance d as shown in Fig. 2.13. The transmission matrix for this system is $M = M_3M_2M_1$, where M_3 is mirror 2, M_2 is the medium separating the mirrors, and M_1 is mirror 1. $M_{2,2}$ of the 2x2 transmission matrix, M , is $1/t$. By rewriting $1/t$, the intensity reflection for the FP cavity is found as

$$\mathfrak{R} = 1 - \frac{(1 - |r_1|^2)(1 - |r_2|^2)}{|1 - r_1r_2 \exp(-i2\varphi)|^2} \quad (2.18)$$

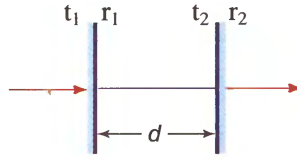


Fig. 2.13: A FP etalon with partially reflective mirrors. The illustration is from [20].

where $\varphi = nk_0d$ and n is the RI of medium M_2 . r_1 and r_2 are the amplitude reflectance's for mirror 1 and 2, respectively [20]. Assuming that $\arg\{r_1r_2\} = 0$ it is possible to write (2.18) as

$$\mathfrak{R} = 1 - \frac{\mathfrak{R}_{\min}}{1 + (2F/\pi)^2 \sin^2 \varphi} \quad (2.19)$$

where

$$\mathfrak{R}_{\min} = \frac{(1 - |r_1|^2)(1 - |r_2|^2)}{(1 - |r_1r_2|)^2} \quad (2.20)$$

$$F = \frac{\pi\sqrt{|r_1r_2|}}{1 - |r_1r_2|} \quad (2.21)$$

F is known as the finesse and is increasing as a function of the reflectance product r_1r_2 . In (2.18) and (2.19), it can be shown that the minimum \mathfrak{R} is obtained when $\varphi = nk_0d = q\pi$, where $q = 1, 2, 3, \dots$. The wavelength range, $\Delta\lambda$, between integers, Δq , also known as the free spectral range (FSR), can be further expressed as

$$\text{FSR} = \frac{\lambda_0^2}{2d_o} \quad (2.22)$$

where $d_o = nd$ is the optical length. The change in optical path length from φ can be used to determine the change in n or d of the medium, M_2 , by monitoring the change in wavelength position of the minima in \mathfrak{R} or the change in FSR.

As mentioned in Section 2.2.2, optical techniques may increase the accuracy in detecting small volumetric changes in stimuli-responsive hydrogels, making them available for use in label-free biosensing applications. The hydrogel may represent a micro FP cavity modeled as medium M_2 in Fig. 2.13 with intensity reflection as in (2.18). r_1 would here represent the support-hydrogel interface and r_2 would represent the hydrogel-solution interface. Due to scattering, absorption and mode-mismatch in the hydrogel, r_2 can be replaced with γr_2 , where γ is the loss factor. Since the hydrogel contains a significant volume fraction of water the reflectance product γr_1r_2 and finesse F can be assumed to be small. With $|\gamma r_1r_2| \ll 1$ and

$\arg\{\gamma r_1 r_2\} = 0$, the total reflection intensity $I(\lambda)$ for a hydrogel can be expressed by simplifying (2.18) into

$$I(\lambda) = I_0 \mathfrak{R}_{\text{hyd}} = I_0 \left[|r_1|^2 + |r_2|^2 + 2|\gamma r_1 r_2| \cos(2\varphi) \right] \quad (2.23)$$

where I_0 is the intensity of incident light. $I(\lambda)$ is a sinusoid with phase $2\varphi = 4\pi d_o / \lambda_0 + \varphi_0$, where φ_0 is the initially arbitrary phase⁴. Thus, the FSR of $I(\lambda)$ can be expressed as in (2.22) and its phase change as a function of the change in optical length can be expressed as

$$\Delta\phi_{\mathfrak{R}_{\text{hyd}}} = \frac{4\pi \Delta d_o}{\lambda_0} \quad (2.24)$$

The change in d_o is a result of both a change in physical length d of hydrogel cavity and a change in RI

$$\Delta d_o = \Delta n_{\text{gel}} + d \Delta n_{\text{gel}} \quad (2.25)$$

where n_{gel} is the RI of the hydrogel originating from solvent and polymer concentration. Due to the high volume fraction of water in the hydrogel, the main contributor to the optical length change will come from the change in d as a result of hydrogel swelling or contraction.

2.3.2 Interpretation of an Interferometric Signal

Quality of an Interferometric Signal

Quality of an optical resonator can be characterized by estimating the losses arising from imperfect reflection at r_1 or r_2 , as well as from absorption and scattering that occurs in the medium between r_1 and r_2 . It is possible to characterize the loss by estimating the quality factor Q defined as 2π multiplied by the ratio of stored energy to energy loss per cycle. With $F = \text{FSR} / \delta\lambda$ and with $\delta\lambda$ as the full width at half maximum (FWHM), Q can be expressed as [20]

$$Q = \frac{\lambda_0}{\text{FSR}} F = \frac{\lambda_0}{\delta\lambda} \quad (2.26)$$

For the unknown reflections values, r_1 and r_2 in F , it is possible to estimate Q by determining the experimental values, $\delta\lambda$ and λ_0 .

To estimate the quality of a low finesse FP cavity expressed in (2.23), it is possible to obtain Q as explained above, or it is possible to estimate the visibility parameter indicating the strength of interference between the waves. The visibility of (2.23) can be described as

$$\mathcal{V} = \frac{\max(I(\lambda)) - \min(I(\lambda))}{\min(I(\lambda)) + \min(I(\lambda))} \quad (2.27)$$

⁴phase-shift at r_1 and r_2 changes the reflection product from $-|\gamma r_1 r_2|$ to $+|\gamma r_1 r_2|$ in (2.23)

where $\max(I(\lambda))$ and $\min(I(\lambda))$ is the maximum and minimum intensity of $I(\lambda)$, respectively [20]. By inserting (2.23) in (2.27) the visibility becomes

$$\mathcal{V} = \frac{2|\gamma r_1 r_2|}{|r_1|^2 + |\gamma r_2|^2} \quad (2.28)$$

Since $Q \propto F \propto r_1 r_2$ for $r_1 r_2 \ll 1$, visibility can also be used as a measure of the quality factor.

Determining FSR and Phase Change in an Interferometric Signal

As noise and other artifacts often disrupts the interferometric signals, the use of interrogation techniques can significantly increase the accuracy of the monitoring. Considering that the signal is sinusoidal with changing period and phase, the use of interrogation methods such as cross-correlation techniques, fast Fourier transformation or quadrature demodulation techniques could be very advantageous. In this thesis, the focus will be on applying autocorrelation functions and quadrature modulation techniques to determine the period and phase, respectively.

The autocorrelation function is a symmetric and a self-correlating method. To illustrate the use it is possible to apply the function to the result in (2.23). With a wavelength-vector with $n_w = 1, 2, 3, \dots$ as the wavelength-vector integers with corresponding reflection intensities and vector length N_w , the autocorrelation function is measuring the correlation between $I(\lambda)_i$ and $I(\lambda)_{i+k_l}$ where $k_l = 0, 1, 2, \dots, (N_w - 1)$ is the lag time. The autocorrelation for lag time, k_l , is expressed as

$$r_{k_l} = \frac{\sigma_{sv}^2}{N_w - 1} \sum_{n_w=1}^{N_w-k_l} \left(I(\lambda)_i - \overline{I(\lambda)} \right) \left(I(\lambda)_{i+k} - \overline{I(\lambda)} \right) \quad (2.29)$$

where σ_{sv}^2 is the sample variance of the lag time series and $\overline{I(\lambda)}$ is the mean of $I(\lambda)$ [54]. The function will decay with lag time since the self correlating strength is decreasing with k_l . For a sinusoidal signal, the first peak in r_{k_l} , for $k_l > 0$, represents the maximum self-correlation strength for a lag time value that is equal to the period of the sinusoid. The FSR of $I(\lambda)$ is then found from the first peak with corresponding lag time since it is scalable to the wavelength.

By using the quadrature demodulation technique, it is possible to find the phase of an interferometric signal by knowing its period or FSR. A signal, such as $I(\lambda)$, can be modulated with a sinus or a cosinus resulting in the two functions

$$I_{\cos}(n_w) = I(\lambda) \cos(f_{\text{FSR}} n_w) \quad (2.30)$$

$$I_{\sin}(n_w) = I(\lambda) \sin(f_{\text{FSR}} n_w) \quad (2.31)$$

where $f_{\text{FSR}} = 1/k_{\text{FSR}}$ and k_{FSR} is FSR scaled as the lag time value found from the autocorrelation function [55], [56]. For $\Delta f = f_{\text{FSR}} - f_{\text{I}(\lambda)} \ll f_{\text{I}(\lambda)}$, with $f_{\text{I}(\lambda)}$ as the absolute frequency of the signal, the phase ϕ_{hyd} in $I(\lambda)$ can be expressed as [55], [56]

$$\phi_{\text{hyd}} = \tan^{-1} \left[\frac{\overline{I_{\text{sin}}}}{\overline{I_{\text{cos}}}} \right] \quad (2.32)$$

where

$$\overline{I_{\text{cos}}} = \frac{1}{N_w} \sum_{n_w=1}^{N_w} I_{\text{cos}}(n_w) \quad (2.33)$$

$$\overline{I_{\text{sin}}} = \frac{1}{N_w} \sum_{n_w=1}^{N_w} I_{\text{sin}}(n_w) \quad (2.34)$$

The error of the phase estimations is dependent on the error present in the estimated demodulation frequency f_{FSR} , but can be decreased with increasing numbers of periods in the signal.

In summary, the optical length can be determined from (2.22) by using the autocorrelation method, whereas the change in optical length from (2.24) can be determined by using of the quadrature demodulation technique. For significant hydrogel swelling and deswelling, it might be practical only to use the autocorrelation method to estimate the optical length if the sampling frequency of the interferometric signal results in phase changes larger than $\pi/2$. On the other hand, for small hydrogel swelling and contractions, it might be practical to use the quadrature demodulation technique combined with the autocorrelation method to detect the small changes in the optical length.

2.3.3 Sensor Implementation with Single-Mode Optical Fiber

FO sensors based on EFPI in reflection mode can be fabricated by immobilizing a hydrogel on the OF end face as shown in Fig. 2.14 [5], [13], [56]–[59]. IR light is confined as a single transverse mode in OF core and hydrogel volume which ensures sufficient interference between the field reflected at the fiber-gel interface, r_1 , and the field reflected at the gel-solution interface, r_2 . Since the reflection-product is, $r_1 r_2 \ll 1$, the hydrogel can be considered to be a low-finesse FP cavity. Hence, the reflection intensity of this FP can be described as (2.23) and the swelling equilibrium can be monitored by using the autocorrelation or quadrature demodulation methods in (2.29) and (2.32). Due to the significant volume fraction of water in the hydrogel, the contribution to changes in the optical length will arise from changes in the physical length with minor influence from the RI.

The hydrogel swelling can be tailored to be responsive to a variety of different biochemicals [5], [13], [56]–[59]. Firm adhesion of hydrogel on the OF end face ensures that there is no gap in-between creating additional reflections, which is

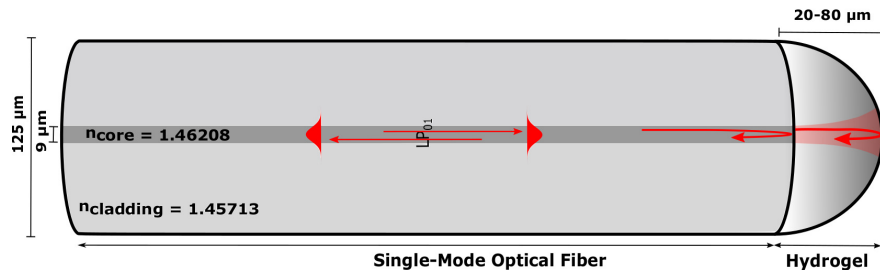


Fig. 2.14: Illustration of SM OF with hydrogel immobilized in its end face. IR light is confined as a single transverse mode in core and hydrogel with reflection at OF-gel interface and hydrogel-solution interface.

obtained by functionalizing the OF with silane groups that forms covalent bonds with the hydrogel [60]. Low surface roughness on the hydrogel-solution interface results in high visibility of the EFPI, and is obtained by polymerizing the pre-gel on the OF end face in an oil-water emulsion as shown in Fig. 2.15. Here, acrylamide

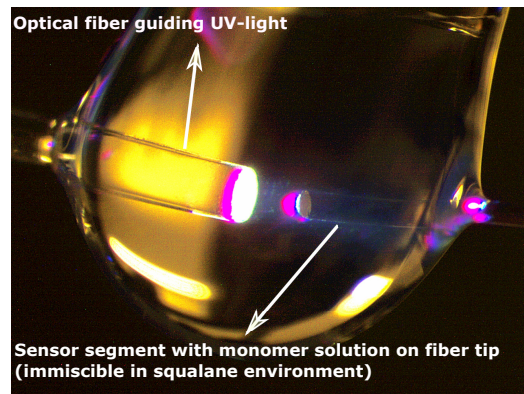


Fig. 2.15: Optical microscope image of the UV-polymerization of the pre-gel in an oil-water emulsion.

monomers are used as the backbone of the polymer network that can be incorporated with recognition elements [5]. The pre-gel with photoinitiator can be deposited on the OF end face with a pipette and further photopolymerized by using UV light. Under UV illumination the photoinitiator releases free radicals that are catalyzing the polymerization of the monomers, spacers and recognition elements in the pre-gel [11], [61].

The number of modes carried by the OF as defined by the V design parameter in (2.5) is also present in the FP cavity. The modes in the FP cavity can be expressed by using Hermite-Gaussian beams with indexes (l_{hg}, m_{hg}) [20]. For

Hermite-Gaussian beams the higher modes will propagate with an excess phase $\mathcal{Z}(z) = (l_{hg} + m_{hg}) \tan^{-1}(\frac{z}{z_0})$ where z_0 is the Rayleigh range. The mode(s) carried by the OF will also be present in the Hermite-Gaussian modes in the FP cavity. The visibility of the FP interference will, therefore, be higher for OF with few modes as opposed to OF with many modes. Hence, the use of SM OF have significant advantages being able to detect nanometer changes in the hydrogel swelling as compared to MM OF that is often limited by modal dispersion [5], [62].

2.4 Nanoplasmonic Systems

Nanoplasmonic systems are based on optical phenomena occurring at the nanometer scale from light interacting with the confined collective oscillations of electron clouds or plasmons. By using waveguides or mirrors, the optical field can not be confined to a scale below half of its wavelength. However, by using the optical field to excite plasmons in NMNS, the light is interacting with the oscillating electron clouds confined to a scale smaller than the diffraction limit. Noble metals show to be a suitable candidate to excite plasmons due to their high conductivity, that is often displayed as a free electron behavior. Incident visible (VIS) light on bulk gold excites bulk plasmons but cannot be used for RI sensing since they are localized inside the material. By reducing the gold size below $\lambda/2$, the plasmons can be excited on the gold surface if the propagation constant, $\beta = (2\pi n/\lambda_0) \sin \theta$, of the TEM plane wave is phase-matched with the propagation constant of the SPP as mentioned in Section 2.1.3. The excitation of SPP is thus dependent on the angle θ and the wavelength of the incident light. By reducing the gold size below $\lambda/2$ in three-dimensions, the plasmons can be confined to a nanosphere or particle that is collectively oscillating in resonance with the light frequency. The surface plasmons traveling in this nanoparticle is known as LSPR and are dependent on the particle size and shape as well as the local dielectric medium. This LSPR nano-probe can be used for sensing local RI changes. The excitation of LSPR is also independent of phase matching of propagation constants, i.e. it is independent of the angle of the incident light. NMNS have been implemented with OF in the last decade in various configurations and biosensor applications due to their label-free sensing, fast response times, high sensitivity, high selectivity, remote sensing capabilities, and simplified optical design [7]–[9], [18], [33], [63]–[77]. Multiparametric sensing is possible as the LSPR can be spectrally resolved for different sizes and shapes [9], [14]. Also, single or clustered NMNS of specific geometrical shapes exhibit intense localized electric fields on their surfaces which is useful for other label-free detection methods such as SERS [14], [31], [38], [39]. In the following Sections 2.4.1 to 2.4.5, extinction of NMNP, dipole-dipole coupling, LSPR dependence on metal-dielectric function, as well as the implementation of NMNP with OF for local RI sensing are described more in detail.

2.4.1 Gold Nanoparticle – A Nano-Probe Sensing the Refractive Index

Spherical Noble Metal Nanoparticles

As mentioned in Section 2.2.1, the intense light scattering and absorption of NMNP is due to the collective oscillating electron cloud in the particle that is in resonance with the frequency of the incoming TEM plane wave. The scattering and absorption are illustrated in Fig. 2.16. The scattering or absorption of NMNP can

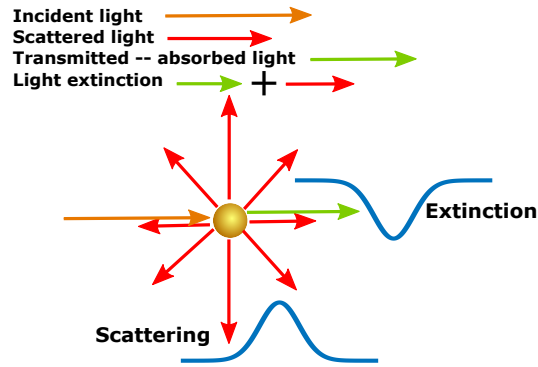


Fig. 2.16: Illustration of scattering, absorption and extinction of an NMNP.

be quantified by measuring the difference between incident light intensity I_0 and transmitted intensity I_t by using the Lambert-Beer law

$$I_t = I_0 \exp(-\sigma_{\text{ext}}NDd) \quad (2.35)$$

where $\sigma_{\text{ext}} = \sigma_{\text{sca}} + \sigma_{\text{abs}}$ is the extinction cross coefficient, σ_{sca} is the scattering cross coefficient, σ_{abs} is the absorption cross coefficient, ND is the number density and d is the length of the light path traveling through the medium with MNPs [78]. The scattering and absorption of MNPs will also be dependent on their size, shape, composition and surrounding environment. The light extinction by particles can be described from the Mie theory that is based on solving ME for a homogeneous sphere [79]. The solutions consist of both low and high order multipoles of electromagnetic waves traveling on the sphere. The scattering, extinction and absorption cross-section of gold nanospheres can be described as

$$\sigma_{\text{sca}} = \frac{P_{\text{sca}}}{I_0} = \frac{2\pi}{|k|^2} \sum_{L=1}^{\infty} (2L+1)(|a_L|^2 + |b_L|^2) \quad (2.36)$$

$$\sigma_{\text{ext}} = \frac{P_{\text{ext}}}{I_0} = \frac{2\pi}{|k|^2} \sum_{L=1}^{\infty} (2L+1)[\text{Re}(a_L + b_L)] \quad (2.37)$$

$$\sigma_{\text{abs}} = \frac{P_{\text{abs}}}{I_0} = \sigma_{\text{ext}} - \sigma_{\text{sca}} \quad (2.38)$$

where P is scattering, absorption or extinction power, I_0 is the incident plane wave intensity, L are integers representing a dipole for $L = 1$ or multipoles for $L > 1$ and k is the incoming wave vector [79]. a_L and b_L are parameters composed of the Riccati–Bessel functions ψ_L and χ_L

$$a_L = \frac{m\psi_L(mx)\psi'_L(x) - \psi'_L(mx)\psi_L(x)}{m\psi_L(mx)\chi'_L(x) - \psi'_L(mx)\chi_L(x)} \quad (2.39)$$

$$b_L = \frac{\psi_L(mx)\psi'_L(x) - m\psi'_L(mx)\psi_L(x)}{\psi_L(mx)\chi'_L(x) - m\psi'_L(mx)\chi_L(x)} \quad (2.40)$$

where the primes represent the first differentiation with respect to the argument in the parenthesis, $x = k_m r$, r is the radius of the particle, k_m is the wavenumber of the incident light within a medium, $m = \frac{n}{n_m}$, n_m is the real refractive index of the surroundings of the metal and $n = n_R + in_I$ is the complex refractive index of the metal [79]. For a dipole with $x \ll 1$, one can use an approximation of the Riccati–Bessel functions given by Bohren and Huffman to express the extinction and scattering cross-section as

$$\sigma_{\text{ext}} = \frac{18\pi\epsilon_m^{\frac{3}{2}}}{\lambda} \frac{4\pi r^3}{3} \left[\frac{\epsilon_2}{(\epsilon_1 + 2\epsilon_m)^2 + (\epsilon_2)^2} \right] \quad (2.41)$$

$$\sigma_{\text{sca}} = \frac{32\pi^4\epsilon_m^2}{\lambda^4} \left(\frac{4\pi r^3}{3} \right)^2 \left[\frac{(\epsilon_1 - \epsilon_m)^2 + (\epsilon_2)^2}{(\epsilon_1 + 2\epsilon_m)^2 + (\epsilon_2)^2} \right] \quad (2.42)$$

where ϵ_1 and ϵ_2 are the real and imaginary components, respectively, of the complex metal dielectric function $\epsilon(\lambda) = \epsilon_1 + i\epsilon_2$, ϵ_m is the dielectric constant of the surrounding medium, r is the radius of the particle, and λ is the wavelength of the incident light [80]. Extinction and scattering scales with r^3 and r^6 , respectively. Extinction is thus dominating for small particles, whereas scattering is dominating for larger particles. From the denominator in Equation (2.42) it can be shown that extinction and scattering is maximized at the plasmon resonance condition

$$\text{Re}[\epsilon(\lambda)] = -2\epsilon_m \quad (2.43)$$

$\text{Re}[\epsilon(\lambda)] = \epsilon_1(\lambda)$ is dependent on wavelength and needs to be negative to satisfy the condition in (2.43). Noble metals like gold have negative dielectric values for visible wavelengths due to the collective oscillation of conductive electrons in resonance with the light frequency. From (2.43) it can be noted that the LSPR wavelength is dependent on the dielectric properties of the surrounding medium ϵ_m . Therefore, a GNP can be used as a nano-probe for sensing the local RI on their surface.

The Dielectric Function of Metals

The real and imaginary dielectric values as a function of wavelength for gold or silver can be found from experimental measurements, such as from Johnson and Christy [81]. Thus, it is possible to find LSPR resonance wavelength, λ_{\max} , for σ_{sca} and σ_{ext} , by matching $\varepsilon_1(\lambda_{\max})$ with $-2\varepsilon_m$. The theoretical expression for ε_1 in (2.43) can be represented as free electron behavior for metals. From ME it is possible to derive an expression of the effective permittivity for conducting materials as a function of angular frequency, ω , and conductivity, σ [20]. Combining this expression with the Drude model and further describing conductivity as a function of frequency and electron collision frequency, γ , the real dielectric function of metals can be found as [31]

$$\varepsilon_1 = 1 - \frac{\omega_p^2}{\omega^2 + \gamma^2} \quad (2.44)$$

$$\omega_p = \sqrt{\frac{N e_c^2}{\varepsilon_0 m_e}} \quad (2.45)$$

Here ω_p is the angular frequency of the bulk plasma oscillations of the metal, N is the electron density of the metal, e_c is the electron charge, ε_0 is the permittivity of vacuum, and m_e is the effective mass of the electron. The collision frequency can be related to the electron mean free path, l_e , as $\gamma = v_F/l_e$, where v_F is the Fermi velocity [31]. For $\gamma \ll \omega$, the expression in (2.44) can be simplified to

$$\varepsilon_1 = 1 - \frac{\omega_p^2}{\omega^2} \quad (2.46)$$

When ω is lower than ω_p , ε_1 becomes negative, i.e., metals with high conductivities will satisfy the plasmon resonance condition for a spherical particle in (2.43). Real metals will have a considerable deviation from the free electron behavior at high frequencies due to inter-band and intra-band transition. These effects can be included by introducing ε_∞ in (2.46) as [31]

$$\varepsilon_1 = \varepsilon_\infty - \frac{\omega_p^2}{\omega^2} \quad (2.47)$$

By using (2.46) with the plasmon resonance condition $\varepsilon_1 = -2\varepsilon_m$ for a sphere the LSPR wavelength resonance becomes

$$\lambda_{\max} = \lambda_p \sqrt{2n_m^2 + 1} \quad (2.48)$$

while using (2.47) gives

$$\lambda_{\max} = \lambda_p \sqrt{2n_m^2 + \varepsilon_\infty} \quad (2.49)$$

where $\lambda_p = 2\pi c/\omega_p$ is the plasma oscillation wavelength of the bulk metal, and $n_m = \sqrt{\varepsilon_m}$, is the RI or the surrounding medium of the gold nanosphere [82].

Spheroidal Noble Metal Nanoparticles

The scattering and extinction of spheroidal particles can be described by Gans theory, a generalization of the Mie theory [83]. In the quasi-static approximation, the scattering and extinction cross-section of spheroids are

$$\sigma_{\text{ext}} = 4\pi \left(\frac{2\pi}{\lambda}\right) \text{Im}(\alpha) \quad (2.50)$$

$$\sigma_{\text{sca}} = \frac{8\pi}{3} \left(\frac{2\pi}{\lambda}\right)^4 \text{Re}|\alpha|^2 \quad (2.51)$$

where α is the polarizability of the spheroid [31], [84]. The polarizability in the quasi-static approximation can be further expressed as

$$\alpha = \frac{(1 + \kappa)V}{4\pi} \left(\frac{\varepsilon(\lambda) - \varepsilon_m}{\varepsilon(\lambda) + \kappa\varepsilon_m} \right) \quad (2.52)$$

$$\kappa = \begin{cases} \frac{1-L_p}{L_p}, & \text{Longitudinal mode} \\ \frac{1+L_p}{1-L_p}, & \text{Transverse mode} \end{cases} \quad (2.53)$$

$$L_p = \frac{1 - e^2}{e^2} \left[\frac{1}{2e} \ln \left(\frac{1+e}{1-e} \right) - 1 \right] \quad (2.54)$$

$$e = \sqrt{1 - \left(\frac{1}{\text{AR}} \right)^2} \quad (2.55)$$

where AR is the aspect ratio in κ for longitudinal or transverse excitation and $V = (4\pi abc)/3$ is the volume of a spheroid with semi-axes a , b and c [14], [83]. The AR of oblate and prolate spheroids is the ratio between the major and the minor axis⁵. The polarizability in (2.52) is maximized when the real part of the metal dielectric function, $\varepsilon_1(\lambda)$, and the dielectric constant of the surrounding medium, ε_m , satisfy the relation

$$\varepsilon_1(\lambda) = -\kappa\varepsilon_m \quad (2.56)$$

By using (2.46), the LSPR peak position as a function of local RI can be described as

$$\lambda_{\text{max}} = \lambda_p \sqrt{\kappa n_m^2 + 1} \quad (2.57)$$

From (2.57) it can be shown that the local RI sensitivity, $S = \Delta\lambda_{\text{max}}/\Delta n_m$, of noble metal spheroidal particles is dependent on κ and the AR of the spheroidal particle.

⁵For oblate spheroids $c = b < a$. For prolate spheroids $a = b < c$.

2.4.2 Dipole-Dipole Coupling

Near-field of Two Dipoles

The electric field with a distance, d , away from the NMNP is composed of the incident field, E_0 , and the near-field, E_{nf} , of the NMNP

$$E = E_0 + E_{\text{nf}} \quad (2.58)$$

The near-field for all possible multi-polar modes can further be expanded as

$$E_{\text{nf}} = \frac{2\alpha}{d^3} + \frac{3\beta}{d^4} + \frac{4\gamma}{d^5} + \dots \quad (2.59)$$

where $\alpha, \beta, \gamma, \dots$ is the dipole, quadrupole, octupole... polarizability tensors of the particle, respectively [38], [84], [85]. Hence, for minimal distance, d , relative to particle size more terms from the near-field expansion are included in E . For a two particle system the electric field felt by either of the particles can be described as (2.58). The plasmon oscillations for the two particles with center-to-center distance, d , are now coupled, and the field at particle one and two can be expressed as⁶

$$E_1 = E_0 + \xi \frac{p_2}{\epsilon_m d^3} \quad (2.60)$$

$$E_2 = E_0 + \xi \frac{p_1}{\epsilon_m d^3} \quad (2.61)$$

where $p_1 = \epsilon_m \alpha_1 E_1$ and $p_2 = \epsilon_m \alpha_2 E_2$ is the dipole moment of particle one and two, respectively [38], [84]–[86]. The factor $\xi = 3 \cos \theta_1 \cos \theta_2 - \cos \theta_{12}$ represents the coupling orientation of the dipoles where θ_1 is the angle between the direction of dipole one, θ_2 is the angle between the direction of dipole two, and θ_{12} is the angle between the direction of the two dipoles. For two dipoles in the side-by-side (s-s) or end-to-end (e-e) configuration, ξ becomes -1 and 2, respectively. By inserting expression for p_1 and p_2 into (2.60) and (2.61), the equation becomes

$$E_1 \left(1 - \xi^2 \frac{\alpha_1 \alpha_2}{d^6} \right) = E_0 \left(1 + \xi \frac{\alpha_2}{d^3} \right) \quad (2.62)$$

$$E_2 \left(1 - \xi^2 \frac{\alpha_1 \alpha_2}{d^6} \right) = E_0 \left(1 + \xi \frac{\alpha_1}{d^3} \right) \quad (2.63)$$

The average polarizability $\langle \alpha \rangle$ of the pair particles can be expressed in

$$\frac{1}{2}(p_1 + p_2) = \frac{1}{2}(\epsilon_m \alpha_1 E_1 + \epsilon_m \alpha_2 E_2) = \epsilon_m E_0 \langle \alpha \rangle \quad (2.64)$$

⁶for dipoles only

By using (2.62) and (2.63) with (2.64), $\langle\alpha\rangle$ can be described as

$$\langle\alpha\rangle = \frac{1}{2} \frac{\alpha_1 \left(1 + \xi \frac{\alpha_2}{d^3}\right) + \alpha_2 \left(1 + \xi \frac{\alpha_1}{d^3}\right)}{1 - \xi^2 \frac{\alpha_1 \alpha_2}{d^6}} \quad (2.65)$$

The average polarizability does not take into account the multi-pole effects expressed in (2.59). For small distances with near-contact between particle surfaces, the solution in (2.65) will display inaccurate values of $\langle\alpha\rangle$. However, multipole and retardation effects can be estimated by using the discrete dipole approximation (DDA), which has been shown to be a robust method for determining the dipole-dipole coupling of NMNPs of different size, shape and metal types [38], [87], [88].

Solutions for Particles with Identical Size and Shape

From (2.65), $\langle\alpha\rangle$ is maximized when

$$1 - \xi^2 \frac{\alpha_1 \alpha_2}{d^6} = 0 \quad (2.66)$$

By using (2.52) and assuming identical particles in the cluster with $\alpha_1 = \alpha_2$, the plasmon resonance condition becomes

$$\varepsilon_1 = -\mathcal{F}(d)\varepsilon_m \quad (2.67)$$

$$\mathcal{F}(d) = \frac{g^2 + \kappa \pm g(\kappa + 1)}{1 - g^2} \quad (2.68)$$

$$g = \frac{\xi(1 + \kappa)V}{4\pi d^3} \quad (2.69)$$

Substituting $g = \frac{\xi(1 + \kappa)V}{4\pi d^3}$ as, A/B , and κ as, C , expression in (2.68) can be further simplified to

$$\mathcal{F}(d) = \frac{4\pi\kappa \pm \xi \frac{V}{d^3} (1 + \kappa)}{4\pi \mp \xi \frac{V}{d^3} (1 + \kappa)} \quad (2.70)$$

where \pm and \mp indicates bright modes and dark modes, respectively.⁷ The bright modes occur due to the symmetric oscillation in the e-e and s-s configuration for the longitudinal plasmon mode. On the contrary, the dark modes occur due to the antisymmetric oscillation in the e-e and s-s configuration for the longitudinal plasmon mode. The excitation of dark modes is often very complicated but can be achieved by exciting them with the bright modes. The interference between bright modes and dark modes may give rise to phenomena such as Fano resonances [31], [84].

⁷+ and – in numerator and denominator for bright modes, respectively. For dark modes it is opposite.

Plasmon Ruler Equation

The LSPR wavelength resonance is dependent on the cubic power of the particle dimension to interparticle distance ratio. This dependence is possible to scale, so it display a universal behavior for particle sizes and shapes. This universal scaling behavior is often known as the plasmon ruler equation (PLE) and can be useful for accurate measurements of the distance between particles at the nanometer scale [89]–[91]. The PLE defined as $\Delta\lambda/\lambda_0$, can be derived first by using (2.46) and $\mathcal{F}(d)$ in (2.67).

$$\lambda_{\max} = \lambda_p \sqrt{\mathcal{F}(d)n_m^2 + 1} \quad (2.71)$$

This can further be developed by finding its first derivative with respect to \mathcal{F} .

$$\frac{\Delta\lambda_{\max}}{\Delta\mathcal{F}(d)} = \frac{\lambda_p n_m^2}{2\sqrt{\mathcal{F}(d)n_m^2 + 1}} \quad (2.72)$$

For entirely separated particles with $d \rightarrow \infty$ the function $\lambda_{\max}^0 = \lambda_p \sqrt{\kappa n_m^2 + 1}$. Hence, the PLE is

$$\frac{\Delta\lambda_{\max}}{\lambda_{\max}^0} = \frac{n_m^2 \Delta\mathcal{F}(d)}{2\sqrt{(\mathcal{F}(d)n_m^2 + 1)(\kappa n_m^2 + 1)}} \quad (2.73)$$

Note that the solution in (2.70) used for the PLE in (2.73) is based on the point dipole model and does not take into account the retardation effects or the effect of multi-poles expressed in (2.59). For small distances with near-contact between particle surfaces the solution in (2.73) may display inaccurate values. However, by using DDA methods the PLE is shown to be approximated as

$$\frac{\Delta\lambda}{\lambda_0} \approx 0.18 \exp\left(\frac{-(s/D)}{0.23}\right) \quad (2.74)$$

for different shapes, sizes, type of metals and dielectric constants of medium [92]. Here, $s = d - D$, is the separation distance between particles and D is the diameter of a particle along the axis of interparticle interaction. The decay rate, τ , in $a \exp(-x/\tau)$, of PLE for different NMNP (size, shape, metal type) are shown to be roughly 0.2 with only variations in the magnitude a [92]. This reflects that the strength of interparticle electromagnetic coupling relative to the intraparticle plasmonic restoring potential may have a universal decay rate for many types of NMNPs.

2.4.3 Change in the Metal Dielectric Function

The LSPR wavelength shift may originate from effects other than the change in size, shape, metal or dielectric medium. Charge transfer may occur between NMNPs and chemicals that are broadening or shifting the plasmon resonance. This effect is often known as chemical interface damping (CID), and may be explained by the

plasmon decay rate (or collision frequency), γ , that is a dampening constant for the oscillating electrons in the Drude model in (2.44) [31], [85], [93]–[96]. The total plasmon decay rate can be expressed as

$$\gamma = \gamma_b + \gamma_{\text{rad}} + \gamma_{\text{surf}} + \gamma_{\text{CID}} \quad (2.75)$$

where γ_b is the bulk damping, γ_{rad} is the radiation damping, γ_{surf} is the electron-surface scattering, and γ_{CID} is the CID [94]. The bulk damping describes the scattering of electrons with impurities, phonons, electrons or lattice defects. Radiation damping occurs due to the secondary light emission. Electron-surface scattering describes the scattering of electrons in NMNP with a size comparable to the mean free electron path, l_e . CID is included as the last term and describes the damping that occurs due to changing the chemical interface of the NMNP. The size dependence in (2.75) can be further expressed for each term as

$$\gamma = \gamma_b + 2\hbar K_{\text{rad}} V + \frac{A_{\text{surf}} v_F}{l_{\text{eff}}} \quad (2.76)$$

where \hbar is Planck's constant, V is the volume of a particle with a proportionality constant K_{rad} , l_{eff} is the average distance of electrons to surface, v_F is Fermi velocity, and A_{surf} is a proportionality constant [31], [85], [93]–[96]. The CID overcomes the other damping terms for small particle sizes when the average electron path length to the surface is within a range so that the energy of the plasmon resonance is transferred to the surface molecules.

Electrons may also be injected into or removed from MNMNs changing their electron density leading to a plasmon resonance wavelength shift. This may occur due to adding chemical reductants to the NMNP colloid solution or due to electrodes in solution transferring electrons to the particles [97]–[101]. The MNMNs can also be cathodically polarized by using radiolytically generated reducing agents [102]. For spheroidal NMNP, λ_{max} is found by using (2.47)

$$\lambda_{\text{max}} = \lambda_p \sqrt{\varepsilon_m \left(\frac{1 - L_p}{L_p} \right) + \varepsilon_\infty} \quad (2.77)$$

where L_p is the shape dependent depolarization factor in (2.54). By taking the first derivative of (2.77) with respect to N (the electron density), it can be expressed as⁸

$$\frac{\Delta \lambda_{\text{max}}}{\Delta N} = -\frac{\lambda_p}{2N} \sqrt{\varepsilon_m \left(\frac{1 - L_p}{L_p} \right) + \varepsilon_\infty} \quad (2.78)$$

⁸for simplicity it is assumed that ε_∞ is not changing with N

With λ_0 expressed as in (2.77) the ratio $\Delta\lambda_{\max}/\lambda_0$ becomes [97]

$$\frac{\Delta\lambda_{\max}}{\lambda_0} = -\frac{\Delta N}{2N} \quad (2.79)$$

The red or blueshift of LSPR for NMNPs is proportional to the decreasing or increasing electron density, respectively. It can also be noted that the expression in (2.79) is independent of particle size, shape and RI. However, the electrons injected or removed from single or clustered NMNPs are dependent on their oscillating strength as well as the thickness of the electrical double layer on their surfaces [97].

2.4.4 Interpretation of a Plasmon Resonance Signal

Q Factor, Limit of Detection, Sensitivity, Figure of Merit

As for EFPI based resonators, the quality of a plasmon resonance signal can be characterized by estimating the losses arising in each collective electron cloud oscillation. From the Drude model in (2.44) the quality factor at resonance can be expressed as $Q = \omega/2\gamma$ that is a function of the dampening constant, γ [39]. It is also possible to express the quality factor for nanoplasmonic systems as a universal analytical formula

$$Q = -\frac{\varepsilon_m}{\Delta\varepsilon_m} \frac{\Delta\omega}{\gamma} \quad (2.80)$$

where $\Delta\omega$ is the angular frequency shift of LSPR for the change in the dielectric constant $\Delta\varepsilon_m$ [103]–[105]. From (2.80) the minimum number of detectable analytes, N_a , or limit of detection (LOD) is

$$N_a = \frac{|\Delta\omega|}{\gamma} \frac{\varepsilon_m}{\alpha_a} \frac{V_m}{Q} \quad (2.81)$$

where α_a is the polarizability of the analyte, and V_m is the modal volume of the surface plasmons of a nanoparticle [103]–[105]. The sensitivity is also a useful parameter that can be used to describe the FOM. Sensitivity in LSPR based sensors is the ratio between wavelength shift and RI with units in (nm/RIU)

$$S = \frac{\Delta\lambda_{\max}}{\Delta n_m} \quad (2.82)$$

The sensitivity is a parameter in FOM as

$$\text{FOM} = \frac{S}{\delta\lambda} \quad (2.83)$$

where $\delta\lambda$ is the linewidth of the LSPR [14]. Sensitivity, FOM and LOD are instrumental parameters to describe the quality of an LSPR signal. The parameters may also define the applications the LSPR sensor systems are used for.

Estimating Plasmon Resonance Wavelength Shift

Due to noise and other artifacts disrupting the LSPR signal it may be useful to apply interrogation techniques for estimating the plasmon resonance wavelength shifts to increase the accuracy of the monitoring. For a Lorentzian LSPR signal, it is possible to implement a wavelength or frequency estimator based on a Fourier transform

$$\begin{aligned} \mathcal{F}\{\mathcal{L}((v - v_0) - \delta v, \Delta v)\} \mathcal{F}^*\{\mathcal{L}((v - v_0), \Delta v)\} \\ = \\ |\mathcal{F}\{\mathcal{L}((v - v_0), \Delta v)\}|^2 \exp(-i2\pi f \delta v) \end{aligned} \quad (2.84)$$

where \mathcal{F} represents the Fourier transform of the Lorentzian \mathcal{L} , f is the frequency of the Fourier domain, δv is the frequency shift away from v_0 , Δv is the Lorentzian linewidth, and $\mathcal{F}\{\mathcal{L}((v - v_0), \Delta v)\}$ is a known reference signal that is sufficiently averaged [106]. Based on estimating amplitude and phase in (2.84) it is possible to find the shift in frequency δv and the wavelength resonance shift.

For asymmetric Gaussian signals modulated by linear or non-linear functions, it may be useful to apply a smoothing spline function to find LSPR peak wavelength. The smoothing spline, s , can be computed for a smoothing parameter, p , that minimizes the expression

$$p \sum_{i=1}^{N_w} g_i [y_i - s(x_i)]^2 + (1 - p) \int \left(\frac{\partial s}{\partial x} \right)^2 dx \quad (2.85)$$

where N_w is the length of the wavelength-vector x received from the spectrometer, and y_i is the LSPR signal for wavelength-vector, x_i [107]. g_i is used for specified weighting of individual observations in y_i . By choosing a fixed smoothing parameter, the balance between residual error and local variation is also fixed.

2.4.5 Sensor Implementation with Multi-Mode Optical Fiber

FO LSPR sensors in reflection can be fabricated by immobilizing NMNPs in a hydrogel on OF end face as shown in Fig. 2.17 [108]. By using MM OF, an intense LSPR signal can be obtained as a result of the high NA exciting a significant fraction of the NMNPs and an effective collection of scattering from the LSPR of the NMNPs. The advantage of immobilizing NMNPs in hydrogel lies in the large number of particles for sensing, precise control over number density (ND), low cost manufacturing and having free standing single NMNP distributed in a three-dimensional aqueous environment. Applications would consist of detecting volumetric changes in the hydrogel, receptor-analyte recombination on the NMNP surface or by detecting chemical concentrations with SERS. The method for fabricating hydrogel on the

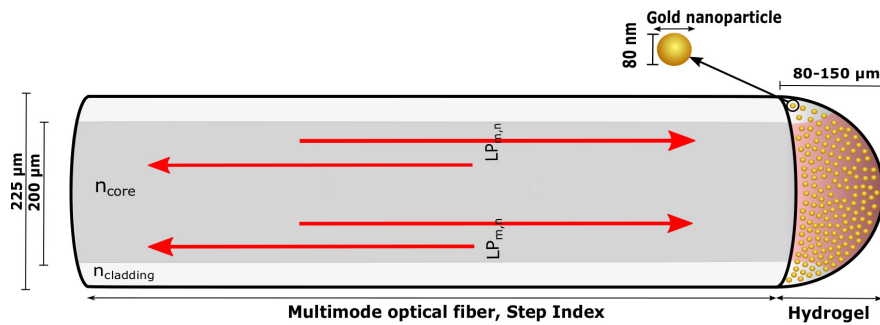


Fig. 2.17: Illustration of MM OF with hydrogel embedded with NMNP on OF end face. Light is guided in the fiber core with NA colored as red in fiber and hydrogel. The illustration is from [108].

OF end face is described in Section 2.3.3. The pH or ionic strength of the pre-gel may change the surface charge on the NMNPs and induce aggregation. To prevent nanoparticle aggregation, the pH or ionic strength of the pre-gel can be adjusted, or the surface charge of the NMNP can be controlled by using different stabilizing agents such as citric acid or polyethylene glycol (PEG) with carboxyl or amine groups [109].

With NMNPs immobilized in the hydrogel, both scattering and absorption will contribute to the reflected LSPR signal as shown in Fig. 2.18. Assuming that the

1. Incident light from lightsource
2. Reflection at fiber-gel interface from (1)
3. Transmission from (1) through hydrogel only
4. Incident light on GNP from (1)
5. Extinction of GNP from (4)
6. Reflection from (5) and/or (3) at hydrogel-solution interface and incident on GNP only
7. Scattering of GNP from (4) combined with extinction of GNP from (6)
8. Reflection from (5) and/or (3) at hydrogel-solution interface and transmission through hydrogel only
9. Scattering of GNP from (6) and (4)
10. Reflection from (8), and (7)

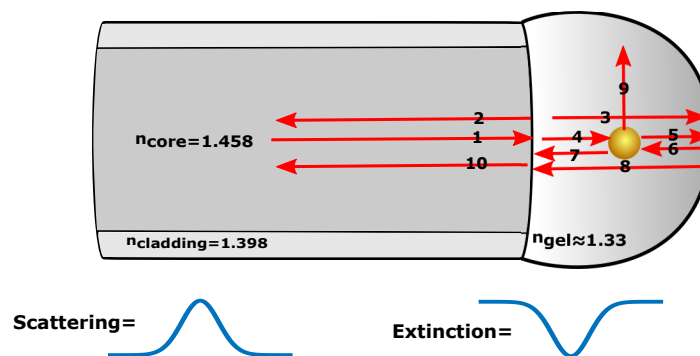


Fig. 2.18: Scattering and extinction of NMNP embedded in a hydrogel. The illustration is from [108].

scattering and absorption are weak, the change in reflected power due to NMNP can be approximated as

$$\Delta P_R = (1 - R_1)^2 \left[\frac{1}{2} \left(\frac{\text{NA}}{4} \right)^2 \sigma_{\text{sca}} - R_2 \sigma_{\text{ext}} \right] \text{ND} 2d P_{\text{in}} \quad (2.86)$$

where R_1 is the reflectance of the OF-hydrogel interface, R_2 is the reflectance of hydrogel-solution interface, ND is the GNP density, NA is numerical aperture, d is the physical length of the hydrogel and P_{in} is the input power [110]. A reflection dip for net absorption or reflection peak for net scattering will depend on the relative strength of the scattering and extinction terms. Depending on the shape of the signal it is possible to estimate the resonance peak wavelength by using the smoothing spline interpolant in (2.85), or the Fourier estimation in (2.84) can be used. The LSPR shift for the FO system in Fig. 2.17 will either be due to local RI changes or dipole-dipole coupling. Changes in the hydrogel volume can be measured by utilizing either or both of the effects depending on the polymer wt% of the hydrogel and ND of the MNMNs used, while receptor-analyte recombination on the NMNP surface can be detected from the local RI changes.

As mentioned in Section 2.3.3, the hydrogel also represents a micro FP cavity that can be used for interference measurements. For MM OF the interference might be washed out due to modal dispersion since each mode is traveling with different group velocities. The number of modes can be approximated to be proportional to V^2 in (2.5) for large V parameter values. For Hermite-Gaussian beams (as mention in Section 2.3.3) with indexes $(l_{\text{hg}}, m_{\text{hg}})$ the higher modes in the FP cavity will propagate with an excess phase of $\mathcal{Z}(z) = (l_{\text{hg}} + m_{\text{hg}}) \tan^{-1} \left(\frac{z}{z_0} \right)$ where z_0 is the Rayleigh range [20]. With V parameter of more than 100 for MM OF, there is several thousands of modes in the FP cavity, i.e., the visibility of the FP cavity will efficiently be reduced to zero.

2.5 Multiparametric Sensor Implementation

The advantage of using FO sensors for multi-sensing applications lies in controlling the TEM plane wave properties of phase, amplitude, polarization and frequency. By controlling the wave properties, the sensor parameters can be multiplexed spectrally, temporally, or for polarization. The monitoring of several parameters is both useful for obtaining information from several spatial points and for increasing the accuracy of the sensing by correlating the relevant parameters. Spectral multiplexing can be based on multiple sensing elements such as FBG or FP interferometers [16], [21], [25], [53]. Temporal multiplexing can be based on distributed sensing-based OFs by measuring the change in its intrinsic properties from the change in Rayleigh or Brillouin scattering [3]. Many applications also require simultaneous measure-

ment of several parameters in a single sample or single position. Multiple sensor elements can be used in single sample or position, but the increased size of the resulting sensor might not be acceptable. E.g., for medical applications there is a great need for sensing multiple parameters in one single point, combined with other essential features like small dimensions, label-free sensing, real-time monitoring and high sensitivity. By exploiting the intrinsic or extrinsic light-matter interactions on the core-cladding interface or on the OF end face, many of these requirements can be satisfied. Multiple-parameter sensing can be achieved in a single position by using multiple-modes as performed with TFBG [27], [28]. Spectral multiplexed sensing in single positions can be achieved by using fluorophores of different wavelengths [111], [112], or using NMNPs of different LSPR wavelengths in an optode or on the facet of a cleaved OF [9]. In this thesis, the LSPR and interferometric sensor modalities described in Section 2.3.3 and 2.4.5 for obtaining dual parameter sensing have been utilized. Some additional effects may arise in both signals, and the mechanisms behind them are described in Section 2.5.1 and 2.5.2. The FO sensor system combining LSPR and interferometric sensor modalities are described in Section 2.5.3.

2.5.1 Distribution of Particles in Hydrogel

Since the hydrogel changes its swelling equilibrium in response to chemical stimuli, it will also change the ND of the particles distributed in it. For hydrogel deswelling, the interparticle distance decreases which may increase the dipole-dipole interactions between the NMNPs. Therefore, the distribution of particles in the hydrogel will influence the amplitude and linewidth of the observed LSPR signal. The probability density function related to interparticle distances can be accurately estimated by utilizing models based on the nearest-neighbor distribution function (NNDF) [113]–[115]. With nearest-neighbor at a given distance, $l = d - r$, from a point in the region exterior to the particles, the void NNDF for randomly-distributed three-dimensional impenetrable spheres in the Carnahan–Starling approximation can be expressed as

$$H_v(y) = 24\eta(1-\eta) \left(ey^2 + fy + g \right) \exp \left[-\eta \left(8ey^3 + 12fy^2 + 24gy + h \right) \right] \quad (2.87)$$

where $y = \frac{l}{2r} > \frac{1}{2}$, $\eta = \frac{\text{ND}\pi(2r)^3}{6}$ is the reduced density, ND is the number density and $e = e(\eta)$, $f = f(\eta)$, $g = g(\eta)$, $h = h(\eta)$ are the density-dependent coefficients.

$$e(\eta) = \frac{1 + \eta}{(1 - \eta)^3} \quad (2.88)$$

$$f(\eta) = -\frac{\eta(3 + \eta)}{2(1 - \eta)^3} \quad (2.89)$$

$$g(\eta) = \frac{\eta^2}{2(1-\eta)^3} \quad (2.90)$$

$$h(\eta) = \frac{-9\eta^2 + 7\eta - 2}{2(1-\eta)^3} \quad (2.91)$$

With $\eta \ll 1$, Equation (2.87) can be simplified to⁹

$$H_v(y) = 24\eta y^2 \exp[-8\eta y^3], y > \frac{1}{2} \quad (2.92)$$

With significant dipole-dipole interactions between NMNP for $d \leq 5r$ [116], the probability of finding particles within this range can be computed by integrating $H_v(y)$ from $y_1 = \frac{2r-r}{2r} = \frac{1}{2}$ to $y_2 = \frac{5r-r}{2r} = 2$

$$P(d \leq 5r) = \int_{y_1}^{y_2} 24\eta y^2 \exp[-8\eta y^3] dy = -\exp[-8\eta y_2^3] + \exp[-8\eta y_1^3] \quad (2.93)$$

From Equation (2.92) it can be observed that increasing ND for hydrogel contraction increases the amplitude of $H_v(\frac{\bar{d}-r}{2r})$ at the mean interparticle distance, \bar{d} , while its width is decreasing. Hydrogel swelling or contraction will then influence the amplitude and the linewidth of the LSPR signal for $\bar{d} \leq 5r$. Since NNDF is based on the assumption that the particles are randomly distributed, it can also be compared with LSPR coupling experiments of NMNP to determine the particle distribution qualitatively.

2.5.2 Refractive Index For a Contracting Hydrogel

Changes in RI for a Dynamic Hydrogel Volume

Since hydrogels have a significant volume fraction of water, the swelling or contraction will result in small RI changes that have negligible influence on the interferometric measurements of the physical length of the FP cavity. By increasing the wt% of the monomers used for polymerization, the network will be denser. With high polymer density there will be larger RI changes for hydrogel swelling or contraction. Hence, NMNP may sense the change in RI as a result of the change in the hydrogel volume depending on the wt% of the monomers used in the polymerization. This could be a disadvantage in receptor-analyte recombination measurements but an advantage in detecting changes in the hydrogel volume¹⁰. The RI of the hydrogel can be represented by the relation

$$n_{\text{gel}} = n_p x_p + n_w(1 - x_p) \quad (2.94)$$

⁹assuming no close-packing of particles.

¹⁰change in polymer density is changing the local RI around the NMNP

where n_p is the RI of the polymer, n_w is the RI of the water and x_p is the mole fraction of the polymer. As the hydrogel is composed of two components, polymer and water, the relation between the mole fraction, x , and mass fraction, w , can be found from

$$w_w m_p = w_p m_w \quad (2.95)$$

$$x_p \frac{m_w}{M_w} = x_w \frac{m_p}{M_p} \quad (2.96)$$

where w_p is the mass fraction of the polymer, w_w is the mass fraction of water, m_p is the mass of the polymer, m_w is the mass of water, M_p is the molar mass of the polymer and M_w is the molar mass of water. m_p will be constant for hydrogel swelling and deswelling, while m_w will change. By using the relations in Equation (2.95) and (2.96), the ratio $\frac{m_w}{m_p}$ can be expressed with respect to the mole fraction of the polymer as

$$\frac{m_w}{m_p} = \left(\frac{1}{x_p} \right) \left(\frac{M_w}{M_p + M_w \frac{w_p}{w_w}} \right) = \frac{1}{x_p} a \quad (2.97)$$

x_p can be further described as a function of the hydrogel swelling degree by scaling it to the ratio $\frac{V_{\text{pregel}}}{V}$ where V_{pregel} is the volume of pre-gel (the polymerization of pre-gel is described in Section 2.3.3) on the OF and V is the volume of the hydrogel on the OF. The ratio $\frac{m_w}{m_p}$ as a function of $\frac{V_{\text{pregel}}}{V} = v$ by using Equation (2.95) gives

$$\frac{m_w}{m_p} = \left(\frac{1}{v} \right) \left(\frac{\frac{w_w}{w_p} \rho_p + \rho_w}{\rho_p + \frac{w_p}{w_w} \rho_w} \right) = \frac{1}{v} b \quad (2.98)$$

where ρ_p is the density of the polymer (pure), and ρ_w is the density of water (pure). By setting (2.97) equal to (2.98), x_p is scaled to v with a and b

$$x_p = v \frac{a}{b} \quad (2.99)$$

The ratio $\frac{a}{b}$ is only weakly dependent on the swelling degree. Therefore, it is possible to approximate $\frac{a}{b}$ as a constant found with the initial value of x_{p0} and v_0 . By inserting (2.99) into (2.94), the RI can be assessed for the hydrogel swelling and contraction from knowing the initial and dynamic volume change.

RI Changes from Inclusion of Dipoles in Hydrogel

The NMNPs immobilized in the hydrogel can be represented as dipoles each with a polarizability, α . In the quasi-static approximation, the dipoles perturbate the electric field inside the hydrogel. The total perturbation of the electric field is found by using the superposition principle and the macroscopic permittivity can be related to the volume fraction of dipoles included with respect to the volume of the hydrogel. The effective RI, ε_{eff} , as a function of the volume fraction, $f_v = V_{\text{dipoles}}/V_{\text{hydrogel}}$, can

be expressed by using the Maxwell Garnett mixing formula for $f_v \ll 1$ [85], [117]

$$\frac{\varepsilon_{\text{eff}} - \varepsilon_m}{\varepsilon_{\text{eff}} + 2\varepsilon_m} = f_v \frac{\varepsilon(\lambda) - \varepsilon_m}{\varepsilon(\lambda) + 2\varepsilon_m} \quad (2.100)$$

Here, the effective RI of the hydrogel without NMNPs can also be estimated by modeling each monomer component as a dipole. $\varepsilon(\lambda)$ is assumed to be constant for λ , and the volume fraction f_v is assumed to be composed of the volume of monomers and volume of solvent in the hydrogel found from the wt% in (2.95) and (2.96). If the hydrogel consists of NMNPs as dipoles, $\varepsilon(\lambda)$ is dependent on λ , and the effective RI can be described as a function of polarizability

$$\varepsilon_{\text{eff}} = \varepsilon_m + \frac{3\varepsilon_m}{\frac{3f\varepsilon_m}{4\pi\alpha} - 1} \quad (2.101)$$

From (2.101) it is shown that the largest effective RI is when α is maximized at the plasmon resonance condition [117].

2.5.3 Sensor Implementation with a Double-Clad Optical Fiber

The FO sensor system combining LSPR and interferometric sensor modalities can be configured as shown in Fig. 2.19 [37], [110]. The hydrogel can be fabricated

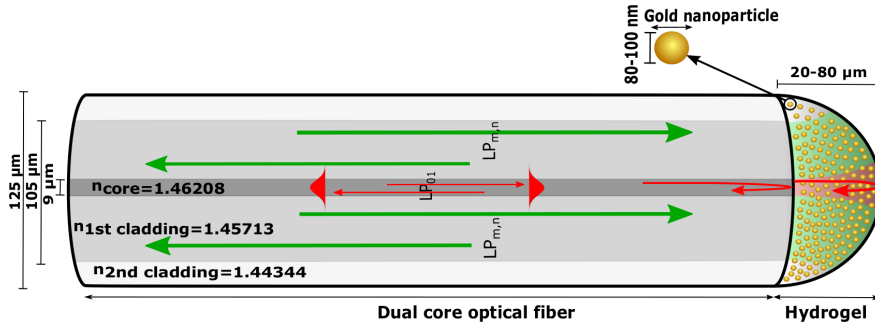


Fig. 2.19: Illustration of the dual core FO sensor combining LSPR and interferometric sensor modalities. As colored with red, IR light is confined to a single transverse mode both in the fiber inner core and hydrogel with reflection at OF-hydrogel and hydrogel-solution interface. As colored with green, VIS light is confined as MM in the larger core with a larger NA than the IR light in the inner core. LSPR is measured with VIS light while the FP interferometer is measured with the IR light. The illustration is from [37].

as described in Section 2.3.3. The sensing modalities are combined by using a double-clad optical fiber (DCOF) that consist of a small core and a large core-cladding, with NMNPs immobilized in a hydrogel on the OF end face. The IR light is confined into a single transverse mode in an OF core and in a hydrogel (noted as red in Fig. 2.19) with effective interference between the field reflected at the OF-hydrogel

interface and the field reflected at the hydrogel-solution interface. The hydrogel is a low-finesse FP in this system since $r_1 r_2 \ll 1$. The EFPI can then be interrogated in the same way as the FO system in Fig. 2.14. The MM first cladding-core is guiding the VIS light and is used for probing the LSPR of the NMNPs (noted as green in Fig. 2.19). The high NA of the large diameter core ensures effective excitation of a significant fraction of the NMNPs immobilized in the hydrogel and effective collection of scattering from the LSPR of the NMNPs. The LSPR signal can then be interrogated in the same way as in the FO system in Fig. 2.17. The mode-coupling between the SM core and MM first cladding is negligible due to the short propagation distances used (few meters).

A DCOF coupler is utilized to separate the MM and SM fields as shown in Fig. 2.20. Most of the SM light is coupled to the IR spectrometer while most of the

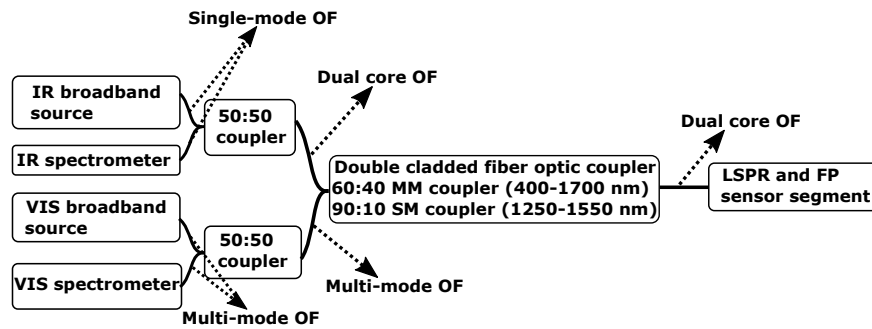


Fig. 2.20: Diagram of the FO instrument combining LSPR and interferometric sensor modalities with DCOF. The illustration is from [37].

MM light is coupled to the VIS spectrometer. As mentioned in Section 2.3.3 and 2.4.5, a large number of modes in the FP cavity leads to zero visibility interference, while for a single mode in the FP cavity leads to a high visibility interference. The interference is thus suppressed for the LSPR spectrum with VIS light, while effective interference occurs for the hydrogel FP cavity with IR light.

Concerning the hydrogel composition and NMNPs there are conflicting requirements for the two sensing modalities. For high polymer density hydrogel and low NMNP ND it is possible to obtain high visibility of the interference signal whereas a high LSPR signal is obtained for a hydrogel with high NMNP ND. With low polymer density hydrogel, it is possible to reduce the effect of polymer chains in near the plasmon wave as well as allowing analyte diffusion into the hydrogel volume. High NMNP ND may also induce dipole-dipole interactions that will shift the LSPR for hydrogel swelling or contraction. Hence, the hydrogel composition and NMNP ND must be tailored to reach the desired interferometric and LSPR sensing requirements to minimize any cross-talk or to reach the sensing requirements as defined by the

application in mind. For a configuration where LSPR is utilized for sensing the receptor-analyte recombination and where the interferometer is used for sensing the hydrogel swelling, the polymer density should be low and the NMNP ND should be optimized, so no dipole-dipole interactions are induced. In this situation, the optical path changes caused by the significant physical swelling will dominate over the minute change in bulk RI, while the LSPR shifts will be dominated by the analyte binding to the surface rather than the density of the polymer chains.

2.6 Characterizing Origin of Observed Signals

In Section 2.5.1 an NNDF model for describing the probability of having particles separated at different distances is presented. The distribution of particles may influence the amplitude and linewidth of LSPR signals from dipole-dipole coupled NMNPs. The NNDF can also be used to estimate the amount of dipole-dipole interactions present in the LSPR signal. Although the NNDF model is useful for describing the spatial distribution of particles, it is only valid for a truly random distribution. Since the surface charge of NMNPs ensures an efficient dispersion, any disruption of these electrostatic repulsive forces would lead to inhomogeneous particle distributions. Agglomeration of NMNPs can be estimated by measuring the visibility of the interferometric modality of the OF sensor system presented in Section 2.5.3. The visibility measurements can detect highly agglomerated particle-clusters but would not be able to detect agglomeration at the OF end face, hydrogel-solution interface or agglomeration on the polymer network. However, the particle distribution may be successfully characterized by using volume imaging methods such as the focused ion beam-scanning electron microscope (FIB-SEM) or the serial block-face scanning electron microscopy (SBFSEM) techniques [118]–[122]. Therefore, this section concerns the presentation of particle distribution models assumed to exist for the NMNP-hydrogels as well as some remarks concerning challenges in preparing hydrogels for SEM as the hydrogel structure is contained by the water absorbed in the polymer network.

2.6.1 Model for Particle Distributions in Hydrogel

The NMNPs in hydrogels may exhibit different types of particle distributions as illustrated in Fig. 2.21. A random distribution of particles may exist at the optimal pH and ion strength of the gel resulting in sufficiently charged NMNP surfaces. The OF end face, hydrogel-solution interface and the polymer network is in this condition also electrostatically repulsive to the NMNP with a polymer network that is sterically immobilizing them. The amount of dipole-dipole coupling of NMNP is then possible to model from the particle distribution model (2.87) in Section 2.5.1. Particles may also be distributed on the OF end face. This can occur as the result of binding to functionalized surfaces (silane, biotin-antigen, negative or positively charged) due

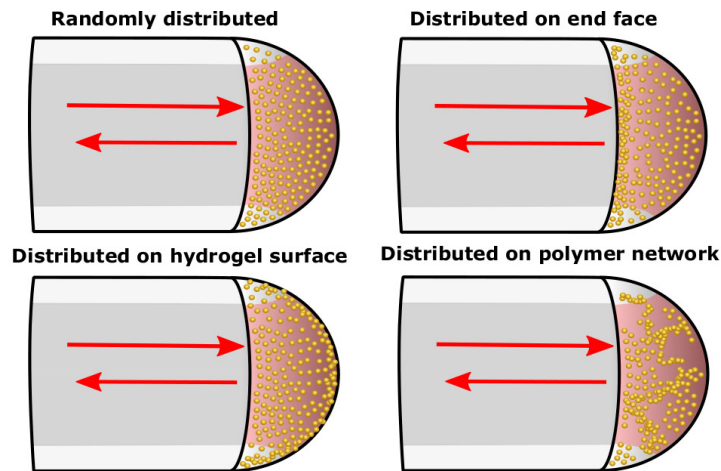


Fig. 2.21: Random and inhomogeneous distributions of particles in a hydrogel.

to the disruption of the surface charge of the NMNPs or as a result of covalent or non-covalent bonds between the surface and NMNPs. The LSPR response and signal from the particle assemblies on the OF end face may dominate over or significantly blend with the LSPR response and signal from the particles distributed in the gel.

Depending on the stabilizing agent used on the NMNP surface, liquid-liquid interface assembly may occur on the hydrogel-liquid (oil, water, solvent) interface. For highly ordered assemblies this may increase the reflection of light at the hydrogel-liquid (oil, water, solvent) interface [123], [124], and result in detecting the extinction of NMNPs rather than the scattering. Another particle distribution may occur due to the interactions between the polymer network and NMNPs. Anionic or cationic polymer networks in hydrogels may attract NMNPs with an opposite surface charge and form assemblies along the pore structures in the hydrogel. The LSPR response and signal here is a function of the assembled and close-packed NMNPs on the hydrogel polymer structure. Particle distributions in hydrogels can be studied by using FIB-SEM or the SBFSEM techniques [118]–[122]. Electron microscopy techniques require the samples to be in a vacuum and will propose challenges for conserving the native hydrated state since its structure is contained by the water absorbed in the polymer network. The structure of the hydrogel can be conserved by choosing appropriate preparation methods, which also depends on the composition of the hydrogel.

2.6.2 Hydrogel and Electron Microscopy – A Few Remarks

Imaging of NMNPs is possible by employing the SEM technique where an electron beam with Ångström electron wavelength is utilized for scanning the

sample, that is lowering the diffraction limit as compared to using a light beam with nm wavelengths in optical microscopes [125]. The incident electron-beam is interacting with the sample as illustrated in Fig. 2.22. High beam voltage results

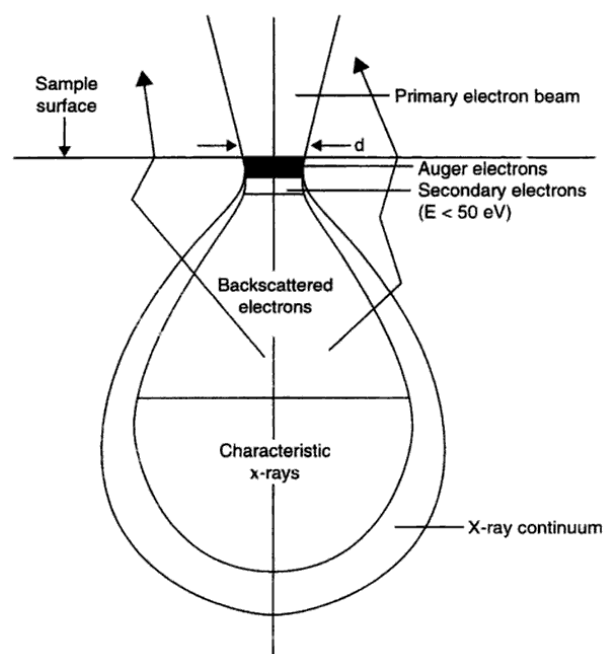


Fig. 2.22: Beam range and interaction with the sample in SEM imaging. The illustration is from [125].

in mostly backscattering electrons (BSE) and x-ray characteristics while low beam voltage results in mostly Auger electrons and secondary electrons (SE). SE detection from the sample is often used for studying the morphology of low-density materials and BSE detection from the sample is often used for studying the morphology of high-density materials. By having a high and low density material matrix, it is possible to select what type of materials that is supposed to be characterized by using high or low beam voltage resulting in high SE or BSE intensities, respectively. Hence, NMNPs can be characterized in hydrogels by using high beam voltage and BSE detectors since metal nanoparticles are denser than the polymer network.

To study particle distribution of NMNP-hydrogels in SEM, an appropriate method have to be chosen for conserving the hydrogel structure. Pore structures of hydrogels can be conserved by using different drying methods such as high or low-temperature drying [126]–[128] or critical point drying (CPD) [127], [129]–[131]. However, it is still difficult to prevent collapsing characteristics from occurring for these drying methods [127], [132], [133]. Any degree of hydrogel collapse will also result in

close-packing of the NMNPs. By comparing images from conventional SEM with specialized SEM techniques such as cryoSEM or environmental-SEM [129], [134], it is possible to estimate the presence of these collapsing features. The contrast of NMNP in gel-like samples may be further improved by omitting the sample metal coating and instead include highly conductive sample holders [135], or by using both SE and BSE detectors to obtain density dependent contrasts that highlights the high densities areas in the image [136]. Imaging with the transmission electron microscopy (TELM) can successfully characterize the particle distributions of metal nanoparticles. This also requires the sample to be cut into nanometer thick slices.

In the work presented in this thesis, efforts have been made to map the metal nanoparticle distributions in hydrogels by using electron microscopy [137]. The hydrogels were prepared by fixation, dehydration and drying. From experience, it was found that hydrogels do efficiently rehydrate. This results in challenges concerning hydrogel collapse or challenges in performing ultramicrotomy for TELM. In ultramicrotomy the sample has to be cut with a diamond knife on top of a water surface. Cutting the fixated, dehydrated and dried hydrogels on top of a water surface is rehydrating the hydrogel and results in dissociation. Hence, TELM imaging of hydrogels becomes a complicated approach suddenly. However, the morphology of the fixated, dehydrated and dried NMNP-hydrogel structures can be observed by using conventional SEM. Small-sized contrast features are also observable for high beam voltage and with BSE detector that indicates the presence of NMNPs. The mapping of the particle distributions can then be performed with volume imaging methods such as the FIB-SEM or the SBFSEM techniques [118]–[122]. The degree of collapse and other artifacts [138] are however uncertain for dried hydrogels in conventional SEM but can be estimated by comparing results with cryoSEM or environmental-SEM images [139].

Summary and Discussion of Papers

3.1 Summary

3.1.1 Paper I

In paper I, an LSPR based OF architecture in reflection fabricated by immobilizing GNPs in a hydrogel on the FO end face was reported. The LSPR of the GNP in the hydrogel can be used for detecting receptor-analyte recombinations, for SERS, or used as a plasmon ruler for detecting changes in the hydrogel swelling equilibriums. By using different NMNPs of different size and shape they may also be used for multianalyte sensing in complex mixtures. The immobilization of GNP in hydrogels has some advantages over earlier designs that utilize the LSPR of noble metal structures on the OF side or end face; (1) a large number of GNPs in hydrogel results in strong LSPR signal; (2) precise control of GNP density and (3) free standing GNPs available for sensing in a three-dimensional aqueous environment. The sensor integration on the OF end face results in more straightforward manufacturing methods as compared to utilizing the side face since there is no need for cladding removal. Also, by using a MM OF it ensures a high LSPR signal as a result of the high numerical aperture exciting a significant fraction of the GNPs and effective collection of scattering from the LSPR of the GNPs.

The results were presented as proof-of-concept experiments that explore the LSPR and interparticle distance distribution attributes of the OF design with GNP-hydrogel on the OF end face. Changes in the hydrogel swelling equilibriums were controlled with pH solutions for different initial NDs of GNPs in the hydrogel. The hydrogel deswelling results in increasing the RI as well as an increase in the GNP density that may redshift the LSPR wavelength. From estimating deswelling hydrogel volumes with GNPs in an optical microscope, the NNDF of the particles could be computed. It was found from these measurements that the interparticle distances are too large for dipole-dipole coupling to occur for the GNP densities used in our experiments. These observations were in contradiction with the obtained reflection spectra of the GNP-hydrogel on the OF end face. For the highest ND used, the LSPR wavelength was dependent on the interparticle distances. Hence, for the GNP densities used in our experiments, the interparticle distances are small enough for plasmon coupling to occur. Considering that the NNDF is only valid

for a genuine random particle distribution, this suggests that the particles in the hydrogel might be inhomogeneously distributed. The assumption of dipole-dipole coupling was consistent with the changes in the estimated FWHM of the LSPR signal for hydrogel deswelling. The amplitude of the LSPR signal was measured for hydrogel deswelling and was found to be decreasing. The decreasing amplitude for decreasing interparticle distances suggests that higher GNP densities result in a more significant dispersion in particle scattering caused by the increased fraction of particles interacting and by the increased variations in local RI.

In summary, a new LSPR FO system was developed by immobilizing a GNP-hydrogel on the OF end face and characterized by performing proof-of-concept experiments to explore its LSPR and interparticle distance distribution attributes. The LSPR response shows not only to be dependent on the initial GNP densities for different hydrogel swelling equilibriums but also shows to be dependent on how the GNPs are distributed. By controlling the GNP densities and hydrogel compositions, this FO system may be used for detecting receptor-analyte recombinations, for SERS, or used as a plasmon ruler for detecting changes in the hydrogel swelling equilibriums.

3.1.2 Paper II

In paper II, a new single-point multiparameter FO sensor concept based on a combination of interferometric and plasmonic sensor modalities on a DCOF end face was demonstrated. The sensor consists of an EFPI in the form of a hemispherical hydrogel embedded with spherical GNPs that exhibit LSPR. The LSPR of the GNPs is sensitive to the RI of the surrounding environment, whereas the volume-responsive hydrogel is sensitive to specific chemical compounds. The LSPR of the GNPs are measured in the VIS range, and the EFPI is measured in the IR range. The two sensing modalities are combined by using a DCOF, where VIS MMs are guided in the first cladding, and IR SM is guided in the core. The VIS MMs in the first cladding and hydrogel ensures high numerical aperture for collection and excitation of the LSPR of the GNP and ensures interference suppression due to a large number of modes. The IR SM confined in core and hydrogel enables accurate interferometric measurements, which avoids the limitation of modal dispersion in MM EFPI.

The quality and cross-sensitivity of the interferometric and plasmonic sensing modalities were assessed by measuring the visibility of the EFPI for different GNP densities, the LSPRs of the GNPs for different hydrogel swelling equilibriums and the FSRs for different GNP densities and hydrogel swelling equilibriums. The hydrogel deswelling was controlled with increasing ethanol concentrations. Despite having the GNPs immobilized in the hydrogel, the visibility was measured to be near constant with small fluctuations for increasing GNP densities. The FSR of the EFPI measured for hydrogel deswelling was increasing monotonically for low

and high GNP densities. It was concluded that the visibility and the sensitivity of the EFPI sensor with GNPs are similar to previous work and sufficient for many applications. The LSPR wavelength showed to have small variances within 2 nm for the deswelling GNP-hydrogel. It was concluded from this that the hydrogel deswelling is not increasing the local RI but rather introducing small variations in the dielectric environment on the surfaces of the GNPs. Also, no interference fringes were observable in the VIS range due to the washed out interference in the MM DCOF. The quality of the LSPR signal was comparable to other OF end face based LSPR sensors.

In summary, interferometric and plasmonic sensing modalities were combined by using a hydrogel embedded with GNPs immobilized on a DCOF end face. The quality and cross-sensitivity of the two sensing modalities were assessed by measuring the visibility for GNP densities, the FSR for hydrogel deswelling and the LSPR for hydrogel deswelling. Results from this proof-of-concept demonstration proved the utility of immobilizing GNPs in hydrogels to measure both interferometric and LSPR signals with acceptable levels of cross-talk to obtain label-free and selective sensing of specific biomolecules for medical purposes.

3.1.3 Paper III

In paper III, the effect of the GNP shape, the hydrogel swelling degree, the bulk RI and the feasibility of using LSPR of GNP-hydrogels for biosensing were further studied as a continuation of the FO system developed in paper II. Spherical GNPs were exchanged with gold nanorods (GNR) and the hydrogel was composed of poly(acrylamide-co-acrylic acid) instead of polyacrylamide. Hence, the hydrogel swelling can be controlled with pH solutions instead of ethanol concentrations. The LSPR response from RI changes was assessed with glycerol and sucrose solutions and the biosensing functionality of the GNRs was assessed with biotin-streptavidin recombinations. The EFPI was interrogated with IR light, and the LSPR of the GNRs were interrogated with VIS-IR light (450-850 nm). As for the FO sensor system in paper II, the high numerical aperture of the MM first cladding with VIS-IR light enables efficient excitation and collection of the LSPR of the GNRs. The interference in the LSPR spectrum is suppressed due to a large number of modes in the first cladding and hydrogel as well as due to the modal dispersion in the MM first cladding of the DCOF. Using the SM core of the DCOF for the EFPI enables high visibility interference spectra and avoids the limitation of modal dispersion in MM fiber and fiber tip FP cavity.

The characterization of the interferometric and plasmonic sensing modalities was performed by controlling the hydrogel swelling with pH solutions and varying the bulk RI with glycerol solutions as well as by varying the local RI with biotin-streptavidin recombinations on the GNR surface. The pH induced hydrogel swelling

caused weak redshifts of the longitudinal LSPR mode of the GNRs while increasing the bulk RI caused significant blueshifts. The redshift with hydrogel swelling was concluded to be due to the reduced plasmon coupling in the s-s configuration for increasing interparticle distances. The total redshift was measured to be less than 1 nm for a volume-swelling degree of 6. For smaller cavity length changes, the LSPR variations will be negligible and sufficient for many biosensing applications. The blueshift for increasing bulk RI was concluded to be due to the alteration of the surface electronic structure of the GNRs donated by the anionic poly(acrylamide-co-acrylic acid) polymer network and the glycerol and sucrose solutions. Hence, care must be taken when using this sensor concept for bulk RI sensing. The increasing local RI for biotin-streptavidin recombinations on the GNRs was redshifting the longitudinal LSPR by 7.6 nm, which demonstrated the effect and differences between bulk and local RI sensing. Last, the FSR was found to be increasing monotonically for deswelling hydrogels induced with pH solutions. The EFPI signal quality and the response were concluded to be comparable to previous work and sufficient for many biosensing applications.

In summary, the characterization of a multiparametric LSPR and interferometric FO sensor has been conducted for different hydrogel swelling degrees, bulk RI and local RI. The FSR and LSPR measurements from hydrogel swelling degrees and biotin-recombinations proves the utility of immobilizing GNRs in hydrogels to measure both interferometric and LSPR signals with an acceptable level of cross-talk for use in medical or biological applications.

3.1.4 Paper IV

In paper IV, a comparison was made of different preparation methods of hydrogels for conventional SEM as an effort in developing methods to map NMNP distributions with volume imaging methods such as the FIB-SEM or the SBFSEM techniques. The nanoplasmonic response for the LSPR sensors presented in paper I to III shows to be dependent on the orientation of the spheroidal NMNPs as well as the distribution of the NMNPs. The orientation and the distribution of particles in the hydrogel are mainly controlled by the self-assembly kinetics occurring in the hydrogel synthesis. Thus, to assess the particle self-assembly and distribution, volume imaging methods can be used for characterizing the morphology of the NMNP-hydrogels. The pore structure of hydrogels is contained by the water absorbed in the polymer network and pose challenges for FIB-SEM or SBFSEM volume-imaging since the sample must be in a vacuum chamber. By choosing appropriate preparation methods, the structure of the hydrogel can be conserved in a vacuum. The hydrogels were thus prepared for conventional SEM by using two drying methods; the critical point drying (CPD) technique and the drying of hydrogels in hexamethyldisilazane (HMDS) solvent.

The results present SEM images of hydrogels with and without GNRs in SE and BSE mode. The morphology of CPD and dried hydrogels in HMDS shows to have comparable pore structures. This shows that drying with HMDS serves as a suitable alternative to the CPD technique. Drying with HMDS is a cost-effective substitution of the CPD technique that omits equipment use as well as it involves less parametrical variables in the drying. The pore structures of anionic poly(acrylamide-co-acrylic acid) hydrogels show to have more irregular structures than polyacrylamide hydrogels. This observation may be due to the more significant hydrophilicity of the anionic poly(acrylamide-co-acrylic acid) hydrogels. The pore structures of hydrogels should be assessed with care since most dried hydrogels exhibit collapsing features due to rehydration after the dehydration and drying process. The dehydration process with ethanol is making the hydrogel contract significantly. The hydrogel pores structures observed in this paper can, therefore, be assumed to be smaller than pore structures for hydrogels in their hydrated native state. Small-sized and high contrast features were observable in the BSE SEM images of GNR-hydrogels, which could indicate the presence of GNRs, since they are denser than the polymer network. The obtained contrast of GNRs was low and difficult to distinguish from artifacts associated with the sample preparations. The contrast of NMNPs in a low density matrix can be enhanced by using highly conductive sample holders or by combining SE and BSE images to map the density contrasts.

In summary, the preparation methods of hydrogels with and without GNRs have been qualitatively assessed in conventional SEM as a precursor in developing methods for mapping particle distributions in hydrogels with FIB-SEM or SBFSEM techniques. To identify the spatial positions of the GNRs in the hydrogel, the contrast needs to be enhanced with highly conductive sample holders or by using both SE and BSE images to map the density contrast. Drying with HMDS can be used instead of the CPD technique that omits the use of equipment and reduces the cost. Choosing an optimized sample preparation method for SEM with optimized imaging parameters is also highly essential for obtaining accurate information about materials that are not correlated to artifacts. Hence, the results obtained from the preparation methods and SEM imaging parameters in this paper are useful in developing methods for mapping the NMNP distributions in micro-hydrogels by using FIB-SEM or SBFSEM techniques.

3.2 Discussion

New and improved monitoring of complex multi-variable environments often relies on the diversity and the implementation of new sensor technologies. The sensor is often designed as defined by the application in mind with requirements such as fast response times, high selectivity, high sensitivity, robustness, multiplexing possibilities, remote sensing possibility, label-free sensing, or possibility for miniatur-

ization. In some cases, the working environment may also expose the sensor to high temperatures, corrosive entities, or high electro-magnetic fields. There are no sensor designs that will satisfy all the requirements. Hence, a library of sensor designs is useful for finding balanced solutions between the requirements and cost-effectiveness. For biochemical sensors, miniaturization is a vital objective since smaller sizes lead to faster diffusion times and sensor responses. For medical applications, miniaturization enables sensor insertion into small sample volumes, tissues or vessels. OF waveguides show to be a popular technology platform concerning remote sensing and sensor miniaturization. Also, OF based sensors are immune to electro-magnetic interference and can monitor in high temperatures and corrosive environments. The light-matter interactions in the sensor integrated on the OF can be measured as a function of amplitude, frequency, polarization or phase. Thus, the modulation of light properties offers many possibilities for signal multiplexing that can be applied for multiparametric sensing of complex multivariable environments.

The work presented in this thesis focuses on using interferometric and nanoplasmonic sensing modalities with OF label-free sensor systems for multianalyte monitoring at a single point. Light may only be frequency modulated to interrogate both of the sensing modalities. The interferometric sensing can be performed by detecting the length changes in a FP cavity by observing the phase changes of the sinusoidal spectra in the IR light-range. The LSPR sensing can be performed by detecting the local RI changes on the NMNP surfaces by measuring the resonance frequency shifts of the Lorentzian spectra in the VIS-IR light-range. Results and experiences from the earlier developed EFPI OF sensor designs enabled the implementation of LSPR biosensing by immobilizing NMNPs in the FP cavity. The nanoplasmonic concept was explored first in paper I, by measuring the reflectance of spherical GNPs embedded in hydrogel immobilized on a MM OF end face for different NDs and hydrogel swelling equilibriums. The LSPR attributes of the GNPs in the three-dimensional hydrogel polymer network were characterized by varying the initial ND in different hydrogel swelling equilibriums. From these measurements, it was found that increasing initial GNP densities changed the LSPR response for hydrogel deswelling from being dominated by the local RI changes in the hydrogel, to being dominated by the reduced interparticle distance inducing dipole-dipole coupling. These observations stood in contrast to the particle distribution model used, that indicated the interparticle distances to be much larger than the distance for inducing dipole-dipole coupling. This model predicts interparticle distances for a genuine random distributed interparticle distribution. Thus, the LSPR of GNPs embedded in the hydrogel is not only dependent on local variations of the RI or the interparticle distances inducing dipole-dipole coupling, but it is also dependent on how the particles are distributed in the hydrogel.

The results obtained from paper I gave detailed insight into the LSPR response characteristics from the reflection of GNPs in hydrogels but left some unanswered questions such as, how are the particles distributed? Is there any degree of particle agglomeration in the hydrogel? By combining interferometric detection of cavity length changes of the swelling hydrogel with the LSPR based RI sensing in paper II, these questions might be answered. The visibility of the low finesse interference of light in the hydrogel cavity in reflection depends on absorption, scattering and mode mismatching. Hence, the degree of particle agglomeration would significantly influence the visibility of the interferometer. By combining interferometric and nanoplasmonic sensing modalities based on using the reflection of GNP-hydrogel on a DCOF end face, a proof-of-concept sensor by sensing two parameters in a single point was also demonstrated. The quality of the EFPI sensor was assessed by measuring the visibility as a function of GNP densities as well as by measuring the FP cavity lengths for different hydrogel swelling equilibriums with different GNP densities. The quality of the LSPR sensor was assessed by measuring the resonance wavelength as a function of hydrogel contraction. From the visibility measurements, it was found that the GNPs are well dispersed through the hydrogel and a strong LSPR signal can be achieved with the GNP densities used for this sensor without reducing the quality of the EFPI signal. The FP cavity length measurements indicated that the EFPI sensor response is comparable to earlier work that utilizes hydrogels without NMNPs. The LSPR wavelength measurements show that the local RI variations for different hydrogel swelling equilibriums are sufficiently small enough not to introduce artifacts in the detection of receptor-analyte recombinations. The interference was also washed out efficiently in the LSPR spectra due to the large number of modes in the fiber and FP cavity, as well as due to the modal dispersion in the MM DCOF.

From the results in paper II, it was concluded that the particle dispersion degree could be observed through the visibility measurements and that it would serve as a good indicator for assessing the quality of both interferometric and LSPR signals. The EFPI and LSPR cross-sensitivity or cross-talk were small and the signal quality was comparable to other work. This demonstrates the utility of immobilizing NMNPs in hydrogels for measuring both interferometric and LSPR signals to obtain label-free and selective sensing of specific biomolecules for medical or biological purpose. Whereas the effect of embedding spherical GNPs in the hydrogel FP cavity as well as the feasibility of using GNP-hydrogel for LSPR sensing have been elucidated in paper II, other parameters such as the effect of particle shape, bulk RI and LSPR biosensing, have been left undiscussed. Thus, the sensor characterization performed in paper II is continued in paper III by exchanging the spherical GNPs with spheroidal GNRs, by making the hydrogel responsive to pH instead of ethanol, and by functionalizing the GNRs with biotin for detecting biotin-streptavidin recombinations. The FP cavity lengths and LSPR wavelengths were measured for different pH and bulk RI solutions

to assess the cross-sensitivity of the signals, whereas the LSPR response to local RI changes was assessed by detecting biotin-streptavidin recombination on the GNR surfaces. Two anomalies were observed in this proof-of-concept demonstration; (1) an absorption dip was observed instead of the expected scattering peak of the LSPR signal; (2) when increasing the bulk RI controlled with glycerol or sucrose solutions, the LSPR wavelength was blueshifting instead of the expected redshifting. A reason for the first anomaly could be that there are reflection points (self assembled gold mirrors) in proximity to the OF end face, inside the hydrogel or on the surface of the hydrogel that is increasing the influence of the extinction coefficient (reflections result in transmission through GNRs to the OF) so it dominates over the influence of the scattering coefficient (reflection from individual GNRs only). A reason for the second anomaly could be that the LSPR is responding to changes in the metal-dielectric function as a result of CID or as a result of a change in the electron density in the GNRs. The difference between the LSPR response for bulk RI and local RI changes were demonstrated from the biotin-streptavidin recombinations resulting in a redshift. Despite the anomalies observed, local RI changes could be detected from the LSPR wavelength redshift measurements from the biotin-streptavidin recombinations, while negligible LSPR wavelength blueshifts (plasmon coupling in the s-s configuration) were observed for hydrogel deswelling. Thus, the cross-talk is small between the interferometric and LSPR sensing modalities and sufficient for biosensing in medical or biological applications. The LSPR blueshifts for hydrogel deswelling were an interesting observation as it indicates plasmon coupling of GNRs in the s-s configuration. This suggests an organized orientation of the GNRs in the hydrogel.

The first anomaly, where the reflection from GNRs in hydrogel results in a absorption dip instead of a scattering peak, raises again the question that was posed in paper I, how are the particles distributed in the hydrogel? The distribution and orientation of the NMNPs in hydrogels may result in unexpected nanoplasmonic features. This self-assembly of particles might be controlled kinetically in the hydrogel synthesis. The study of particle distributions in NMNP-hydrogels may elucidate their nanoplasmonic properties. In paper IV, effort was made in the preparation of NMNP-hydrogels for conventional SEM to characterize the particle distributions, as a precursor for volume-imaging NMNP-hydrogels with FIB-SEM or SBFSEM. SEM images in SE and BSE mode were obtained for polyacrylamide and poly(acrylamide-co-acrylamide) hydrogels with and without GNRs, and were CPD or dried with HMDS before imaging. It was concluded from these results that the contrast of the GNRs is not high enough to distinguish them from artifacts associated with the sample preparations. The hydrogel may also contain collapsing features that would lead to a close-packing of the GNRs. Thus, some improvements are necessary to obtain any quantitative information about the particle distribution in hydrogels. The results can be used qualitatively in developing preparation methods for volume

imaging of NMNP-hydrogels with FIB-SEM and SBFSEM, or for characterizing pore structures of hydrogels.

Paper I and paper II-III can be perceived as a presentation of two different proof-of-concept sensor systems, whereas paper IV can be perceived as a further investigation of the results obtained from paper I to III. In paper I, the FO sensor can be used for detecting receptor-analyte recombinations, detecting significant hydrogel swelling equilibrium changes or used for SERS. In paper II and III, the FO sensor can be used for detecting length changes of stimuli responsive hydrogels based on the EFPI, whereas the LSPR of NMNP can be used for detecting receptor-analyte recombinations or used for SERS. For real-life biosensing, the composition of the hydrogel, type of NMNP and ND of the NMNP for the proof-of-concept systems must be chosen as defined by the application in mind. The FO sensors are, therefore, presented in their purest form as photonic devices instead of real-life biosensors to demonstrate their general interferometric or plasmonic properties. The EFPI sensors have in earlier work been developed for glucose sensing and the LSPR of the GNRs have been used for biotin-streptavidin measurements in paper III. Thus, both the EFPI and the LSPR FO devices have been demonstrated as biosensors individually.

Conclusion and Outlook

Novel FO sensor systems have been presented in this thesis and characterized concerning fundamental interferometric and plasmonic properties in combination with a theoretical approach to understand the experimental observations of the sensing modalities. The first FO sensor concept was demonstrated by using the LSPR of the NMNP-hydrogel for sensing local RI changes on NMNP surfaces and for detecting dipole-dipole coupling between the NMNPs. This sensor concept can be used for detecting substantial changes in swelling equilibriums of stimuli-responsive hydrogels, detecting receptor-analyte recombinations, or used for SERS. SERS is possible by designing the NMNP-hydrogels so that it exhibits a large number of plasmonic hot-spots. For low NMNP densities in deswelling hydrogels, the LSPR wavelength shifts were dominated by local RI changes, whereas for high NMNP densities in deswelling hydrogels the LSPR wavelength shifts were dominated by dipole-dipole coupling. Theoretical modeling showed that the plasmon coupling effect could only be explained by assuming an inhomogeneous particle distribution in the hydrogel.

The second FO sensor concept was demonstrated by combining interferometric and LSPR sensing modalities for detecting both hydrogel swelling equilibrium changes and local RI changes in one single point. This sensor concept can be utilized to detect nm changes in hydrogel swelling equilibriums by using the EFPI as well as utilized for detecting receptor-analyte recombinations by using the LSPR of the NMNPs. It was shown by measuring the visibility for increasing GNP densities and by measuring the FP cavity lengths (FSR) for hydrogel deswelling, that the EFPI was unaffected by the particles immobilized in the hydrogel. The EFPI and LSPR sensor signal and response were concluded to be comparable to earlier work. The visibility of the EFPI could, in addition, be used for assessing the dispersion degree of the NMNPs in the hydrogel FP cavity. The bulk RI controlled with sucrose or glycerol solutions showed to induce an LSPR response that was different from the LSPR response induced by the local RI changes of analytes binding to the NMNP surfaces. The LSPR wavelength shifts for increasing bulk RI (increasing wt% of glycerol or sucrose) were assumed to be a result of CID or due to the alteration of the surface electronic structure of the NMNP donated by the monomers in the hydrogel and the glycerol or sucrose solutions. The cross-sensitivity between the EFPI and the LSPR sensor were found to be small for both spherical and spheroidal GNPs, i.e. the LSPR wavelength have negligible shifts for hydrogel deswelling. For GNRs, the small blueshifts indicated that the majority of the particles were highly organized

in the s-s configuration. The distribution of NMNPs was in fact quite uncertain for all of the FO sensors systems which led the work into characterizing the NMNP-hydrogels in conventional SEM. The hydrogels were prepared for SEM by fixation, dehydration and drying. From the results obtained and from experience it was found that hydrogels do efficiently rehydrate. The rehydration results in challenges concerning hydrogel collapse or challenges in performing ultramicrotomy for TELM. Not surprisingly, water-ultramicrotomy of hydrogel fixated in epoxy resulted in a total dissociation of the hydrogel-slices. The results from conventional SEM showed that the hydrogel morphology was intact after performing fixation, dehydration and drying, but the contrast from the NMNPs was low. Hence, some improvements are necessary for obtaining any quantitative information about the particle distribution in hydrogels. Nonetheless, the conventional SEM characterization results may be used as qualitative information to develop preparation methods for volume-imaging of NMNP-hydrogels with FIB-SEM or SBFSEM techniques.

FO waveguides may become increasingly attractive as a chemical sensor in the medical and energy industry, environmental monitoring and R&D institutions with a magnitude similar to the increasing popularity of using OF as temperature or strain sensors. This development will not only apply to OF waveguides particularly, but to both electronic and photonic sensor devices due to the increasing demand for controlling complicated chemical processes, that we now understand from the significant achievements made in basic research. Controlling and regulating complicated chemical processes opens up new possibilities in many areas, e.g. making the life-cycle of hydrogen fuel cells longer, efficient energy production from waste, detect chemical markers in blood to obtain faster treating methods for patients in intensive care units, or efficient monitoring and regulation of algae production. The applications of FO waveguides may be defined by its size, capability for remote sensing, capability for distributed sensing, or for its inert properties. Establishing the sensor on the OF end face removes the possibility for distributed sensing but several sensing parameters can be combined in a single point, as demonstrated in this thesis. The possibility for inserting the OF into small samples or volumes may serve as point-of-monitoring (not specifically medical applications). Combined with miniaturization that results in faster diffusion times, response times and cost-effective designs, OF sensors in reflection may become a favorite technology platform in both research and industry. Hydrogels have been synthesized for various applications but few have been used for biosensing due to the limited sensitivity offered by the interrogation techniques. The use of hydrogels as a low finesse FP cavity on OF end face is a prime example of how FO waveguides became the ultimate tool for detecting length changes of stimuli-responsive hydrogels accurately and used as label-free sensors. The use of GNPs as label-free sensing probes are also advantageous since they can be easily biofunctionalized, although some challenges exists concerning stability issues in high ionic strengths or in corrosive solutions that

results in particle agglomeration. Also, different NMNPs of size and shapes exhibits different LSPR. These properties are quite useful for obtaining multianalyte sensing in complex mixtures. The development of new photonic devices or sensors in this thesis may inspire others to make use of the concepts presented. Perhaps LSPR sensing can be combined with similar interferometric OF architectures, OF-LSPR sensing can be multiparametric with NMNPs of different size and shape, or maybe it is possible to achieve polarization sensitive measurements of highly ordered NMNPs in a hydrogel or another embedding matrix. Maybe noble metal nanocomposite hydrogels can be engineered to exhibit some impressive nanoplasmonic features? Only our imagination puts boundaries on the research questions that are posted.

References

- [1] Institute of Bio-Sensing Technology, „Making Sense of Sensors: Markets and Technology“, University of West of England, Institute of Bio-Sensing Technology, Bristol, Tech. Rep., 2011.
- [2] A. L. Washburn and R. C. Bailey, „Photonics-on-a-chip: recent advances in integrated waveguides as enabling detection elements for real-world, lab-on-a-chip biosensing applications“, *Analyst*, vol. 136, no. 2, pp. 227–236, 2011.
- [3] X. Bao and L. Chen, *Recent Progress in Distributed Fiber Optic Sensors*, 2012.
- [4] H. H. Gorris, T. M. Blicharz, and D. R. Walt, „Optical-fiber bundles“, *FEBS Journal*, vol. 274, no. 21, pp. 5462–5470, 2007.
- [5] S. Tierney, D. R. Hjelle, and B. T. Stokke, „Determination of Swelling of Responsive Gels with Nanometer Resolution. Fiber-Optic Based Platform for Hydrogels as Signal Transducers“, *Anal. Chem.*, vol. 80, no. 13, pp. 5086–5093, 2008.
- [6] K. Vindas, E. Engel, P. Garrigue, *et al.*, „Nano-structured optical fiber bundles for remote SPR detection: a first step toward in vivo biomolecular analysis“, vol. 10323, 2017, pp. 1 032 304–1 032 307.
- [7] M. Sanders, Y. Lin, J. Wei, T. Bono, and R. G. Lindquist, „An enhanced {LSPR} fiber-optic nanoprobe for ultrasensitive detection of protein biomarkers“, *Biosensors and Bioelectronics*, vol. 61, no. 0, pp. 95–101, 2014.
- [8] Z. Zhang, Y. Chen, H. Liu, *et al.*, „On-fiber plasmonic interferometer for multi-parameter sensing“, *Opt. Express*, vol. 23, no. 8, pp. 10 732–10 740, 2015.
- [9] B. Sciacca and T. M. Monro, „Dip Biosensor Based on Localized Surface Plasmon Resonance at the Tip of an Optical Fiber“, *Langmuir*, vol. 30, no. 3, pp. 946–954, 2014.
- [10] O. Wichterle and D. Lim, „Hydrophilic Gel for Biological Use“, *Nature*, vol. 185, pp. 117–118, 1960.
- [11] E. M. Ahmed, „Hydrogel: Preparation, characterization, and applications: A review“, *Journal of Advanced Research*, vol. 6, no. 2, pp. 105–121, 2015. arXiv: arXiv:1011.1669v3.
- [12] K. Gawel, D. Barriet, M. Sletmoen, and B. T. Stokke, *Responsive Hydrogels for Label-Free signal transduction within biosensors*, 2010.
- [13] D. R. Hjelle, A. Berg, R. Ellingsen, *et al.*, *Optical sensing of measurands*, 2008.

- [14]K. M. Mayer and J. H. Hafner, „Localized Surface Plasmon Resonance Sensors“, *Chem. Rev.*, vol. 111, no. 6, pp. 3828–3857, 2011.
- [15]T. Endo, K. Kerman, N. Nagatani, *et al.*, „Multiple Label-Free Detection of Antigen-Antibody Reaction Using Localized Surface Plasmon Resonance-Based Core-Shell Structured Nanoparticle Layer Nanochip“, *Analytical Chemistry*, vol. 78, no. 18, pp. 6465–6475, 2006.
- [16]D. Kinet, P. Mégret, K. Goossen, *et al.*, *Fiber Bragg Grating Sensors toward Structural Health Monitoring in Composite Materials: Challenges and Solutions*, 2014.
- [17]S. W. James and R. P. Tatam, „Optical fibre long-period grating sensors: Characteristics and application“, *Measurement Science & Technology*, vol. 14, no. 5, R49–R61, 2003.
- [18]S. K. Srivastava, V. Arora, S. Sapra, and B. D. Gupta, „Localized Surface Plasmon Resonance-Based Fiber Optic U-Shaped Biosensor for the Detection of Blood Glucose“, *Plasmonics*, vol. 7, no. 2, pp. 261–268, 2011.
- [19]A. B. Dahlin, „Size Matters: Problems and Advantages Associated with Highly Miniaturized Sensors“, *Sensors*, vol. 12, no. 3, pp. 3018–3036, 2012.
- [20]B. E. A. Saleh and M. C. Teich, *Fundamentals of Photonics, 2nd Edition*, B. E. A. Saleh and M. C. Teich, Eds. Wiley, 2007.
- [21]Y. J. Rao, „Recent progress in applications of in-fibre Bragg grating sensors“, *Optics and Lasers in Engineering*, vol. 31, no. 4, pp. 297–324, 1999.
- [22]M. Nakazawa, „Rayleigh backscattering theory for single-mode optical fibers“, *Journal of the Optical Society of America*, vol. 73, no. 9, p. 1175, 1983.
- [23]L. Schenato, *A Review of Distributed Fibre Optic Sensors for Geo-Hydrological Applications*, 2017.
- [24]A. Leung, P. M. Shankar, and R. Mutharasan, „A review of fiber-optic biosensors“, *Sensors and Actuators B: Chemical*, vol. 125, no. 2, pp. 688–703, 2007.
- [25]H. F. Taylor, „Fiber optic sensors based upon the Fabry-Perot interferometer“, *OPTICAL ENGINEERING-NEW YORK-MARCEL DEKKER INCORPORATED-*, vol. 76, pp. 41–74, 2002.
- [26]A. K. Sharma, R. Jha, and B. D. Gupta, „Fiber-optic sensors based on surface plasmon resonance: A comprehensive review“, *IEEE Sensors Journal*, vol. 7, no. 8, pp. 1118–1129, 2007.
- [27]J. Albert, L.-Y. Shao, and C. Caucheteur, „Tilted fiber Bragg grating sensors“, *Laser & Photonics Reviews*, vol. 7, no. 1, pp. 83–108, 2013.
- [28]T. Guo, F. Liu, B.-O. Guan, and J. Albert, „[INVITED] Tilted fiber grating mechanical and biochemical sensors“, *Optics & Laser Technology*, vol. 78, no. Part B, pp. 19–33, 2016.
- [29]T. Allsop, R. Neal, S. Rehman, *et al.*, „Generation of infrared surface plasmon resonances with high refractive index sensitivity utilizing tilted fiber Bragg gratings.“, *Applied optics*, vol. 46, no. 22, pp. 5456–60, 2007.
- [30]C. Caucheteur, Y. Shevchenko, L.-Y. Shao, M. Wuilpart, and J. Albert, „High resolution interrogation of tilted fiber grating SPR sensors from polarization properties measurement.“, *Optics express*, vol. 19, no. 2, pp. 1656–1664, 2011.

- [31]S. A. Maier, *Plasmonics: Fundamentals and applications*. Springer Science & Business Media, 2007, pp. 1–223. arXiv: arXiv:1011.1669v3.
- [32]W. Yao, R. H. Byrne, and R. D. Waterbury, „Determination of nanomolar concentrations of nitrite and nitrate in natural waters using long path length absorbance spectroscopy“, *Environmental Science and Technology*, vol. 32, no. 17, pp. 2646–2649, 1998.
- [33]Y. Lin, Y. Zou, and R. G. Lindquist, „A reflection-based localized surface plasmon resonance fiber-optic probe for biochemical sensing“, *Biomed. Opt. Express*, vol. 2, no. 3, pp. 478–484, 2011.
- [34]J. Homola, „Surface plasmon resonance sensors for detection of chemical and biological species“, *Chemical Reviews*, vol. 108, no. 2, pp. 462–493, 2008.
- [35]F. G. Banica, *Chemical Sensors and Biosensors: Fundamentals and Applications*. John Wiley & Sons, 2012. arXiv: arXiv:1011.1669v3.
- [36]H. Kuwata, H. Tamaru, K. Esumi, and K. Miyano, „Resonant light scattering from metal nanoparticles: Practical analysis beyond rayleigh approximation“, *Applied Physics Letters*, vol. 83, no. 22, pp. 4625–4627, 2003.
- [37]H. I.D.I. H. Muri, A. Bano, and D. R. D. Hjelme, „A Single-Point , Multiparameter , Fiber Optic Sensor Based on a Combination of Interferometry and LSPR“, *Journal of Lightwave Technology*, vol. 36, no. 4, pp. 1159–1167, 2018.
- [38]P. K. Jain and M. A. El-Sayed, „Plasmonic coupling in noble metal nanostructures“, *Chemical Physics Letters*, vol. 487, no. 4–6, pp. 153–164, 2010.
- [39]M. I. Stockman, „Nanoplasmonics: past, present, and glimpse into future“, *Optics Express*, vol. 19, no. 22, p. 22 029, 2011. arXiv: 1106.1690.
- [40]A. C. Donahue and M. Albitar, „Antibodies in biosensing“, in *Recognition Receptors in Biosensors*, M. Zourob, Ed., New York, NY: Springer New York, 2010, pp. 221–248.
- [41]E. P. Jonášová and B. T. Stokke, „Bioresponsive DNA-co-polymer hydrogels for fabrication of sensors“, *Current Opinion in Colloid and Interface Science*, vol. 26, pp. 1–8, 2016.
- [42]R Byron Bird, W. E. Stewart, and E. R. Lightfoot, *Transport Phenomena*, ser. Wiley International edition. Wiley, 1960.
- [43]N Lakshminarayanaiah, „Transport Phenomena in Artificial Membranes“, *Chem. Rev.*, vol. 65, no. 5, pp. 491–565, 1965.
- [44]M. Tokita, *Transport Phenomena in Gel*, 2016.
- [45]G. Gerlach, M. Guenther, G. Suchanek, *et al.*, „Application of sensitive hydrogels in chemical and pH sensors“, *Macromolecular Symposia*, vol. 210, no. 1, pp. 403–410, 2004.
- [46]H. Suzuki and A. Kumagai, „A disposable biosensor employing a glucose-sensitive biochemomechanical gel“, *Biosensors and Bioelectronics*, vol. 18, no. 10, pp. 1289–1297, 2003.
- [47]Y.-J. J. Lee, S. a. Pruzinsky, and P. V. Braun, „Glucose-Sensitive Inverse Opal Hydrogels: Analysis of Optical Diffraction Response“, *Langmuir*, vol. 20, no. 8, pp. 3096–3106, 2004.

- [48]A. J. Marshall, D. S. Young, S. Kabilan, *et al.*, „Holographic sensors for the determination of ionic strength“, *Analytica Chimica Acta*, vol. 527, no. 1, pp. 13–20, 2004.
- [49]F. J. Arregui, Z. Ciauurriz, M. Oneca, and I. R. Matias, „An experimental study about hydrogels for the fabrication of optical fiber humidity sensors“, *Sensors and Actuators, B: Chemical*, vol. 96, no. 1-2, pp. 165–172, 2003.
- [50]B. P. Abbott, R. Abbott, T. D. Abbott, *et al.*, „Observation of gravitational waves from a binary black hole merger“, *Physical Review Letters*, vol. 116, no. 6, p. 61 102, 2016. arXiv: 1602.03837.
- [51]B. P. A. Collaboration, R Abbott, T. D. Abbott, *et al.*, „Astrophysical Implications of the Binary Black-hole Merger GW150914“, *The Astrophysical Journal Letters*, vol. 818, no. 2, p. L22, 2016.
- [52]D. Castelvecchi and A. Witze, „Einstein’s gravitational waves found at last“, *Nature*, pp. 1–18, 2016.
- [53]Y.-J. Rao, „Recent progress in fiber-optic extrinsic Fabry-Perot interferometric sensors“, vol. 12, no. 3, pp. 227–237, 2006.
- [54]G. E. P. Box, G. M. Jenkins, G. C. Reinsel, and G. M. Ljung, *Time series analysis: forecasting and control*. John Wiley & Sons, 2015.
- [55]Y. L. Lo and J. S. Sirkis, „Passive Demodulation Techniques for Michelson and Polarimetric Optical Fiber Sensors“, *Experimental Techniques*, vol. 19, no. 3, pp. 23–27, 1995.
- [56]I. Bartholsen and D. R. Hjelle, „Fast and accurate read-out of interferometric optical fiber sensors“, vol. 9754, SPIE, 2016, 97540E–97540E–7.
- [57]D. R. Hjelle, O. Aune, B. Falch, D. Østling, and R. Ellingsen, „Fiber-Optic Biosensor Technology for Rapid, Accurate and Specific Detection of Enzymes“, in *Advanced Photonics*, Optical Society of America, 2014, JTU6A.3.
- [58]S. Tierney, B. M. H. Falch, D. R. Hjelle, and B. T. Stokke, „Determination of Glucose Levels Using a Functionalized Hydrogel Optical Fiber Biosensor: Toward Continuous Monitoring of Blood Glucose in Vivo“, *Anal. Chem.*, vol. 81, no. 9, pp. 3630–3636, 2009.
- [59]K. Hammarling and D. R. Hjelle, „Single strand, fiber optic glucose and pH sensor“, in *paper 9715-31, SPIE Photonic West 2016, Optical Diagnostics and Sensing XVI: Toward Point-of-Care Diagnostics*, 2016.
- [60]J. J. Cras, C. A. Rowe-Taitt, D. A. Nivens, and F. S. Ligler, „Comparison of chemical cleaning methods of glass in preparation for silanization“, *Biosensors and Bioelectronics*, vol. 14, no. 8 - 9, pp. 683–688, 1999.
- [61]X. H. Qin, A. Ovsianikov, J. Stampfl, and R. Liska, *Additive manufacturing of photosensitive Hydrogels for tissue engineering applications*, 2014.
- [62]X. Wu and O. Solgaard, „Short-cavity multimode fiber-tip Fabry-Pérot sensors“, *Opt. Express*, vol. 21, no. 12, pp. 14 487–14 499, 2013.
- [63]V. V. R. Sai, T. Kundu, and S. Mukherji, „Novel U-bent fiber optic probe for localized surface plasmon resonance based biosensor“, *Biosensors and Bioelectronics*, vol. 24, no. 9, pp. 2804–2809, 2009.

- [64]T.-J. Lin and C.-T. Lou, „Reflection-based localized surface plasmon resonance fiber-optic probe for chemical and biochemical sensing at high-pressure conditions“, *The Journal of Supercritical Fluids*, vol. 41, no. 2, pp. 317–325, 2007.
- [65]R. Dutta, R. Bharadwaj, S. Mukherji, and T. Kundu, „Study of localized surface-plasmon-resonance-based optical fiber sensor“, *Appl. Opt.*, vol. 50, no. 25, E138–E144, 2011.
- [66]H Nguyen, F Sidirolou, S. F. Collins, *et al.*, „A localized surface plasmon resonance-based optical fiber sensor with sub-wavelength apertures“, *Applied Physics Letters*, vol. 103, no. 19, pp. –, 2013.
- [67]S. J. Park, C. L. Ta, H. G. Baek, *et al.*, „Optical fiber sensor for refractive index measurement based on localized surface plasmon resonance“, in *Lasers and Electro-Optics Pacific Rim (CLEO-PR), 2013 Conference on*, 2013, pp. 1–2.
- [68]C.-H. Chen, T.-C. Tsao, W.-Y. Li, *et al.*, „Novel U-shape gold nanoparticles-modified optical fiber for localized plasmon resonance chemical sensing“, *Microsystem Technologies*, vol. 16, no. 7, pp. 1207–1214, 2009.
- [69]B.-Y. Hsieh, Y.-F. Chang, M.-Y. Ng, *et al.*, „Localized Surface Plasmon Coupled Fluorescence Fiber-Optic Biosensor with Gold Nanoparticles“, *Anal. Chem.*, vol. 79, no. 9, pp. 3487–3493, 2007.
- [70]T.-J. Lin and M.-F. Chung, „Using Monoclonal Antibody to Determine Lead Ions with a Localized Surface Plasmon Resonance Fiber-optic Biosensor“, *Sensors*, vol. 8, no. 1, p. 582, 2008.
- [71]K. Kajikawa and K. Mitsui, „Optical fiber biosensor based on localized surface plasmon resonance in gold nanoparticles“, vol. 5593, 2004, pp. 494–501.
- [72]J. Cao, M. H. Tu, T. Sun, and K. T. V. Grattan, „Wavelength-based localized surface plasmon resonance optical fiber biosensor“, *Sensors and Actuators B: Chemical*, vol. 181, no. 0, pp. 611–619, 2013.
- [73]L.-K. Chau, Y.-F. Lin, S.-F. Cheng, and T.-J. Lin, „Fiber-optic chemical and biochemical probes based on localized surface plasmon resonance“, *Sensors and Actuators B: Chemical*, vol. 113, no. 1, pp. 100–105, 2006.
- [74]H.-H. Jeong, N. Erdene, J.-H. Park, *et al.*, „Real-time label-free immunoassay of interferon-gamma and prostate-specific antigen using a Fiber-Optic Localized Surface Plasmon Resonance sensor“, *Biosensors and Bioelectronics*, vol. 39, no. 1, pp. 346–351, 2013.
- [75]J. G. Ortega-Mendoza, A. Padilla-Vivanco, C. Toxqui-Quitl, *et al.*, „Optical Fiber Sensor Based on Localized Surface Plasmon Resonance Using Silver Nanoparticles Photodeposited on the Optical Fiber End“, *Sensors*, vol. 14, no. 10, pp. 18 701–18 710, 2014.
- [76]W. Ni, H. Chen, X. Kou, M. H. Yeung, and J. Wang, „Optical Fiber-Excited Surface Plasmon Resonance Spectroscopy of Single and Ensemble Gold Nanorods“, *J. Phys. Chem. C*, vol. 112, no. 22, pp. 8105–8109, 2008.
- [77]H. Nguyen, F. Sidirolou, S. F. Collins, *et al.*, „Periodic array of nanoholes on gold-coated optical fiber end-faces for surface plasmon resonance liquid refractive index sensing“, *Proc. SPIE*, vol. 8351, pp. 835 126–835 128, 2012.

- [78]W. E. Wentworth, „Dependence of the Beer-Lambert absorption law on monochromatic radiation: An experiment of spectrophotometry“, *Journal of Chemical Education*, vol. 43, no. 5, p. 262, 1966.
- [79]G. Mie, „Beiträge zur Optik trüber Medien, speziell kolloidaler Metallösungen“, *Ann. Physik*, vol. 330, no. 3, pp. 377–442, 1908.
- [80]C. F. Bohren and D. R. Huffman, *Absorption and Scattering of Light by Small Particles*. Wiley, 1998.
- [81]P. B. Johnson and R. W. Christy, „Optical Constants of the Noble Metals“, *Phys. Rev. B*, vol. 6, no. 12, pp. 4370–4379, 1972.
- [82]T. R. Jensen, M. L. Duval, K. L. Kelly, *et al.*, „Nanosphere Lithography: Effect of the External Dielectric Medium on the Surface Plasmon Resonance Spectrum of a Periodic Array of Silver Nanoparticles“, *J. Phys. Chem. B*, vol. 103, no. 45, pp. 9846–9853, 1999.
- [83]R. Gans, „The Form of Ultramicroscopic Gold Particles“, *Annalen der Physik*, vol. 37, pp. 881–900, 1912.
- [84]V. Klimov, *Nanoplasmonics*. Pan Stanford Publishing, 2014.
- [85]U. Kreibig and M. Volmerr, *Optical Properties of Metal Clusters*, 25. Springer Science & Business Media, 1995, vol. 25, p. 552. arXiv: arXiv:1011.1669v3.
- [86]M. Gluodenis and C. A. Foss, „The effect of mutual orientation on the spectra of metal nanoparticle rod-rod and rod-sphere pairs“, *Journal of Physical Chemistry B*, vol. 106, no. 37, pp. 9484–9489, 2002.
- [87]P. K. Jain, S. Eustis, and M. A. El-Sayed, „Plasmon Coupling in Nanorod Assemblies: Optical Absorption, Discrete Dipole Approximation Simulation, and Exciton-Coupling Model“, *The Journal of Physical Chemistry B*, vol. 110, no. 37, pp. 18 243–18 253, 2006.
- [88]B. T. Draine and P. J. Flatau, „Discrete-Dipole Approximation For Scattering Calculations“, *Journal of the Optical Society of America A*, vol. 11, no. 4, p. 1491, 1994.
- [89]C. Sönnichsen and B. Reinhard, „A molecular ruler based on plasmon coupling of single gold and silver nanoparticles“, *Nature . . .*, vol. 23, p. 741, 2005.
- [90]B. M. Reinhard, M. Siu, H. Agarwal, A. P. Alivisatos, and J. Liphardt, „Calibration of dynamic molecular rulers based on plasmon coupling between gold nanoparticles“, *Nano Letters*, vol. 5, no. 11, pp. 2246–2252, 2005.
- [91]B. M. Reinhard, S. Sheikholeslami, A. Mastroianni, A. P. Alivisatos, and J. Liphardt, „Use of plasmon coupling to reveal the dynamics of DNA bending and cleavage by single EcoRV restriction enzymes“, *Proceedings of the National Academy of Sciences*, vol. 104, no. 8, pp. 2667–2672, 2007.
- [92]P. K. Jain, W. Huang, and M. A. El-Sayed, „On the universal scaling behavior of the distance decay of plasmon coupling in metal nanoparticle pairs: A plasmon ruler equation“, *Nano Letters*, vol. 7, no. 7, pp. 2080–2088, 2007. arXiv: 1106.1690.
- [93]S. Fritz, A. Hilger, U. Kreibig, and V. M., „Width of cluster plasmon Resonances“, *Physical Review B*, vol. 48, no. 24, p. 18 178, 1993.

- [94]B. Foerster, A. Joplin, K. Kaefer, *et al.*, „Chemical Interface Damping Depends on Electrons Reaching the Surface“, *ACS Nano*, vol. 11, no. 3, pp. 2886–2893, 2017.
- [95]J. W. Ha, „Chemical interface damping of single gold nanorods with low sensitivity to the medium dielectric constant“, *Chemical Physics Letters*, vol. 676, pp. 65–69, 2017.
- [96]B. Mehrdel, A. A. Aziz, T. L. Yoon, and S. C. Lee, „Effect of chemical interface damping and aggregation size of bare gold nanoparticles in NaCl on the plasmon resonance damping“, *Optical Materials Express*, vol. 7, no. 3, p. 955, 2017.
- [97]P. Mulvaney, J. Pérez-Juste, M. Giersig, L. M. Liz-Marzán, and C. Pecharromán, „Drastic surface plasmon mode shifts in gold nanorods due to electron charging“, *Plasmonics*, vol. 1, no. 1, pp. 61–66, 2006.
- [98]S. K. Ghosh, S. Nath, S. Kundu, K. Esumi, and T. Pal, „Solvent and ligand effects on the localized surface plasmon resonance (LSPR) of gold colloids“, *Journal of Physical Chemistry B*, vol. 108, no. 37, pp. 13 963–13 971, 2004.
- [99]C. Radhakumary and K. Sreenivasan, „Gold nanoparticles generated through “green route” bind Hg²⁺ with a concomitant blue shift in plasmon absorption peak“, *The Analyst*, vol. 136, no. 14, p. 2959, 2011.
- [100]P. Mulvaney, „Surface Plasmon Spectroscopy of Nanosized Metal Particles“, *Langmuir*, vol. 12, no. 3, pp. 788–800, 1996. arXiv: 96/2412-0788{\\$}12.00/0 [0743-7463].
- [101]A. Henglein, P. Mulvaney, and T. Linnert, „Chemistry of silver aggregates in aqueous solution: non-metallic oligomers and metallic particles“, *Electrochimica Acta*, vol. 36, no. 11-12, pp. 1735–1741, 1991.
- [102]A. Henglein and D. Meisel, „Radiolytic Control of the Size of Colloidal Gold Nanoparticles“, *Langmuir*, vol. 14, no. 26, pp. 7392–7396, 1998.
- [103]M. I. Stockman, „Nanoplasmons : The physics behind the applications“, *Physics Today*, vol. 64, no. February, pp. 39–44, 2011.
- [104]E. Let, D. J. Bergman, and M. I. Stockman, „Surface Plasmon Amplification by Stimulated Emission of Radiation: Quantum Generation of Coherent Surface Plasmons in Nanosystems“, *Physics*, vol. 90, no. January, pp. 1–4, 2003.
- [105]M. I. Stockman, S. V. Faleev, and D. J. Bergman, „Localization versus delocalization of surface plasmons in nanosystems: Can one state have both characteristics?“, *Physical Review Letters*, vol. 87, no. 16, p. 167 401, 2001.
- [106]D. R. Hjelme, „A lower bound on the resolution limit of resonant refractive index sensors“, in *Advanced Photonics 2017 (IPR, NOMA, Sensors, Networks, SPPCom, PS)*, ser. OSA Technical Digest (online), New Orleans, Louisiana: Optical Society of America, 2017, pp. 1–3.
- [107]B. W. Silverman, „Some Aspects of the Spline Smoothing Approach to Non-Parametric Regression Curve Fitting“, *Journal of the Royal Statistical Society. Series B (Methodological)*, vol. 47, no. 1, pp. 1–52, 1985.
- [108]H. I. Muri and D. R. Hjelme, „LSPR coupling and distribution of interparticle distances between nanoparticles in hydrogel on optical fiber end face“, *Sensors (Switzerland)*, vol. 17, no. 12, p. 2723, 2017.

- [109]L. A. Austin, M. A. MacKey, E. C. Dreaden, and M. A. El-Sayed, „The optical, photothermal, and facile surface chemical properties of gold and silver nanoparticles in biodiagnostics, therapy, and drug delivery“, *Archives of Toxicology*, vol. 88, no. 7, pp. 1391–1417, 2014. arXiv: NIHMS150003.
- [110]H. H. I. Muri, A. Bano, and D. R. D. Hjelme, „LSPR and Interferometric Sensor Modalities Combined Using a Double-Clad Optical Fiber“, *Sensors*, vol. 18, no. 1, p. 187, 2018.
- [111]J. R. Epstein and D. R. Walt, „Fluorescence-based fibre optic arrays: a universal platform for sensing“, *Chem. Soc. Rev.*, vol. 32, no. 4, pp. 203–214, 2003.
- [112]K. L. Michael, L. C. Taylor, S. L. Schultz, and D. R. Walt, „Randomly Ordered Addressable High-Density Optical Sensor Arrays“, *Analytical Chemistry*, vol. 70, no. 7, pp. 1242–1248, 1998.
- [113]S Torquato, B Lu, and J Rubinstein, „Nearest-neighbor distribution functions in many-body systems“, *Phys. Rev. A*, vol. 41, no. 4, pp. 2059–2075, 1990.
- [114]B. Lu and S Torquato, „Nearest-surface distribution functions for polydispersed particle systems“, *Phys. Rev. A*, vol. 45, no. 8, pp. 5530–5544, 1992.
- [115]S Torquato and S. B. Lee, „Computer simulations of nearest-neighbor distribution functions and related quantities for hard-sphere systems“, *Physica A: Statistical Mechanics and its Applications*, vol. 167, no. 2, pp. 361–383, 1990.
- [116]S. A. Maier, M. L. Brongersma, P. G. Kik, and H. A. Atwater, „Observation of near-field coupling in metal nanoparticle chains using far-field polarization spectroscopy“, *Phys. Rev. B*, vol. 65, no. 19, pp. 193 408–, 2002.
- [117]V. A. Markel, „Introduction to the Maxwell Garnett approximation: tutorial“, *Journal of the Optical Society of America A*, vol. 33, no. 7, p. 1244, 2016.
- [118]G. Möbus and B. J. Inkson, „Nanoscale tomography in materials science“, *Materials Today*, vol. 10, no. 12, pp. 18–25, 2007.
- [119]K Kulawik, P. A. Buffat, A Kruk, A. M. Wusatowska-sarnek, and A Czyska-filemonowicz, „Materials Characterization Imaging and characterization of γ' and γ ” nanoparticles in Inconel 718 by EDX elemental mapping and FIB - SEM tomography“, *Materials Characterization*, vol. 100, pp. 74–80, 2015.
- [120]P. Schneider, M. Meier, R. Wepf, and R. Müller, „Serial FIB/SEM imaging for quantitative 3D assessment of the osteocyte lacuno-canalicular network“, *Bone*, vol. 49, no. 2, pp. 304–311, 2018.
- [121]E. Jurrus, M. Hardy, T. Tasdizen, *et al.*, „Axon tracking in serial block-face scanning electron microscopy“, *Medical Image Analysis*, vol. 13, no. 1, pp. 180–188, 2018.
- [122]W. Denk and H. Horstmann, „Serial Block-Face Scanning Electron Microscopy to Reconstruct Three-Dimensional Tissue Nanostructure“, *PLOS Biology*, vol. 2, no. 11, e329, 2004.
- [123]S. Guo, S. Dong, and E. Wang, „Rectangular silver nanorods: Controlled preparation, liquid-liquid interface assembly, and application in surface-enhanced raman scattering“, *Crystal Growth and Design*, vol. 9, no. 1, pp. 372–377, 2009.
- [124]S. G. Booth and R. A. Dryfe, „Assembly of Nanoscale Objects at the Liquid/Liquid Interface“, *Journal of Physical Chemistry C*, vol. 119, no. 41, pp. 23 295–23 309, 2015.

- [125]M. T. Postek, K. S. Howard, A. H. Johnson, and K. L. McMichael, „The scanning electron microscope“, *Handbook of charged particle optics*, pp. 363–399, 1997.
- [126]S.-Y. Lin, K.-S. Chen, and L. Run-Chu, „Drying methods affecting the particle sizes, phase transition, deswelling/reswelling processes and morphology of poly(N-isopropylacrylamide) microgel beads“, *Polymer*, vol. 40, no. 23, pp. 6307–6312, 1999.
- [127]R. Rüchel and M. D. Brager, „Scanning electron microscopic observations of polyacrylamide gels“, *Analytical Biochemistry*, vol. 68, no. 2, pp. 415–428, 1975.
- [128]X.-Z. Zhang, Y.-Y. Yang, T.-S. Chung, and K.-X. Ma, „Preparation and Characterization of Fast Response Macroporous Poly(N-isopropylacrylamide) Hydrogels“, *Langmuir*, vol. 17, no. 20, pp. 6094–6099, 2001.
- [129]J Zhang and N. A. Peppas, „Morphology of poly(methacrylic acid)/poly(N-isopropyl acrylamide) interpenetrating polymeric networks“, *Journal of Biomaterials Science, Polymer Edition*, vol. 13, no. 5, pp. 511–525, 2002.
- [130]F. M. Plieva, I. N. Savina, S. Deraz, *et al.*, „Characterization of supermacroporous monolithic polyacrylamide based matrices designed for chromatography of bioparticles“, *Journal of Chromatography B*, vol. 807, no. 1, pp. 129–137, 2004.
- [131]I. N. Savina, B. Mattiasson, and I. Y. Galaev, „Graft polymerization of acrylic acid onto macroporous polyacrylamide gel (cryogel) initiated by potassium doperiodatocuprate“, *Polymer*, vol. 46, no. 23, pp. 9596–9603, 2005.
- [132]H. H. Trieu and S Qutubuddin, „Polyvinyl alcohol hydrogels I. Microscopic structure by freeze-etching and critical point drying techniques“, *Colloid and Polymer Science*, vol. 272, no. 3, pp. 301–309, 1994.
- [133]J. Chen and K. Park, „Synthesis and characterization of superporous hydrogel composites“, *Journal of Controlled Release*, vol. 65, no. 1, pp. 73–82, 2000.
- [134]F. M. Plieva, M. Karlsson, M.-R. Aguilar, *et al.*, „Pore structure in supermacroporous polyacrylamide based cryogels“, *Soft Matter*, vol. 1, no. 4, pp. 303–309, 2005.
- [135]A GOLDSTEIN, Y SOROKA, M FRUŠIĆ-ZLOTKIN, I POPOV, and R KOHEN, „High resolution SEM imaging of gold nanoparticles in cells and tissues“, *Journal of Microscopy*, vol. 256, no. 3, pp. 237–247, 2014.
- [136]S. Bertazzo, E. Gentleman, K. L. Cloyd, *et al.*, „Nano-analytical electron microscopy reveals fundamental insights into human cardiovascular tissue calcification“, *Nature Materials*, vol. 12, p. 576, 2013.
- [137]H. I. D. Muri and D. R. Hjelme, „Mapping the Distribution of Particles in Hydrogel in Use for Nanoplasmonic Biosensors: A Comparison of Preparation Methods“, *MDPI Gels – In progress*, vol. X, no. X, p. 13, 2018.
- [138]A. Mehdizadeh Kashi, K. Tahemanesh, S. Chaichian, *et al.*, „How to Prepare Biological Samples and Live Tissues for Scanning Electron Microscopy (SEM)“, *Galen Medical Journal; Vol 3, No 2 (2014): June 2014*, 2014.
- [139]B. Little, P. Wagner, R. Ray, R. Pope, and R. Scheetz, „Biofilms: An ESEM evaluation of artifacts introduced during SEM preparation“, *Journal of Industrial Microbiology*, vol. 8, no. 4, pp. 213–221, 1991.

PAPER I

Article

LSPR Coupling and Distribution of Interparticle Distances between Nanoparticles in Hydrogel on Optical Fiber End Face

Harald Ian Muri *  and Dag Roar Hjelle

Department of Electronic Systems, Norwegian University of Science and Technology, Gunnerus gate 1, 7012 Trondheim, Norway; dag.hjelme@ntnu.no

* Correspondence: harald.muri@ntnu.no; Tel.: +47-7341-2688

Received: 30 September 2017; Accepted: 20 November 2017; Published: 25 November 2017

Abstract: We report on a new localized surface plasmon resonance (LSPR)-based optical fiber (OF) architecture with a potential in sensor applications. The LSPR-OF system is fabricated by immobilizing gold nanoparticles (GNPs) in a hydrogel droplet polymerized on the fiber end face. This design has several advantages over earlier designs. It dramatically increase the number nanoparticles (NP) available for sensing, it offers precise control over the NP density, and the NPs are positioned in a true 3D aqueous environment. The OF-hydrogel design is also compatible with low-cost manufacturing. The LSPR-OF platform can measure volumetric changes in a stimuli-responsive hydrogel or measure binding to receptors on the NP surface. It can also be used as a two-parameter sensor by utilizing both effects. We present results from proof-of-concept experiments exploring the properties of LSPR and interparticle distances of the GNP-hydrogel OF design by characterizing the distribution of distances between NPs in the hydrogel, the refractive index of the hydrogel and the LSPR attributes of peak position, amplitude and linewidth for hydrogel deswelling controlled with pH solutions.

Keywords: reflection-based FO systems; smart hydrogel; LSPR coupling; nanoplasmonics; point dipole model; Mie scattering; proof-of-concept; interparticle distance distribution; pH sensor

1. Introduction

Fiber optic (FO) sensors based on local surface plasmon resonance (LSPR) have been proposed in various configurations over the last decade [1–4]. The most important features of LSPR FO sensors are label-free sensing, fast response time, high sensitivity, high selectivity, simplified optical design and remote sensing capabilities. The label-free sensing can also be multi-parametric by spectrally resolving different LSPR observed for noble metal nanostructures (NMNS) of different sizes and shapes [5]. LSPR-based FO sensors usually utilize NMNS interacting with the evanescent field at the optical fiber (OF) core-cladding interface or with the light at the OF end face [2,4]. The use of the OF end face offers simpler manufacturing methods compared to utilizing the evanescent field since there is no need for cladding removal. The techniques available for immobilization of NMNS on an OF end face are limited to essentially a monolayer manufactured by photolithographic structuring of metal film, thermal nucleation of metal film or random immobilization of nanoparticles (NP).

This paper reports on the development and the characterization of a new LSPR-based OF architecture in reflection prepared by immobilizing gold nanoparticles (GNP) in a hemispherical hydrogel on the OF end face with potential to be used in sensor applications, as shown in Figure 1.

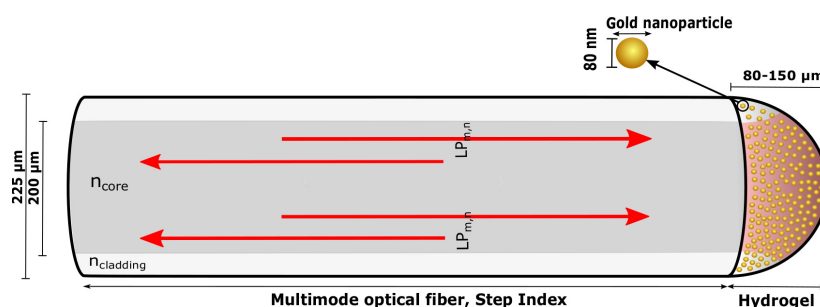


Figure 1. Illustration of the multimode (MM) OF with hydrogel containing gold nanoparticles (GNPs) immobilized on a fiber end face. Visible light is guided in the fiber core with the numerical aperture colored with red in the hydrogel.

The LSPR-based OF system is configured using a multimode (MM) OF with a semi-spherical hydrogel containing spherical GNPs immobilized on OF end face. This configuration ensures a strong LSPR signal as a result of the high numerical aperture (NA) exciting a large fraction of the GNPs and effective collection of scattering from the LSPR of the GNPs. The advantages over earlier designs lies in the increase of the number of GNPs available for sensing, the precise control over the GNP density, having free standing single GNPs distributed in a three-dimensional aqueous environment, and low cost manufacturing. The LSPR OF system can be utilized to detect volumetric changes in the hydrogel, receptor-analyte recombination on the GNP surface or chemical concentrations with surface-enhanced Raman scattering (SERS). By using NPs of different sizes, shapes or material compositions, they can also be used for multianalyte sensing in complex mixtures.

We present proof-of-concept experiments where we explore the LSPR and interparticle distance distribution attributes of the GNP-hydrogel OF design. The LSPR properties and interparticle distances of GNP-hydrogel are assessed for the increasing number density (ND) of GNPs, as well as for the increasing polymer density of the hydrogel. The polymer density is controlled by inducing swelling or deswelling with pH solutions. The ND is controlled by changing the initial ND of GNPs in the hydrogel, as well as by inducing swelling and deswelling of the hydrogel. Increasing ND reduces the distance between the neighboring GNPs that may induce electrostatic interaction between the particles, causing a shift in the LSPR. Increasing polymer density may also result in an LSPR shift due to increasing refractive index (RI). The nearest-neighbor distribution function (NNDF) is therefore computed for increasing ND of GNPs embedded in the hydrogel to assess the distribution of interparticle distances, whereas the RI as a function of hydrogel deswelling is investigated based on the estimation of the mole fraction of polymer and water. The LSPR peak position, amplitude and full width at half maximum (FWHM) of the reflectance from GNP-hydrogel are characterized for the hydrogel deswelling stimulated with pH solutions and for the increase in ND_0 . In addition, the sources of reflection are investigated with respect to the LSPR reflectance spectrum to determine possible errors included in the LSPR peak position value. Since the LSPR peak position is measured for the hydrogel swelling degree induced by different acidic solutions, the LSPR FO design is also represented as a pH sensor.

2. LSPR Attributes of GNPs Immobilized in a Hydrogel

2.1. Scattering of GNP-Hydrogel

The absorption and scattering of incident light on NMNS depends on the optical frequency, particle size and shape, the dielectric environment and the optical constants of the metal. The reflection from GNP embedded in hydrogel immobilized on OF end face is a result of both scattering and absorption. However, in our case with 80-nm GNPs, the reflection will be dominated by the

scattering. With sufficient low GNP density and the absence of dipole-dipole interactions, the scattering cross-section of GNPs embedded in hydrogel can be described by Mie theory for spherical particles [6],

$$\sigma_{\text{sca}} = \frac{P_{\text{sca}}}{I_{\text{inc}}} = \frac{2\pi}{|k|^2} \sum_{L=1}^{\infty} (2L+1)(|a_L|^2 + |b_L|^2) \quad (1)$$

where P_{sca} is the scattered power, I_{inc} is the incident plane wave intensity, L are integers representing a dipole for $L = 1$ or multipoles for $L > 1$ and k is the incoming wavevector. a_L and b_L are parameters composed of the Riccati–Bessel functions ψ_L and χ_L ,

$$a_L = \frac{m\psi_L(mx)\psi'_L(x) - \psi'_L(mx)\psi_L(x)}{m\psi_L(mx)\chi'_L(x) - \psi'_L(mx)\chi_L(x)} \quad (2a)$$

$$b_L = \frac{\psi_L(mx)\psi'_L(x) - m\psi'_L(mx)\psi_L(x)}{\psi_L(mx)\chi'_L(x) - m\psi'_L(mx)\chi_L(x)} \quad (2b)$$

where the primes represents the first differentiation with respect to the argument in the parenthesis, $x = k_m r$, r is the radius of the particle, k_m is the wavenumber of the incident light within a medium, $m = \frac{\tilde{n}}{n_m}$, n_m is the real refractive index of the surroundings of the metal and $\tilde{n} = n_R + in_I$ is the complex refractive index of the metal. For a dipole with $x \ll 1$, one can use an approximation of the Riccati–Bessel functions given by Bohren and Huffman to express the scattering cross-section as [7],

$$\sigma_{\text{sca}} = \frac{32\pi^4 \epsilon_m^2 V^2}{\lambda^4} \left[\frac{(\epsilon_1 - \epsilon_m)^2 + (\epsilon_2)^2}{(\epsilon_1 + 2\epsilon_m)^2 + (\epsilon_2)^2} \right] \quad (3)$$

where ϵ_1 and ϵ_2 are the real and imaginary components, respectively, of the complex metal dielectric function $\tilde{\epsilon}(\lambda) = \epsilon_1 + i\epsilon_2$, ϵ_m is the dielectric constant of the surrounding medium, V is the particle volume, and λ is the wavelength of the incident light. Maximum scattering in Equation (3) occurs when the condition of $\text{Re}[\tilde{\epsilon}(\lambda)] = -2\epsilon_m$ is met. If the dielectric medium around the GNP changes, the wavelength of the LSPR changes. The scattering of 80-nm GNPs can be computed by Equation (1) with $L = 1$ as shown in Figure 2 for different RI of the surrounding medium (n_m).

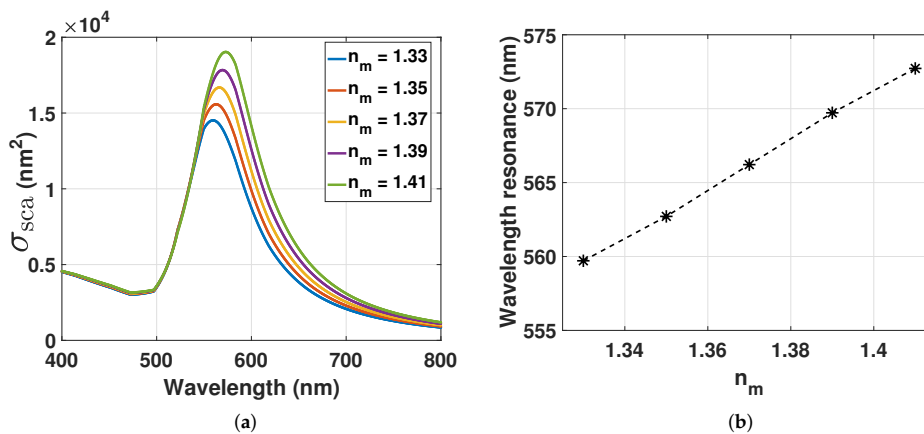


Figure 2. (a) Scattering cross-section computed from Equation (1) with $L = 1$ of GNP with 80 nm in diameter for increasing refractive index (RI) of the surrounding medium; (b) LSPR peak position from Figure 2a as a function of increasing RI.

Optical constants of bulk gold were taken from Johnson and Christy [8]. The redshift for increasing RI will also be associated with a spectral broadening and an increasing amplitude. By using the Drude model, the LSPR peak position as a function of $n_m = \sqrt{\epsilon_m}$ within a sufficiently narrow range can be described as,

$$\lambda_{\max} = \lambda_p \sqrt{2n_m^2 + 1} \quad (4)$$

where λ_p is the plasma oscillation wavelength of the bulk metal [9]. A deswelling hydrogel increases the polymer density, which also increases the probability of having polymer chains in close proximity to the GNPs. The polymer chains in close proximity to the plasmonic wave of the GNPs increase the local RI, which will redshift the LSPR.

2.2. Electrostatic Interactions between Dipoles of GNPs in Hydrogel

Considering a sufficiently high density of GNPs immobilized in the hydrogel, a dipole-dipole interaction between them will occur due to the short interparticle distances. For center-to-center interparticle distances d less than $5r$, the resonance condition $\text{Re}[\tilde{\epsilon}(\lambda)] = -2\epsilon_m$ found from Equation (3) should be corrected by including a dependence on the ND [10]. For two spheres of equal size in close proximity to each other with near-field coupling in the longitudinal mode, the dispersion equation can be described by the point dipole model [11,12],

$$1 - 4 \frac{\alpha_1 \alpha_2}{d^6} = 0 \quad (5)$$

where α_1 is the polarizability of the particle at point r_1 and α_2 is the polarizability of the particle at point r_2 . The polarizability of a spherical particle in a medium with dielectric constant ϵ_m is,

$$\alpha_i = r_i^3 \frac{\epsilon_i - \epsilon_m}{\epsilon_i + 2\epsilon_m} \quad (6)$$

where r_i and ϵ_i are the radius and the dielectric function of the nanosphere, respectively. Equation (6) can be substituted into Equation (5) for α_1 and α_2 to obtain the dispersion equation for two equal coupled spheres.

$$4 \left(\frac{r}{d}\right)^6 \left(\frac{\tilde{\epsilon}(\lambda) - \epsilon_m}{\tilde{\epsilon}(\lambda) + 2\epsilon_m}\right)^2 = 1 \quad (7)$$

By solving Equation (7) with respect to $\tilde{\epsilon}(\lambda)$, we find the dielectric function of the two-particle "cluster" at resonance for antisymmetric plasmon oscillations,

$$\tilde{\epsilon}(\lambda) = -2\epsilon_m \left(1 + 3\left(\frac{r}{d}\right)^3\right) \quad (8)$$

The resonance condition $\text{Re}[\tilde{\epsilon}(\lambda)] = -2\epsilon_m$ used for describing Equation (4) can then be corrected with Equation (8) to include the dipole-dipole interactions. With $n_{md} = \sqrt{\epsilon_m \epsilon_d} = n_{\text{gel}} \sqrt{1 + 3\left(\frac{r}{d}\right)^3}$, where $n_{\text{gel}} = \sqrt{\epsilon_m}$ is the RI of the hydrogel and $\epsilon_d = \left(1 + 3\left(\frac{r}{d}\right)^3\right)$, the scattering cross-section of GNP can be computed from Equation (1) with $L = 1$ for decreasing d as shown in Figure 3. A decrease in d redshifts the LSPR wavelength. With constant n_{gel} and increasing ND due to hydrogel contraction, the redshift is proportional to $\left(\frac{r}{d}\right)^3$. The redshift of the decreasing d will also be associated with a spectral broadening and an increasing amplitude.

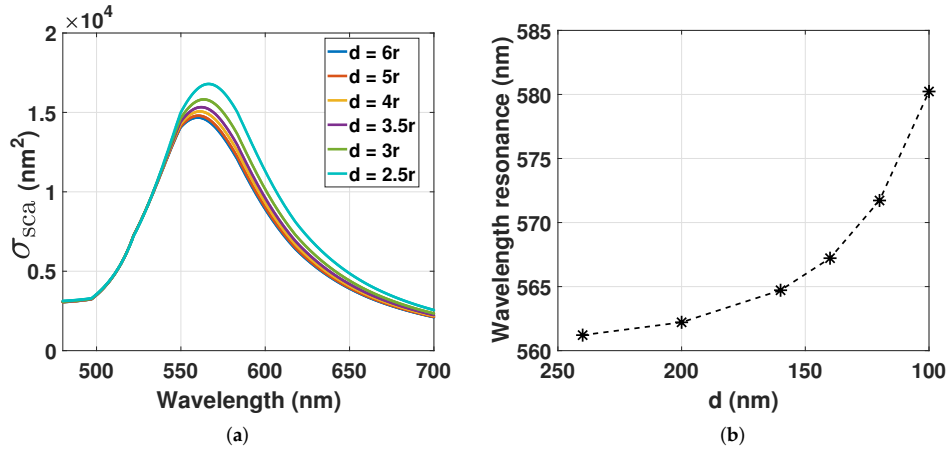


Figure 3. (a) Scattering cross-section computed from Equation (1) with $L = 1$ of GNP with 80 nm in diameter for the decrease in d ; (b) LSPR peak position from Figure (a) as a function of decreasing d . $n_m = 1.33$.

2.3. The Influence of the Nearest-Neighbor Distribution Function on the LSPR Signal

The linewidth and the amplitude of the LSPR signal from the GNP-hydrogel depends on the RI of the medium, the radiative and non-radiative damping of the oscillating electrons, as well as the polydispersity index (PDI) of the GNPs ($\text{PDI} = \frac{\text{Variance}}{\text{Average}^2}$ of the cumulant analysis of the dynamic light scattering of colloids [13]). For hydrogel deswelling, the interparticle distance decreases and increases the dipole-dipole interactions between the GNPs. The resonance condition can be expressed as Equation (8). The linewidth and the amplitude of the LSPR signal depend now also on the distribution of the distances between the particles. The probability density function related to interparticle distances can be accurately estimated by utilizing models based on the nearest-neighbor distribution function (NNDF). Work from Torquato, Lu and Rubinstein has derived theoretical expressions of ‘void’ NNDF of random distributed impenetrable spheres where the probability of finding the nearest neighbor is at a given distance $l = d - r$ from a point in the region exterior to the particles [14–16]. The void NNDF for randomly-distributed three-dimensional impenetrable spheres in the Carnahan–Starling approximation can be expressed as,

$$H_v(y) = 24\eta(1-\eta)(ey^2 + fy + g) \exp[-\eta(8ey^3 + 12fy^2 + 24gy + h)], y > \frac{1}{2} \quad (9)$$

where $y = \frac{l}{2r}$, $\eta = \frac{\varphi\pi(2r)^3}{6}$ is the reduced density, φ is the ND and $e = e(\eta)$, $f = f(\eta)$, $g = g(\eta)$, $h = h(\eta)$ are the density-dependent coefficients.

$$e(\eta) = \frac{1 + \eta}{(1 - \eta)^3} \quad (10a)$$

$$f(\eta) = -\frac{\eta(3 + \eta)}{2(1 - \eta)^3} \quad (10b)$$

$$g(\eta) = \frac{\eta^2}{2(1 - \eta)^3} \quad (10c)$$

$$h(\eta) = \frac{-9\eta^2 + 7\eta - 2}{2(1 - \eta)^3} \quad (10d)$$

For our experiments, the GNPs have a diameter of 80 nm with ND at $\approx 10^{11}$ particles/mL. Thus, the reduced density for GNPs embedded in the hydrogel becomes $\eta = 2.6 \times 10^{-5}$. Since $\eta \ll 1$ for the GNP densities used in our experiments, Equation (9) can be simplified to,

$$H_v(y) = 24\eta y^2 \exp[-8\eta y^3], y > \frac{1}{2} \quad (11)$$

Considering that there is significant dipole-dipole interactions between GNPs for $d \leq 5r$, the probability of finding particles within this range can be computed by integrating $H_v(y)$ from $y_1 = \frac{2r-r}{2r} = \frac{1}{2}$ to $y_2 = \frac{5r-r}{2r} = 2$,

$$P(d \leq 5r) = \int_{y_1}^{y_2} 24\eta y^2 \exp[-8\eta y^3] dy = -\exp[-8\eta y_2^3] + \exp[-8\eta y_1^3] \quad (12)$$

For the increase of ND in Equation (11), the probability of finding the nearest-neighbor at a given distance $l = d - r$ is increasing while the width of the distribution function $H_v(y)$ is decreasing. The change in ND for hydrogel swelling or contraction will then change the probability value $H_v(\frac{\bar{d}-r}{2r})$ at mean interparticle distance (\bar{d}) and influence the amplitude and the linewidth of the LSPR signal for $\bar{d} \leq 5r$.

2.4. Assessing the Refractive Index for Hydrogel Swelling Degree

We can express the RI of the hydrogel as,

$$n_{\text{gel}} = n_p x_p + n_w (1 - x_p) \quad (13)$$

where n_p is the RI of the polymer, n_w is the RI of the water and x_p is the mole fraction of the polymer. As the hydrogel is composed of two components, polymer and water, the relation between mole fraction x and mass fraction w can be found from:

$$w_w m_p = w_p m_w \quad (14a)$$

$$x_p \frac{m_w}{M_w} = x_w \frac{m_p}{M_p} \quad (14b)$$

where w_p is the mass fraction of the polymer, w_w is the mass fraction of water, m_p is the mass of the polymer, m_w is the mass of water, M_p is the molar mass of the polymer and M_w is the molar mass of water. m_p will be constant for hydrogel swelling and deswelling, while m_w will change. By using the relations in Equation (14a,b) the ratio $\frac{m_w}{m_p}$ can be expressed with respect to the mole fraction of the polymer as,

$$\frac{m_w}{m_p} = \left(\frac{1}{x_p}\right) \left(\frac{M_w}{M_p + M_w \frac{w_p}{w_w}}\right) = \frac{1}{x_p} a \quad (15)$$

x_p can be further described as a function of the hydrogel swelling degree by scaling it to the ratio $\frac{V_{\text{pregel}}}{V}$ where V_{pregel} is the volume of pregel on the OF and V is the volume of the hydrogel on the OF.

The ratio $\frac{m_w}{m_p}$ as a function of $\frac{V_{\text{pregel}}}{V} = v$ by the use of Equation (14a) becomes,

$$\frac{m_w}{m_p} = \left(\frac{1}{v}\right) \left(\frac{\frac{w_{w0}}{w_{p0}} \rho_p + \rho_w}{\rho_p + \frac{w_p}{w_w} \rho_w}\right) = \frac{1}{v} b \quad (16)$$

where ρ_p is the density of the polymer (pure) and ρ_w is the density of water (pure). By setting Equation (15) equal to (16), x_p is scaled to v with a and b ,

$$x_p = v \frac{a}{b} \quad (17)$$

The ratio $\frac{a}{b}$ is only weakly dependent on the swelling degree. We can therefore approximate $\frac{a}{b}$ as a constant found with the initial value of x_{p0} and v_0 . By inserting Equation (17) into Equation (13), the RI can be assessed for the hydrogel for swelling and contraction.

3. Materials and Methods

3.1. Materials

The gels were prepared by using the following chemicals: acrylamide (AAM) (99%, Sigma Aldrich, Schnellendorf, Germany), acrylic acid (AAC) (99%, Sigma Aldrich), *N,N*-methylenebisacrylamide (BIS) ($\geq 99.5\%$, Sigma Aldrich), 1-hydroxycyclohexyl phenyl ketone (99%, Sigma Aldrich), dimethyl sulfoxide (DMSO) ($\geq 99.9\%$, Sigma Aldrich), octamethylcyclotetrasiloxane (98%, Sigma Aldrich), 3-(trimethoxysilyl) propyl methacrylate (Silane A174) (98%, Sigma Aldrich), citrate-stabilized spheroidal GNPs of 80 nm in diameter (7.8×10^9 particles/mL, absorption max: 551–557 nm, PDI ≤ 0.2 , Sigma Aldrich), phosphate-buffered saline (PBS) (Tablet, Sigma Aldrich) and squalane (99%, Sigma Aldrich). Milli-Q (mQ) water (resistivity 18.2 M/cm, Millipore Simplicity 185) was used for all solutions. Hydrochloric acid (HCl) (1.0 M, Sigma Aldrich) and sodium chloride (NaCl) (18% *w/v*, VWR, Oslo, Norway) were added to mQ-water to prepare solutions for controlling the hydrogel swelling and contraction. The GNP solution was densified to an ND of 1.95×10^{11} particles/mL by water evaporation. AAM, AAC and BIS were dissolved in PBS solution (pH 7.4) to prepare a stock solution with 30 wt% AAM-AAC with a molar ratio of 15/85 AAM/AAC and with 2 mol% BIS. A pregel solution of 10 wt% AAM-AAC and 2 mol% BIS was prepared by adding citrate-stabilized GNP or PBS to the AAM-AAC stock solution of 30 wt%.

3.2. Synthesize Hydrogel on OF End Face

The LSPR OF segment in Figure 1 was based on $\varnothing 200 \mu\text{m}$ MM OF (FT200EMT, Thorlabs, Göteborg, Sweden) that were stripped of the jacket and cleaned with 96% ethanol, cut (Cleaver MS-7310, Melbye Skandinavia, Oslo, Norway) and prepared for silanization [17]. For silanization of the OF end face, the tips of the OF were soaked in a solution of 0.01M HCl for 15 min to activate the surface, cleaned with mQ-water and then immersed in a solution of 3-(trimethoxysilyl) propyl methacrylate (0.084 M, nitrogen purged octamethylcyclotetrasiloxane) for 10 min. The OF was then cleaned with 96% ethanol and stored for up to two weeks. The pregel solutions from Section 3.1 were used further for the synthesis of hydrogel on the silanized OF end face. Then, 0.01 M 1-hydroxycyclohexyl phenyl ketone photoinitiator (PI) in DMSO was added to the pregel solution to a volume ratio of 31/2000 PI/pregel, so a final pregel solution was made. A drop of squalane added with PI (2.7 mg/mL) was deposited on a glass rod. The silanized OF was located in the squalane-PI drop, and an aliquot of the final pregel solution was transferred to its end face by a pipette (Finnpipette F2, Thermo Scientific, Oslo, Norway). Next, the gel-OF was aligned with an ultraviolet (UV) $\varnothing 365 \mu\text{m}$ Core MM OF (FG365UEC, Thorlabs, Göteborg, Sweden) by the use of an optical stage under observation in an optical stereo-microscope (SZX7, Olympus, Oslo, Norway). The UV-OF illuminated the gel-OF with light at 365 nm by the use of a fiber-coupled LED (M365F1, Thorlabs, Göteborg, Sweden), and it was cured for 10 min. The polymerized gel-OF was subsequently immersed in pentane to remove impurities for 5 s and transferred to PBS solution until further use.

3.3. Setup of the Fiber Optic Instrument

The FO setup illustrated in Figure 4 consists of the following components: visible (VIS) broadband source (HL-2000-FHSA-LL, 360–2400 nm, Ocean Optics, Oslo, Norway), 50:50 coupler MM (50/50, FCMH2-FC, 400–1600 nm, Thorlabs, Göteborg, Sweden), VIS spectrometer (QE65Pro, Ocean Optics,

Oslo, Norway), loose OF-ends terminated with index matching gel (G608N3, Thorlabs, Göteborg, Sweden), LSPR OF segment Ø200µm MM OF (FT200EMT, Thorlabs, Göteborg, Sweden).

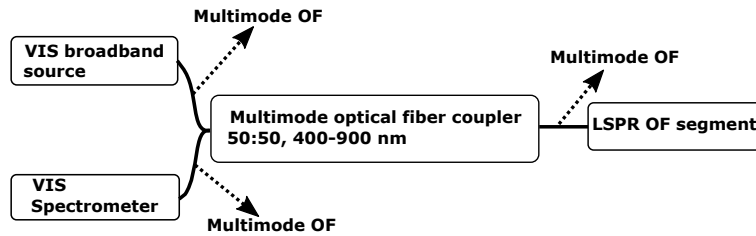


Figure 4. Configuration of the reflection-based FO system containing the light source, spectrometer, OF coupler and LSPR OF segment.

The data acquisition was obtained with the program Spectrasuite (Ocean Optics, Oslo, Norway), and the OFs were spliced using a Fitel Fusion Splicer (Furukawa Electric, Tokyo, Japan).

3.4. Reflectance Measurements of GNP Embedded in Hydrogel

The reflectance spectra were estimated from the measured raw spectra S_λ normalized to a measured reference spectrum R_λ . Before normalization, we subtracted the measured dark spectrum D_λ (recorded with the light source turned off) from both the raw spectra and reference spectra. The normalized reflectance spectra were then computed as:

$$I_R = \left(\frac{S_\lambda - D_\lambda}{R_\lambda - D_\lambda} \right) \times 100\% \quad (18)$$

The reference spectrum was recorded from the reflections of the bare Ø200µm MM OF in mQ-water solution. To determine the LSPR peak position, the reflectance spectra were fitted with a centered and scaled smoothing spline function with the smoothing parameter at 0.999. With smoothing parameter $p = 0$, the smoothing spline function produces a least-square line fit to the data, whereas with $p = 1$, the smoothing spline function produces a cubic spline interpolant. By choosing a fixed smoothing parameter, the balance between residual error and local variation is also fixed [18].

Scattering increases with increasing GNP size, with an associated spectral broadening of the LSPR signal. Thus, for our FO system with GNP diameter ≥ 80 nm and density $\geq 2 \times 10^{10}$ particles/mL in mQ-water solution, we observed a high LSPR signal. The hydrogels used in our swelling measurements were polymerized from pregels with 80-nm GNP densities at $ND_{01} = 8.86 \times 10^9$ particles/mL, $ND_{02} = 1.73 \times 10^{10}$ particles/mL and $ND_{03} = 1.7 \times 10^{11}$ particles/mL.

The hydrogel contraction and swelling were controlled by immersing the gel-OF in pH solutions between 5 and 3 with a constant ionic strength (IS) at 0.274 M. The reflectance spectra were recorded after contraction or swelling had reached equilibrium. The gel-OF was washed in PBS after each measurement to control the size of hydrogel for deswelling only. pH and IS were controlled with a pH/IS meter (inoLab pH/ION 7320, WTW, Oslo, Norway), electrode selective towards Cl (Cl 800 (BNC), WTW, Oslo, Norway), pH electrode (pH phenomenal MIC 220, VWR Collection, Oslo, Norway) and temperature measurer (pH phenomenal TEMP21, VWR Collection, Oslo, Norway). All the experiments were carried out at room temperature, and the pH and IS of the solutions were controlled by adding HCl and NaCl to mQ-water.

4. Results

First, the NNDF was estimated for increasing GNP densities in hydrogel to assess the distribution of interparticle distances for the hydrogel swelling degree. The RI as a function of hydrogel deswelling was estimated based on the estimation of the mole fraction of polymer and water. Second, the sources of

reflections in the hydrogel were investigated with respect to the LSPR reflectance spectrum to determine possible errors included in the value of the LSPR peak with corresponding wavelength. Third, the LSPR response was demonstrated by measuring its peak positions as a function of GNP-hydrogel contraction controlled with pH solutions and as a function of increasing ND_0 . Last, the linewidth and the amplitude of the LSPR signal were characterized for hydrogel deswelling stimulated with pH solutions to compare the LSPR reflectance spectrum with the estimated NNDF of GNPs in hydrogel.

4.1. Nearest-Neighbor Distribution Function for Increasing GNP Density in the Hydrogel

Figure 5 shows the measured volume of pregel to the volume of hydrogel ($\frac{V_{\text{pregel}}}{V}$) ratio based on the observations obtained from optical microscope imaging.

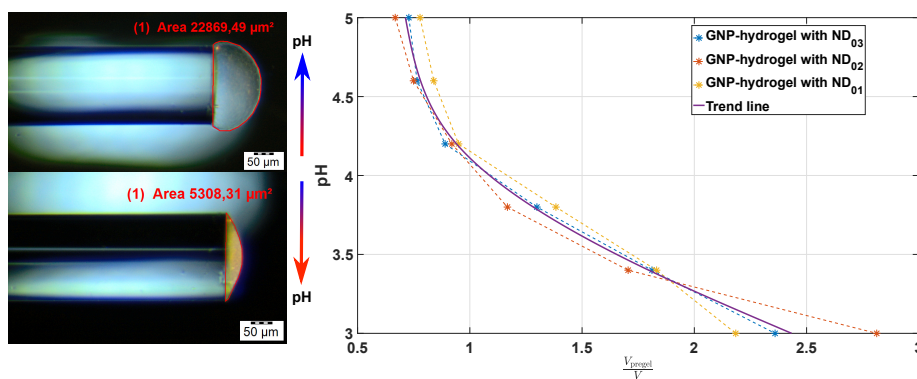


Figure 5. Estimate of the hydrogel volume for the decrease in pH from 5 to 3 based on observations in an optical microscope. The uncertainties of the volume measurements are estimated to be within 1 and 5%. ND, number density.

Three different pregels with different GNP densities at $ND_{01} = 8.86 \times 10^9$, $ND_{02} = 1.73 \times 10^{10}$ and $ND_{03} = 1.7 \times 10^{11}$ particles/mL were used to manufacture the OF sensors. The ratio $\frac{V_{\text{pregel}}}{V}$ was estimated for hydrogel contraction controlled with pH solutions from 5 to 3. $\frac{V_{\text{pregel}}}{V}$ as a function of decreasing pH follows the same trend for the OF sensors fabricated from different densities of GNP in pregel. The NDs of GNPs found for the deswelling hydrogels are further used to compute the NNDF.

In Figure 6a, the NNDFs (Equation (11)) are computed for pH 5 and 3 (from the NDs in Figure 5) of the OF sensors manufactured from different GNP-pregel densities. The probability at the mean interparticle distance \bar{d} is increasing for increasing ND and hydrogel contraction. The smallest \bar{d} for the largest ND and lowest pH is greater than $5r$, i.e., greater than the range where the interaction between dipoles of GNPs occurs.

The probability (Equation (12)) of finding particles with interparticle distance between $2r \leq d \leq 5r$ (computed from NDs in Figure 5) is represented in Figure 6b. The probability is increasing from 0.1×10^{-3} to 6.7×10^{-3} for increasing ND and hydrogel contraction. The low probability for $2r \leq d \leq 5r$ shows that there is only a small fraction of GNPs with interparticle distances inducing dipole-dipole interactions. Hence, for a truly random distribution of GNPs in hydrogel at pH 5 and 3, it is the increasing density of the polymer network and not the dipole-dipole interactions that should be the dominating factor for the change in the LSPR peak position. If the change in LSPR peak position is independent of ND in our experiments, the assumption of having particles randomly distributed in the hydrogel would be reasonable. On the contrary, if the LSPR peak position is dependent on the ND, the GNPs may be inhomogeneously distributed in the hydrogel with a large fraction of particles with $d \leq 5r$.

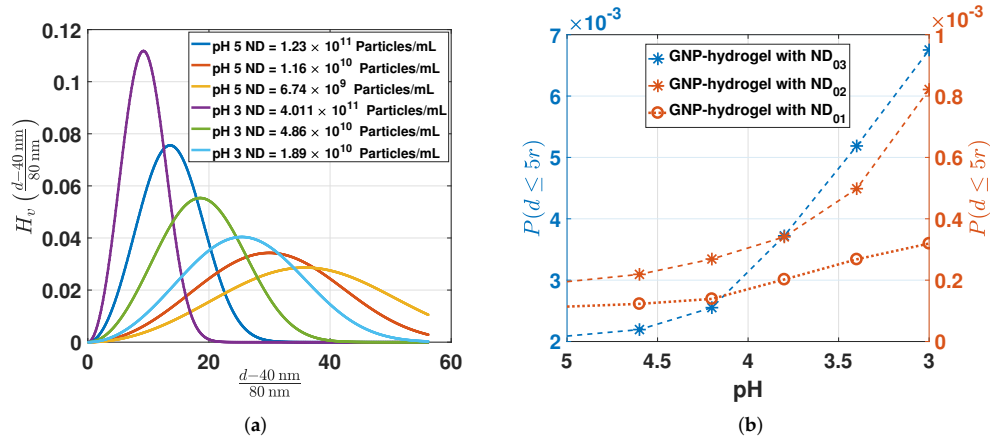


Figure 6. (a) Computation of the void nearest-neighbor distribution function (NPDF) (Equation (11)) for the NDs estimated in Figure 5 for pH 5 and 3; (b) computed probability (Equation (12)) for the interparticle distances between $2r \leq d \leq 5r$ from the ND estimated in Figure 5.

4.2. Refractive Index as a Function of Hydrogel Swelling Degree

The RI of the hydrogel can be assessed from Equation (13) by computing the mole fraction of the polymer in Equation (17). The RI of the polymer can be assumed to be dominated by the mole and mass fraction of AAM-AAC. For our experiments, the mass fraction of AAM-AAC is $w_{p0} = 0.1$. With $n_p = 1.513$ and $n_w = 1.333$ [19,20], n_{gel} from Equation (13) and (17) can be computed as a function of $\frac{V_{pregel}}{V}$ (from Figure 5) for pH 5 to 3 as presented in Figure 7a.

Deswelling of the hydrogel for pH 5 to 3 increases n_{gel} from ~ 1.333 to ~ 1.346 . Inserting $n_m = n_{gel}$ at 1.333 and 1.346 into Equation (1) with $L = 1$, the scattering of GNP can be computed as shown in Figure 7b.

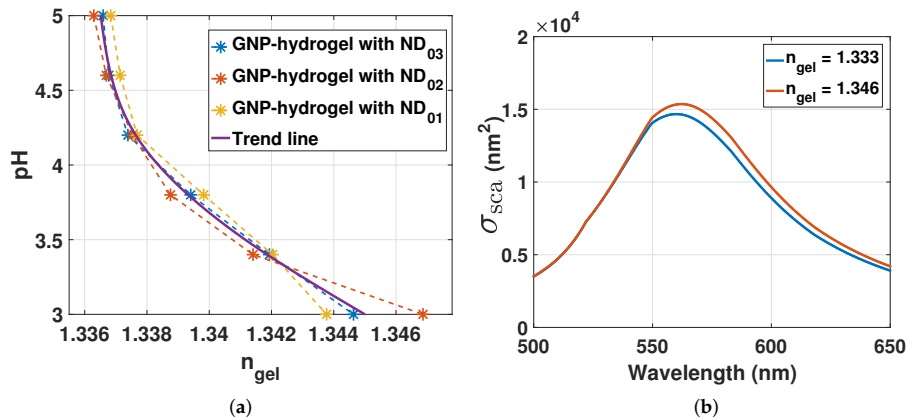


Figure 7. (a) RI of hydrogel computed from Equation (13) and (17) for pH 5 to 3; (b) scattering cross-section computed from Equation (1) with $L = 1$ for $n_m = n_{gel}$ at 1.333 and 1.346.

The scattering of GNPs redshifts by 2 to 3 nm with hydrogel contraction stimulated with pH from 5 to 3. Its important to note that the LSPR is dependent on the mole fraction of polymer chains that are

in close proximity to the plasmonic wave of the GNPs. Due to the localized sensing of the RI changes on the surface of the GNPs, n_m in Equation (1) and n_{gel} in Equation (13) would rather represent the local RI and the bulk RI of the hydrogel, respectively. Hence, the LSPR response of GNPs could be different for bulk and local RI changes.

4.3. The Reflectance for Different GNP Densities

Figure 8a–c shows reflectance spectra for 6.74×10^9 particles/mL (pH 5), 1.6×10^{10} particles/mL (pH 5) and for 1.36×10^{11} particles/mL (pH 4.4), respectively (NDs found from Figure 5). The reflectance measurements of hydrogel without GNPs are shown in Figure 8d for pH 5 to 3.

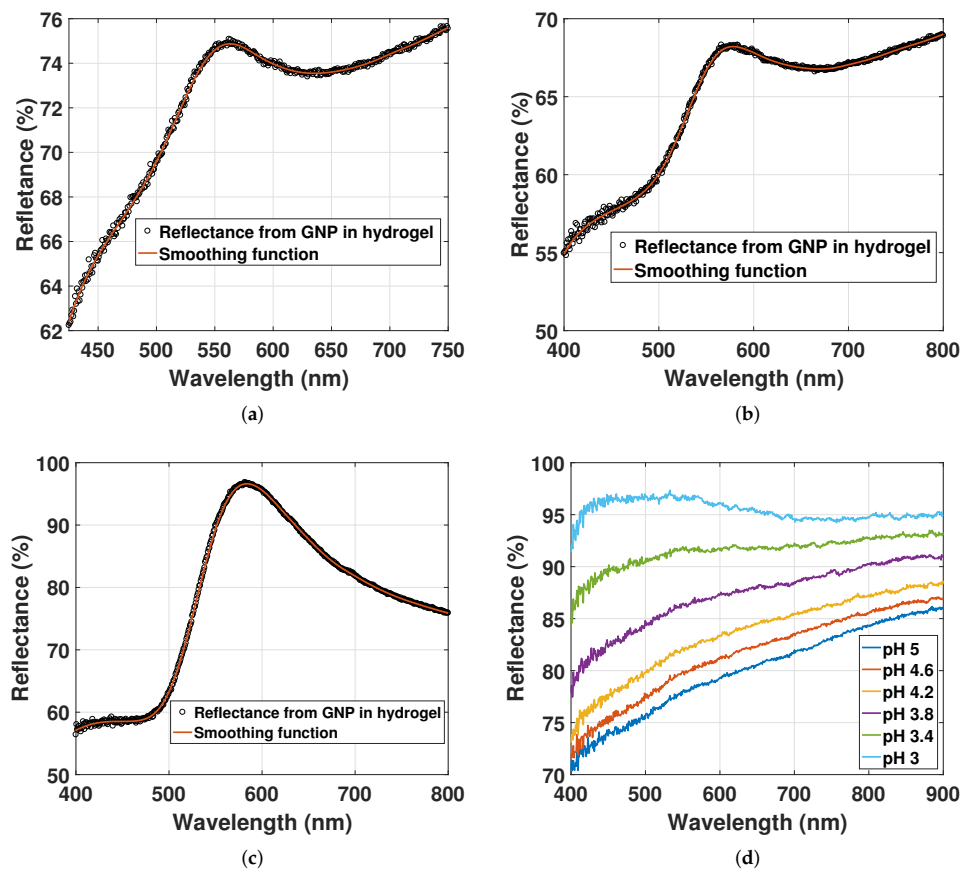


Figure 8. (a) Reflectance of GNP immobilized in hydrogel with ND of 6.74×10^9 particles/mL and (b) 1.6×10^{10} particles/mL in solution of pH at 5; (c) reflectance of GNP immobilized in hydrogel with ND of 1.36×10^{11} particles/mL in solution of pH at 4.4; (d) reflectance from hydrogel without GNPs for pH 5 to 3.

The LSPR peaks are at 561 nm, 575 nm and 583 nm for 6.74×10^9 particles/mL, 1.6×10^{10} particles/mL and 1.36×10^{11} particles/mL, respectively. The increasing ND of GNPs is redshifting the LSPR signal, while its linewidth is broadening. That the LSPR peak position is dependent on the ND indicates an electrostatic interaction between the dipoles. This contrasts with

the computed NNDF in Section 4.1, where only a minor fraction of GNPs was estimated to have interparticle distances less than $5r$. The particles in the hydrogel may not exhibit a random distribution, but could rather exhibit an inhomogeneous distribution with a large fraction of GNPs with interparticle distances between $2r \leq d \leq 5r$.

The spectra in Figure 8a–c may contain reflections other than scattering from GNP that could result in errors in the LSPR peak position value. Not only light scattering, but also light extinction of GNP occurs due to the reflection at the hydrogel-solution interface. The extinction of GNPs will add a spectrum of opposite sign to the LSPR signal relative to the scattered spectrum of GNP. The sources of scattering and extinction of GNP and hydrogel can be listed as illustrated in Figure 9.

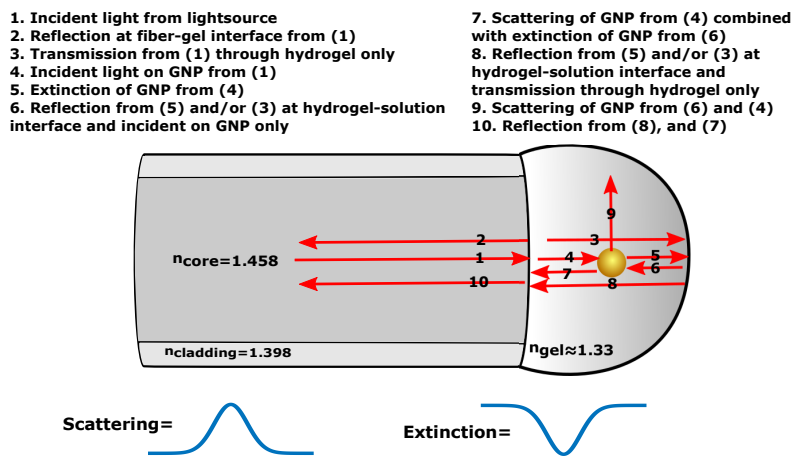


Figure 9. Sources of scattering and extinction from hydrogel and GNP.

The reflection at a normal incidence (2) can be assumed to be roughly 0.002 at the fiber-gel interface. The reflection (8, 6) at the hydrogel-solution interface has in previous work been determined based on visibility measurements [21]. With reflection at 0.002 for the fiber-gel interface and with visibility at 0.2, the reflection (8, 6) at the hydrogel-solution interface can be estimated to be 0.0002. Multiple reflections between the hydrogel-solution and fiber-gel interface can then be safely neglected. Hence, at the LSPR wavelength, the scattering combined with extinction of GNP (7) is dominated by the scattering from (4) as its intensity is much higher than the reflection from (6).

The reflectance measurements of hydrogel without GNP in Figure 8d have a decreasing slope and an increasing reflectance from pH 5 to 3. The change in the slope from the reflectance of the hydrogel will also change the observed LSPR peak position from the reflectance of the GNPs. The reflectance of GNP-hydrogel can be modeled with two functions, the reflectance of the hydrogel without GNPs and the LSPR signal from the GNPs, here modeled as a Gaussian function $g(\lambda - \lambda_0)$. Thus, we can write,

$$f_1(\lambda) = g(\lambda - \lambda_0) + v_0 f_2(\lambda) \quad (19a)$$

$$f_2(\lambda) = a_2(\lambda - \lambda_0)^2 + a_1(\lambda - \lambda_0) + a_0 \quad (19b)$$

where $f_1(\lambda)$ represents the reflection of both GNP and hydrogel with v_0 as a scaling factor for the reflection from the hydrogel without GNPs, $f_2(\lambda)$.

Assuming that $a_2 \ll a_1$, the LSPR peak position as a function of $f_1(\lambda)$ can be described by setting $\frac{\partial f_1(\lambda)}{\partial \lambda} = 0$,

$$\lambda_{\max} = \frac{v_0 a_1 \sigma^2}{b} + \mu \quad (20)$$

where $\sigma = \frac{\text{FWHM}}{2\sqrt{\ln 2}}$, μ and $g(\mu) = b$ are the peak position and amplitude, respectively, of the LSPR signal represented as $g(\lambda - \lambda_0)$. The derivative of λ_{max} with respect to a_1 determines the shift of λ_{max} with changing slope a_1 ,

$$\Delta\lambda_{\text{max}} = \frac{v_0\sigma^2}{b} \Delta a_1 \quad (21)$$

For the reflectance of hydrogel without GNPs in Figure 8d, Δa_1 can be estimated to be $-0.008 \frac{\%}{\text{nm}}$ with $a_2 \ll a_1$ for the change in pH from 5 to 3.8. The factor $\frac{v_0\sigma^2}{b} = \bar{m}$ from the LSPR signal will also determine the shift $\Delta\lambda_{\text{max}}$. For the GNP-hydrogel with low ND in Figure 8a,b, \bar{m} will be large. Thus, an increase in the slope will lead to a redshift of the LSPR signal, whereas a decrease in slope will lead to a blueshift. For the GNP-hydrogel with high ND in Figure 8c, \bar{m} will be small. The increase or decrease in slope will in this case lead to negligible red or blueshifts of the LSPR signal.

4.4. LSPR Peak Position as a Function of Hydrogel Swelling Degree

The reflectance spectra of GNP-hydrogel with ND_{01} at 8.86×10^9 particles/mL fitted with a smoothing spline function are shown in Figure 10a for pH solutions from 5 to 3.4. The resulting LSPR peak positions as a function of hydrogel contraction stimulated with pH solutions are presented in Figure 10b.

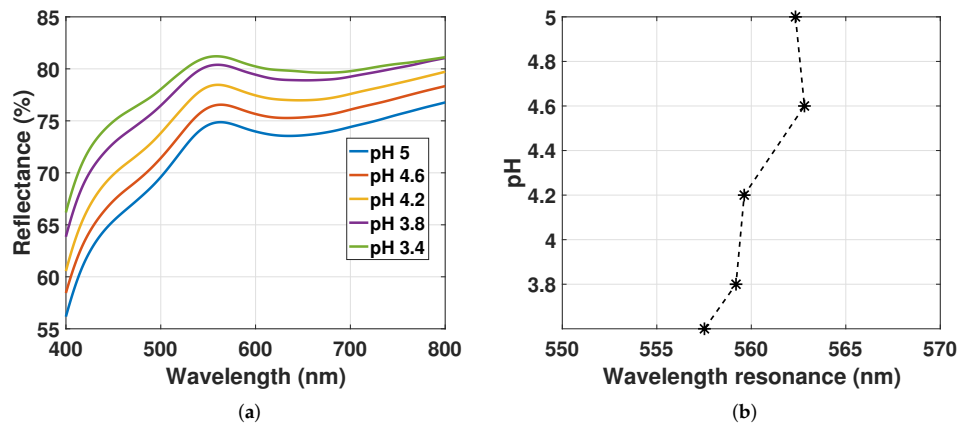


Figure 10. (a) Reflectance spectra of GNP-hydrogel with ND_{01} at 8.86×10^9 particles/mL fitted with a smoothing spline function for pH 5 to 3.4; (b) LSPR peak position from Figure 10a as a function of hydrogel deswelling stimulated with pH solutions from 5 to 3.4.

The reflectance peak is increasing for decreasing pH. As discussed in Section 4.3 for the OF sensor with ND_{01} , the reflectance spectrum will be a sum of the scattering from GNPs with an added slope from the light extinction of the hydrogel. The increase in reflectance peak in Figure 10a may be due to the increase in the reflectance of the hydrogel contraction as observed from Figure 8d. The LSPR peak positions in Figure 10b are changing from 562 nm to 557 nm as a function of hydrogel deswelling. For decreasing pH, the slope from the reflectance of the hydrogel is declining as discussed in Section 4.3. From pH 5 to 3.8, the linear function $f_2(\lambda)$ in Figure 10a has a change in slope of $\Delta a_1 = -0.01 \frac{\%}{\text{nm}}$ between 450 nm and 750 nm that is comparable to $\Delta a_1 = -0.008 \frac{\%}{\text{nm}}$ for the reflectance of hydrogel without GNPs in Figure 8d. $\Delta\lambda_{\text{max}}$ from Equation (21) can be estimated to be ~ 2.25 nm based on the reflectance of GNP-hydrogel in Figure 10a (setting $\Delta a_1 = -0.01 \frac{\%}{\text{nm}}$, $\text{FWHM} = 61$ nm, $g(\lambda - \lambda_0) = 3\%$ and $v_0 = 1$). As discussed in Section 4.2, an increasing mole fraction of polymer in close proximity to the plasmonic wave of the GNPs could also redshift the LSPR signal by 2 to 3 nm. Hence, the blueshift

of the LSPR peak in Figure 10b is due to the reduced slope from the reflectance of hydrogel for pH 5 to 3.4, as well as a result of the local variations of the RI in the hydrogel for the increasing mole fraction of polymer. With ND_{01} at 8.86×10^9 particles/mL, there is then little contribution from the dipole-dipole interactions on the LSPR signal.

Figure 11 represents the reflectance spectra of GNP-hydrogel with increased ND to ND_{02} at 1.73×10^{10} particles/mL fitted with a smoothing spline function for hydrogel deswelling and the corresponding LSPR peak positions.

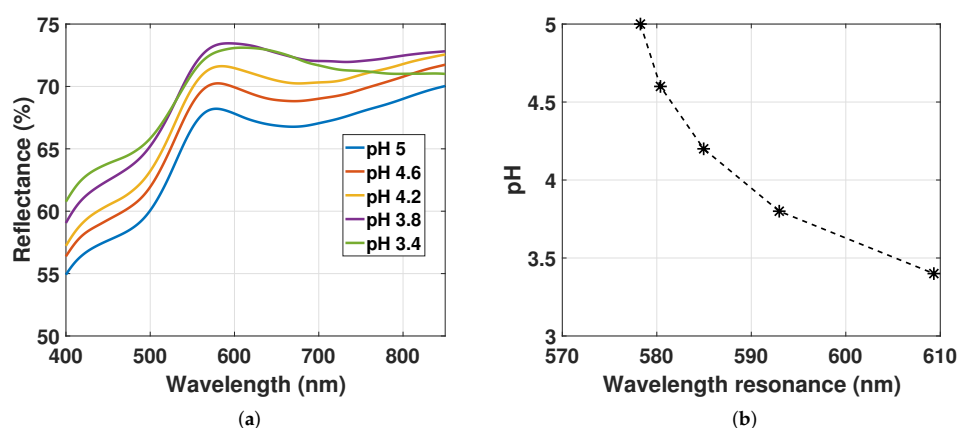


Figure 11. (a) Reflectance spectra of GNP-hydrogel with ND_{02} at 1.73×10^{10} particles/mL fitted with a smoothing spline function for pH 5 to 3.4; (b) LSPR peak position from Figure 11a as a function of hydrogel deswelling stimulated with pH solutions from 5 to 3.4.

The reflectance peak is increasing for pH 5 to 3.8. The increase may be a result of the increase in reflectance of the hydrogel for declining pH as discussed in Section 4.3. For pH 3.8 to 3.4, the ND of GNPs in the hydrogel increases from 2.02×10^{10} particles/mL to 2.95×10^{10} particles/mL (estimated from data in Figure 5), whereas the amplitude is declining and the linewidth is broadening (linewidth and amplitude estimated in Section 4.5). The decline in the reflectance peak from pH 3.8 to 3.4 is due to the decrease in the amplitude of the LSPR signal that is smaller than the increase in the reflectance of the hydrogel observed in Figure 8d. A decreasing amplitude for higher ND suggests also the hypothesis that there is a larger dispersion in particle scattering, which may be caused by the increased fraction of particles interacting, as well as the increased variation in local RI. The linewidth broadening is likely due to the increasing RI and the decrease in \bar{d} inducing dipole-dipole interactions.

The LSPR peak positions in Figure 11a as a function of hydrogel contraction controlled with pH solutions are presented in Figure 11b. The LSPR peak position is redshifting from 578 nm to 610 nm from pH 5 to 3.4. The change in the LSPR peak position in Figure 11b for decreasing pH is now due to three factors: (1) the RI change as a function of hydrogel contraction presented in Section 4.2 results in a redshift of 2 to 3 nm; (2) the change in the slope of $\Delta a_1 = -0.015 \frac{\%}{\text{nm}}$ from pH 5 to 3.8 in Figure 11a that results in a blueshift of 2 to 2.5 nm (see discussion from Figure 10); (3) the decrease in \bar{d} inducing electrostatic interactions between of the GNPs results in redshift of the LSPR signal. The change in LSPR peaks in Figures 10 and 11 shows a different response to the hydrogel deswelling due to the different amounts of GNPs immobilized in the hydrogel. By changing the density of GNPs in pregel from ND_{01} to ND_{02} , the LSPR response for hydrogel contraction becomes dependent on the decreasing \bar{d} as a result of the increasing fraction of GNPs with $\bar{d} \leq 5r$. Whereas the results in Figure 10 show a small blueshift of the LSPR due to the change in the slope Δa_1 with little influence from the

dipole-dipole interactions, the results in Figure 11 show a large redshifting of the LSPR due to the large influence of dipole-dipole interactions and with little influence from the slope Δa_1 .

Finally, the LSPR peak position was measured as a function of hydrogel deswelling stimulated with decreasing pH with even higher ND_{03} at 1.7×10^{11} particles/mL in Figure 12.

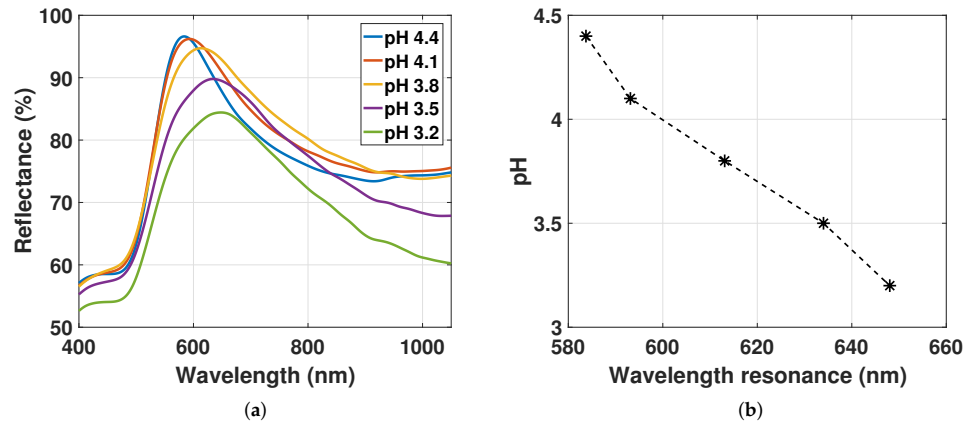


Figure 12. (a) Reflectance spectra of GNP-hydrogel with ND_{03} at 1.7×10^{11} particles/mL fitted with a smoothing spline function for pH 4.4 to 3.2; (b) LSPR peak position from Figure 12a as a function of hydrogel deswelling stimulated with pH solutions from 4.4 to 3.2.

The reflectance spectra of GNP-hydrogel for pH 4.4 to 3.2 fitted with a smoothing spline function are shown in Figure 12a, while the LSPR peak positions as a function of decreasing pH are presented in Figure 12b. The reflectance peak is decreasing, while the linewidth of the reflectance is broadening for hydrogel contraction. From pH 4.4 to 3.2, the ND increases from 1.4×10^{11} particles/mL to 3.5×10^{11} particles/mL (estimated from Figure 5). It is evident that the change in the amplitude of the LSPR signal from scattering of GNPs in Figure 12a dominates over the change in reflectance of the hydrogel observed in Figure 8d for the decrease in pH (linewidth and amplitude estimated in Section 4.5).

The decrease in amplitude of the LSPR signal from pH 4.4 to 3.2 may be a result of the increasing ND of GNPs from 1.4×10^{11} particles/mL to 3.5×10^{11} particles/mL (from data in Figure 5) that increases the dispersion in particle scattering caused by the increased fraction of particle interaction and the increased change in the variations of the local RI. The linewidth broadening is likely due to the increase in RI and the decrease in \bar{d} inducing dipole-dipole interactions.

In Figure 12a, the LSPR peak position is redshifting from 584 nm to 648 nm for hydrogel deswelling. The change of the shift is 64 nm, which is much larger than the shift of 2 to 3 nm from the change in RI for hydrogel contraction discussed in Section 4.2. $\Delta\lambda_{\max}$ from Equation (21) can be estimated to be ~ 2.65 nm (with $\Delta a_1 = -0.01 \frac{\%}{\text{nm}}$, with $g(\lambda - \lambda_0) = 38\%$ and FWHM = 237 nm). With $\Delta\lambda_{\max} \approx 2.65$ nm and minor RI changes for hydrogel contraction, the redshift of LSPR peak position observed in Figure 12b is most likely dominated by the reduced \bar{d} inducing dipole-dipole interactions between the GNPs.

4.5. Amplitude and Linewidth of the LSPR Signal as a Function of Hydrogel Swelling Degree

The amplitude and the linewidth of the LSPR signal from the reflectance spectra of GNP-hydrogel with ND_{03} at 1.7×10^{11} particles/mL for decreasing pH were determined based on the procedure illustrated in Figure 13.

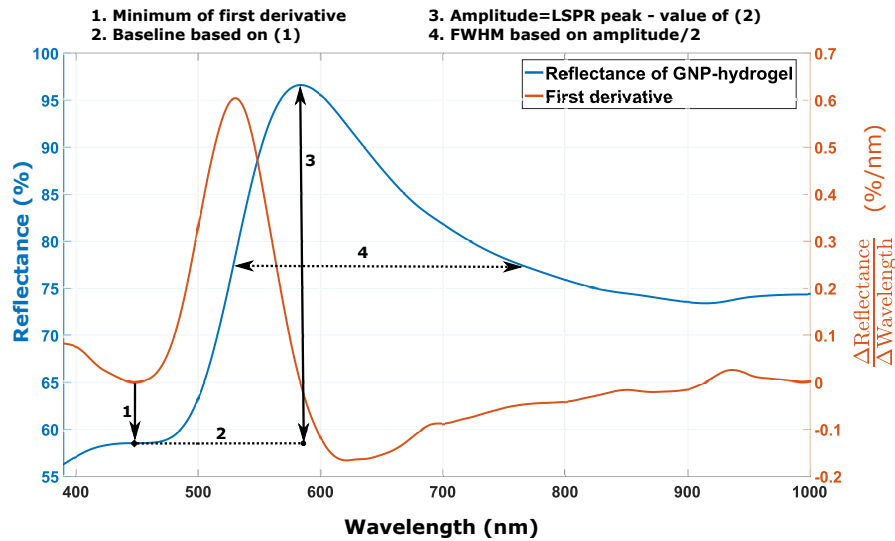


Figure 13. Smoothing fitted function of the reflectance of GNP-hydrogel with ND_{03} at 1.7×10^{11} particles/mL at pH 4.4 with the corresponding first derivative. The minimum of the first derivative of the reflectance of GNP-hydrogel determines the baseline used for computing the FWHM.

The first inflection point of the LSPR signal is used as the baseline for determining the amplitude and the linewidth of the reflectance of GNP-hydrogel. The LSPR reflectance peak subtracted from the baseline represents the amplitude. The linewidth of the LSPR signal is defined as the FWHM from the half maximum value. Due to the asymmetry of the signal, the procedure will tend to overestimate the linewidth. To account for this, the FWHM was further characterized by varying the baseline with respect to the inflection point. The baseline increasing by 10% and 20% proportionally to the inflection point from Figure 13 reduces both the FWHM and the amplitude, but will represent a value less dependent on the change in the asymmetry of the LSPR signal. Figure 14 shows the resulting amplitude and FWHM from the reflectance spectra of GNP-hydrogel from Figure 12 as a function of hydrogel contraction. In Figure 14a, the amplitude of the LSPR signal is decreasing monotonically for pH 4.4 to 3.2, independent of the baseline. The LSPR peak position response in Figure 12 was concluded to be dominated by the reduced \bar{d} , inducing dipole-dipole interactions between the GNPs with minor influence from the local variations of the RI change in the hydrogel and the change in the slope Δa_1 from the light extinction of hydrogel for decreasing pH. The declining amplitude in Figure 14a would imply as discussed in Section 4.4 a larger dispersion in particle scattering for higher ND. A larger dispersion in particle scattering may be caused by the increased fraction of interacting particles and the variations in the local RI.

The FWHM in Figure 14b is increasing from pH 4.4 to 3.5. From pH 3.5 to 3.2, the FWHM decreases for the 10% and the 20% increase in the baseline, while for the original baseline, it decreases from pH 3.8 to 3.2. The increase in FWHM is likely a result of the increasing RI and the dipole-dipole interaction between the GNPs. The decrease in FWHM from pH 3.8 to 3.2 might be due to the change in the reflection of the fiber-gel interface observed in Figure 8d, which changes the signature of the LSPR signal.

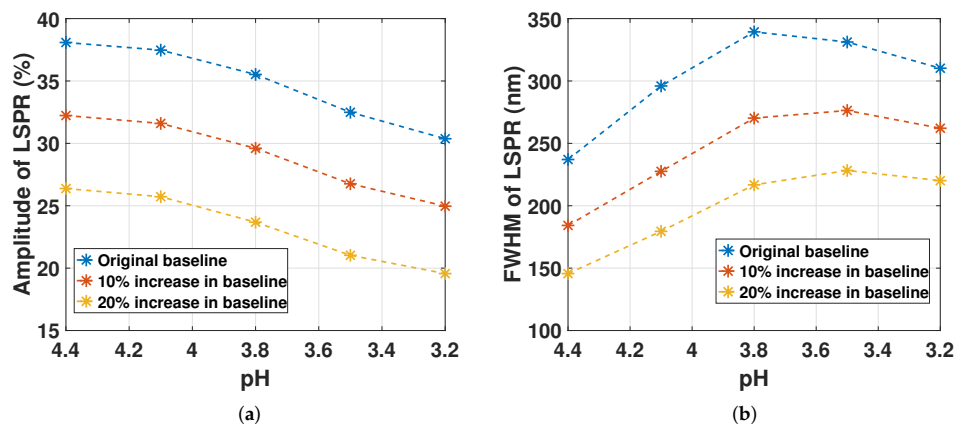


Figure 14. (a) Amplitude from the reflectance of GNP-hydrogel with ND_{03} at 1.7×10^{11} particles/mL for decreasing pH with an increasing baseline; (b) FWHM from the reflectance of GNP-hydrogel with ND_{03} at 1.7×10^{11} particles/mL for decreasing pH with an increasing baseline.

5. Conclusions

A new LSPR-based FO system was developed by immobilizing GNPs in a polymerized polyacrylamid-co-acrylic acid network as a hemispherical hydrogel on OF end face. Proof-of-concept experiments have been presented where we explore the LSPR and interparticle distance distribution attributes of the GNP-hydrogel. The results from the NNDF computation showed that the mean interparticle distance \bar{d} with the GNP densities used in our experiments is much larger than $5r$, whereas the results from the reflectance spectra of GNP-hydrogel on OF end face showed that LSPR peak position is dependent on \bar{d} . This contradiction suggests that the particles in the hydrogel may not exhibit a random distribution, but could rather exhibit an inhomogeneous distribution with a large fraction of GNPs with interparticle distances between $2r \leq d \leq 5r$. The amplitude of the LSPR signal decreases with hydrogel contraction, suggesting the hypothesis that higher ND results in larger dispersion in particle scattering caused by the increased fraction of particles interacting and the increased variations in local RI. The FWHM were increasing from pH 4.4 to 3.5 and decreasing from pH 3.5 to 3.2. The increase in FWHM is likely a result of the increasing RI and the dipole-dipole interactions. The decrease in FWHM from pH 3.8 to 3.2 might be due to the change in the reflection of the fiber-gel interface that changes the signature of the LSPR signal.

Further work will consist of developing the LSPR FO system towards biosensor applications where specific biochemicals will be detected by the use of stimuli-responsive materials embedded with noble metal or silicon nanoparticles (NMDNP). The potential for multi-parametric and label free sensing in complex biological mixtures by the use of an LSPR-based FO biosensor will also be investigated with the focus on the utilization of NMDNP of different sizes, shapes and material compositions. The different NMDNP embedded in tailored polymer networks will then have spectrally-resolvable LSPR peaks where each peak is associated with the detection of a specific biologic entity. By controlling the polarization of the incident light on NMDNP, the sensitivity of LSPR-based FO sensors can be improved by utilizing the dynamic peak position of LSPR for variable light polarizations as the sensing parameter.

Acknowledgments: This work was supported by strategic research funding from Norwegian University of Science and Technology (NTNU). The work was also supported in part by the Interreg Sweden-Norway program (IR2015.01) and Energy and Sensor Systems (ENERSENSE, strategic research program at NTNU).

Author Contributions: Harald Ian Muri and Dag Roar Hjelme conceived and designed the experiments; Harald Ian Muri performed the experiments; Harald Ian Muri and Dag Roar Hjelme analyzed the data; Harald Ian Muri and Dag Roar Hjelme wrote the paper.

Conflicts of Interest: The authors declare no conflict of interest.

References

1. Jeong, H.H.; Son, Y.J.; Kang, S.K.; Kim, H.J.; Roh, H.J.; Erdene, N.; Park, J.H.; Jeong, D.H.; Lee, H.Y.; Lee, S.K. Fiber-Optic Refractive Index Sensor Based on the Cone-Based Round Structure. *IEEE Sens. J.* **2013**, *13*, 351–358.
2. Sanders, M.; Lin, Y.; Wei, J.; Bono, T.; Lindquist, R.G. An enhanced LSPR fiber-optic nanoprobe for ultrasensitive detection of protein biomarkers. *Biosens. Bioelectron.* **2014**, *61*, 95–101.
3. Cao, J.; Tu, M.H.; Sun, T.; Grattan, K.T. Wavelength-based localized surface plasmon resonance optical fiber biosensor. *Sens. Actuators B Chem.* **2013**, *181*, 611–619.
4. Srivastava, S.K.; Arora, V.; Sapra, S.; Gupta, B.D. Localized Surface Plasmon Resonance-Based Fiber Optic U-Shaped Biosensor for the Detection of Blood Glucose. *Plasmonics* **2011**, *7*, 261–268.
5. Mayer, K.M.; Hafner, J.H. Localized Surface Plasmon Resonance Sensors. *Chem. Rev.* **2011**, *111*, 3828–3857.
6. Mie, G. Beiträge zur Optik trüber Medien, speziell kolloidaler Metallösungen. *Ann. Phys.* **1908**, *330*, 377–442.
7. Bohren, C.F.; Huffman, D.R. *Absorption and Scattering of Light by Small Particles*; Wiley: New York, NY, USA, 1998.
8. Johnson, P.B.; Christy, R.W. Optical Constants of the Noble Metals. *Phys. Rev. B* **1972**, *6*, 4370–4379.
9. Jensen, T.R.; Duval, M.L.; Kelly, K.L.; Lazarides, A.A.; Schatz, G.C.; Van Duyne, R.P. Nanosphere Lithography: Effect of the External Dielectric Medium on the Surface Plasmon Resonance Spectrum of a Periodic Array of Silver Nanoparticles. *J. Phys. Chem. B* **1999**, *103*, 9846–9853.
10. Maier, S.A.; Brongersma, M.L.; Kik, P.G.; Atwater, H.A. Observation of near-field coupling in metal nanoparticle chains using far-field polarization spectroscopy. *Phys. Rev. B* **2002**, *65*, 193408, doi:10.1103/PhysRevB.65.193408.
11. Klimov, V.V.; Guzatov, D.V. Optical properties of an atom in the presence of a two-nanosphere cluster. *Quantum Electron.* **2007**, *37*, 209, doi:10.1070/QE2007v037n03ABEH013322.
12. Jain, P.K.; El-Sayed, M.A. Plasmonic coupling in noble metal nanostructures. *Chem. Phys. Lett.* **2010**, *487*, 153–164.
13. Stetefeld, J.; McKenna, S.A.; Patel, T.R. Dynamic light scattering: A practical guide and applications in biomedical sciences. *Biophys. Rev.* **2016**, *8*, 409–427.
14. Torquato, S.; Lee, S.B. Computer simulations of nearest-neighbor distribution functions and related quantities for hard-sphere systems. *Phys. A Stat. Mech. Appl.* **1990**, *167*, 361–383.
15. Lu, B.; Torquato, S. Nearest-surface distribution functions for polydispersed particle systems. *Phys. Rev. A* **1992**, *45*, 5530–5544.
16. Torquato, S.; Lu, B.; Rubinstein, J. Nearest-neighbor distribution functions in many-body systems. *Phys. Rev. A* **1990**, *41*, 2059–2075.
17. Cras, J.; Rowe-Taitt, C.; Nivens, D.; Ligler, F. Comparison of chemical cleaning methods of glass in preparation for silanization. *Biosens. Bioelectron.* **1999**, *14*, 683–688.
18. Silverman, B.W. Some Aspects of the Spline Smoothing Approach to Non-Parametric Regression Curve Fitting. *J. R. Stat. Soc. Ser. B Methodol.* **1985**, *47*, 1–52.
19. Stejskal, J.; Horská, J. Refractive index increments of polyacrylamide and comments on the light scattering from its solutions. *Makromol. Chem. Phys.* **1982**, *183*, 2527–2535.

20. Haynes, W.M. *Handbook of Chemistry and Physics*, 97th ed.; CRC Taylor and Francis Group: Boca Raton, FL, USA, 2016.
21. Muri, H.I.D.I.; Bano, A.; Hjelme, D.R. First step towards an interferometric and localized surface plasmon fiber optic sensor. In Proceedings of the 25th International Conference on Optical Fiber Sensors (OFS-25), Chemical, Environmental, Biological and Medical Sensors and Biophotonics, Jeju, Korea, 24–28 April 2017; Paper Number: OFS100-046.



© 2017 by the authors. Licensee MDPI, Basel, Switzerland. This article is an open access article distributed under the terms and conditions of the Creative Commons Attribution (CC BY) license (<http://creativecommons.org/licenses/by/4.0/>).


PAPER II

This paper is not included due to copyright
available in
Journal of Lightwave Technology 2018 ;Volum 36.(4) s. 1159-1167
<https://doi.org/10.1109/JLT.2018.2791722>

PAPER III

Article

LSPR and Interferometric Sensor Modalities Combined Using a Double-Clad Optical Fiber

Harald Ian Muri * , Andon Bano and Dag Roar Hjelme

Department of Electronic Systems, Norwegian University of Science and Technology, Gunnerus Gate 1, 7012 Trondheim, Norway; andon2105@hotmail.com (A.B.); dag.hjelme@ntnu.no (D.R.H.)

* Correspondence: harald.muri@ntnu.no; Tel.: +47-7341-2688

Received: 23 November 2017; Accepted: 7 January 2018; Published: 11 January 2018

Abstract: We report on characterization of an optical fiber-based multi-parameter sensor concept combining localized surface plasmon resonance (LSPR) signal and interferometric sensing using a double-clad optical fiber. The sensor consists of a micro-Fabry-Perot in the form of a hemispherical stimuli-responsive hydrogel with immobilized gold nanorods on the facet of a cleaved double-clad optical fiber. The swelling degree of the hydrogel is measured interferometrically using the single-mode inner core, while the LSPR signal is measured using the multi-mode inner cladding. The quality of the interferometric signal is comparable to previous work on hydrogel micro-Fabry-Perot sensors despite having gold nanorods immobilized in the hydrogel. We characterize the effect of hydrogel swelling and variation of bulk solution refractive index on the LSPR peak wavelength. The results show that pH-induced hydrogel swelling causes only weak redshifts of the longitudinal LSPR mode, while increased bulk refractive index using glycerol and sucrose causes large blueshifts. The redshifts are likely due to reduced plasmon coupling of the side-by-side configuration as the interparticle distance increases with increasing swelling. The blueshifts with increasing bulk refractive index are likely due to alteration of the surface electronic structure of the gold nanorods donated by the anionic polymer network and glycerol or sucrose solutions. The recombination of biotin-streptavidin on gold nanorods in hydrogel showed a 7.6 nm redshift of the longitudinal LSPR. The LSPR response of biotin-streptavidin recombination is due to the change in local refractive index (RI), which is possible to discriminate from the LSPR response due to changes in bulk RI. In spite of the large LSPR shifts due to bulk refractive index, we show, using biotin-functionalized gold nanorods binding to streptavidin, that LSPR signal from gold nanorods embedded in the anionic hydrogel can be used for label-free biosensing. These results demonstrate the utility of immobilizing gold nanorods in a hydrogel on a double-clad optical fiber-end facet to obtain multi-parameter sensing.

Keywords: reflection-based OF sensor; smart hydrogel; FP interferometer; LSPR; gold nanorods; double-clad optical fiber; multiparameter sensor; single-point sensor

1. Introduction

Sensor miniaturization is an important design objective for biochemical sensors. Size matters, not only for applications requiring insertion into small sample volumes or insertion into tissue or vessels, but also for the functionality of the sensors [1]. Small size means fast diffusion times and therefore fast sensor response. Optical fiber-based sensors represent one popular sensor platform for miniaturization [2–4].

Multi-parameter sensing ability is another attractive sensor feature. Many applications require simultaneous measurement of several parameters in a single sample or single position. While this can be achieved using multiple sensor elements, the increased size of the resulting sensor might

not be acceptable. Therefore, sensors with multi-parameter sensing ability are receiving increasing attention in the literature [5]. For optical fiber (OF) sensing, one can utilize multiple modes to achieve multi-parameter sensing, for example, in tilted fiber Bragg grating sensors [6,7]. Other techniques include using fluorophores with different fluorescent wavelengths [8,9], or using noble metal nanoparticles with different localized surface plasmon resonance (LSPR) wavelengths [10] in an optrode or on the facet of a cleaved OF. All these sensors achieve multi-parameter sensing utilizing a single sensing modality.

We have recently demonstrated an OF-based multi-parameter sensor concept by combining LSPR and interferometric sensing using a double-clad optical fiber (DCOF) [11,12]. The multi-parameter sensor, as illustrated in Figure 1, consists of a micro-Fabry–Perot (FP) in the form of a hemispherical stimuli-responsive hydrogel [13,14] with immobilized gold nanoparticles (GNPs) on the facet of a cleaved DCOF [15,16].

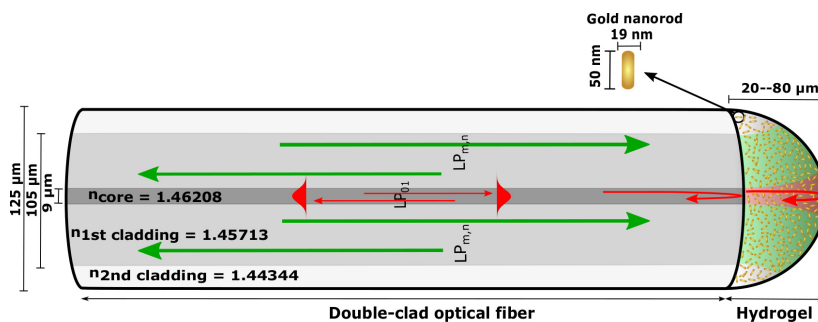


Figure 1. Illustration of the double-clad optical fiber combining interferometric and plasmonic sensor modalities with $n_{\text{core}} = 1.46208$, $n_{\text{1st cladding}} = 1.45713$, and $n_{\text{2nd cladding}} = 1.44344$. Light in the range of 1500–1600 nm (λ_{I}) is confined as single transverse mode both in the fiber and in the hydrogel volume, with reflection at the OF–hydrogel interface and hydrogel–solution interface illustrated with red color. Multi-mode with light in the range of 450–850 nm (λ_{II}) is guided in the first cladding with numerical aperture illustrated with green on fiber-end face. The FP interference is measured with λ_{I} , while the LSPR signal from gold nanorods (GNR) is measured with λ_{II} .

The swelling degree of the stimuli-sensitive hydrogel is measured interferometrically using the single-mode inner core of the DCOF in the 1500–1600 nm spectral range (noted as λ_{I} from now on), while the LSPR signal in the 450–850 nm spectral range (noted as λ_{II} from now on) is measured using the multi-mode (MM) inner cladding of the DCOF. This configuration enables efficient excitation and collection of the LSPR signal using the large numerical aperture (NA) MM waveguide defined by the inner cladding, at the same time as we suppress optical interference in the LSPR spectrum. Similarly, by using the single-mode core of the DCOF we avoid the limitation of modal dispersion in the MM fiber and the fiber-tip FP cavity, and achieve high visibility interference spectra for the interferometric measurement.

In the proof-of-concept experiments reported in [11,12], we demonstrated basic sensor functionality; the visibility of the FP signal was unaffected by the GNP densities up to $1.8 \times 10^{11} \text{ mL}^{-1}$ and particle diameter up to 100 nm. Furthermore, we showed that the LSPR peak wavelength was unaffected by the hydrogel swelling degree. A more detailed study of the LSPR signal from spherical GNPs embedded in anionic hydrogel [15,16] indicated that for the highest particle densities, we had to account for plasmon coupling between proximal GNPs to explain the observed LSPR spectra. Theoretical modelling showed that the plasmon coupling effect could only be explained assuming non-uniform distribution of particles in the hydrogel.

Thus, the effect of embedding spherical GNPs in the hydrogel FP cavity, as well as the feasibility of LSPR-based sensing using GNPs embedded in the hydrogel, have been discussed. However, the effect

of GNP shape, hydrogel swelling degree, bulk refractive index (RI), and the feasibility of LSPR-based biosensing in a hydrogel has not been elucidated. In this paper, we characterize the LSPR signal from gold nanorods (GNRs) embedded in an anionic hydrogel. We demonstrate interferometric measurement of hydrogel swelling up to a swelling degree of 6. Hydrogel swelling, induced by pH change, induces a small redshift of the LSPR peak wavelength, rather than the expected blueshift from the reduced averaged RI of the diluted polymer network. The observed redshift can be explained as a result of reduced side-by-side (s-s)-oriented plasmon coupling with hydrogel swelling. Increased bulk RI, using glycerol and sucrose, induces a large blueshift of the LSPR peak wavelength, contrary to the expected redshift from the increased medium RI. This blueshift can only be explained as a result of alteration of the surface electronic structure of the GNRs donated by the anionic polymer network and the glycerol or sucrose solutions [17–20]. In spite of these unexpected behaviors, we do show, using biotin-functionalized GNRs binding to streptavidin, that the LSPR signal from GNRs embedded in a hydrogel can be used for biosensing.

2. Polarizability of GNRs and Hydrogel as Low-Finesse FP Etalon

2.1. Fabry-Perot Interferometer

The stimuli-responsive hydrogel shown in Figure 1 represents a low-finesse FP etalon. The FP is interrogated using λ_1 light guided by the single-mode core. Confining the λ_1 light to a single transverse mode, both in the fiber and in the hydrogel volume, ensures effective interference between the field reflected at the fiber–gel interface and the field reflected at the gel–solution interface (as illustrated with red color in Figure 1).

The optical length l_0 and the length change Δl_0 can be estimated from the wavelength-dependent FP reflection. Both the reflection at the gel–solution interface, r_2 , and at the fiber–gel interface, r_1 , are small, such that the reflected intensity of the hydrogel FP can be approximated as

$$I_{\text{FP}}(\lambda) = I_0 \left[r_1^2 + (\gamma r_2)^2 + 2\gamma r_1 r_2 \cos \left(\frac{4\pi l_0}{\lambda} + \varphi_0 \right) \right] \quad (1)$$

where $k = \frac{2\pi}{\lambda}$, γ is a loss factor (due to absorption, scattering and mode mismatch), and φ_0 is the initial arbitrary phase. The free spectral range (FSR) is related to the optical length as

$$\text{FSR} = \frac{\lambda_0^2}{2l_0} \quad (2)$$

where λ_0 is the wavelength of observation. The length change is related to the phase change of the interferometric spectrum as

$$\Delta\phi = \frac{4\pi\Delta l_0}{\lambda_0} \quad (3)$$

The change in l_0 may originate from both a change in RI of the gel and from a change in the physical length l of hydrogel cavity,

$$\Delta l_0 = \Delta l n_{\text{gel}} + l \Delta n_{\text{gel}} \quad (4)$$

where n_{gel} is the RI of the gel, originating from both the solvent and the polymer concentration.

Over the short propagation distances used here (a few meters), the mode-coupling between the single-mode (SM) core and the MM cladding will be negligible. The crosstalk between the MM channel and the SM channel in the fiber coupler is not specified. However, since we are using spectrally resolved detection in both channels, we would not be affected by any coupler crosstalk.

2.2. LSPR of GNRs in Hydrogel

The LSPR of the GNRs in the hydrogel is probed using λ_{II} light guided in the MM-first cladding shown in Figure 1. By using the high NA of the large-diameter core for the λ_{II} light, we ensure effective excitation of a large fraction of the GNRs immobilized in the hydrogel volume and effective collection of the reflection from the LSPR of the GNRs (as illustrated with green color in Figure 1). The reflection from the GNRs in hydrogel on the OF end face is a result of the extinction that is the sum of scattering and absorption. With a sufficiently low GNR density, and absence of dipole–dipole interactions, the optical properties of GNRs in hydrogel can be described by Gans theory, a generalization of Mie theory for spheroidal particles [21,22]. In the quasi-static approximation, the polarizability of the longitudinal plasmon mode of GNRs is

$$\alpha = \frac{(1 + \kappa)V}{4\pi} \left(\frac{\varepsilon(\lambda) - \varepsilon_m}{\varepsilon(\lambda) + \kappa\varepsilon_m} \right) \quad (5)$$

$$\kappa = \frac{1 - L}{L} \quad (6)$$

$$L = \frac{1 - e^2}{e^2} \left[\frac{1}{2e} \ln \left(\frac{1 + e}{1 - e} \right) - 1 \right] \quad (7)$$

$$e = \sqrt{1 - \left(\frac{1}{AR} \right)^2} \quad (8)$$

where AR is the aspect ratio of the GNRs, $\varepsilon(\lambda) = \varepsilon_1 + i\varepsilon_2$ is the complex metal dielectric function, and V is the volume of the GNRs.

The polarizability is maximized when the real part of the metal dielectric function, $\varepsilon_1(\lambda)$, and the dielectric constant of the surrounding medium, ε_m , satisfy the relation

$$\varepsilon_1(\lambda) = -\kappa\varepsilon_m \quad (9)$$

By using the Drude model, the LSPR peak position as a function of local RI, $n_m = \sqrt{\varepsilon_m}$, can be described as

$$\lambda_{\max} = \lambda_p \sqrt{\kappa n_m^2 + 1} \quad (10)$$

where λ_p is the plasma oscillation wavelength of the bulk metal [23]. For the transverse resonance, we have to replace κ with $\kappa_T = \frac{1+L}{1-L}$.

For GNRs in close proximity to each other, the LSPR of the longitudinal plasmon mode will change with decreasing center-to-center interparticle distance d [24]. For two identical GNRs, the resonance permittivities of the dipole–dipole coupling for the longitudinal plasmon mode can be described by the point dipole model [25]. For the side-by-side (s-s) or the end-to-end (e-e) cluster configuration, the plasmon resonance condition becomes

$$\varepsilon_1(\lambda)_{(\pm)} = -\mathcal{F}_{(\pm)}\varepsilon_m \quad (11)$$

$$\mathcal{F}_{(\pm)} = - \left(\frac{g^2 + \kappa}{g^2 - 1} \pm \frac{g(\kappa + 1)}{g^2 - 1} \right) \quad (12)$$

$$g = \frac{\mathcal{N}(1 + \kappa)V}{4\pi d^3} \quad (13)$$

where $\mathcal{F}_{(+)}$ with $\mathcal{N} = 2$ represents the e-e configuration and $\mathcal{F}_{(-)}$ with $\mathcal{N} = 1$ represents the s-s configuration (dipole moment maximized with $\frac{a^2}{d^6} = 1$ for the s-s and with $\frac{4a^2}{d^6} = 1$ for the e-e

configuration). The LSPR peak position as a function of n_m and d can be further expressed by using the Drude model,

$$\lambda_{\max(\pm)} = \lambda_p \sqrt{\mathcal{F}_{(\pm)} n_m^2 + 1} \quad (14)$$

The plasmon resonance condition and λ_{\max} can be computed from Equation (11) and (14), as shown in Figure 2 for decreasing d . In the e-e configuration, a decrease in interparticle distance, d , will redshift the LSPR peak position, whereas in the s-s configuration a decrease in d will result in a blueshift.

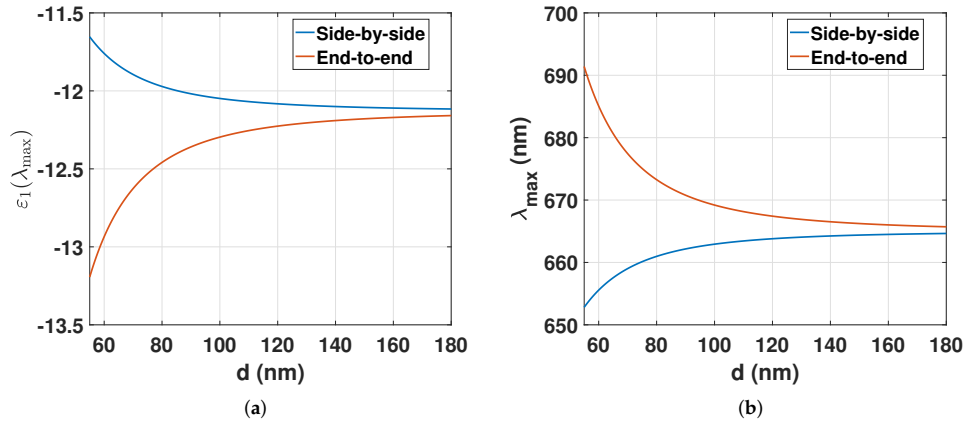


Figure 2. (a) Resonance permittivities (Equation (11)) of two identical GNRs in the s-s or e-e configuration for decreasing d ; (b) λ_{\max} (Equation (14)) of two identical GNRs in the s-s or e-e configuration for decreasing d . $\epsilon_m = n_m^2 = 1.33^2$, $\lambda_p = 183$ nm, GNR width = 19 nm, GNR length = 50 nm, and AR = 50/19.

Both absorption and scattering will contribute to the reflected LSPR signal. If we ignore interference effects (see discussion below) and assume for simplicity that scattering and absorption are weak, we can approximate the change in reflected power due to the GNRs as

$$\Delta P_R = (1 - R_1)^2 \left[\frac{1}{2} \left(\frac{\text{NA}}{4} \right)^2 \sigma_{\text{sc}} - R_2 \sigma_{\text{ex}} \right] \rho 2l P_{\text{in}} \quad (15)$$

where R_1 is the reflectance of the fiber–hydrogel interface, R_2 is the reflectance of the hydrogel–solution interface, ρ is the GNP density, and P_{in} is the input power. Depending on the relative strength of the scattering and extinction terms, we will either observe an LSPR reflection dip (net absorption) or a LSPR reflection peak (net scattering). For the particle sizes and densities, and hydrogel compositions used in this work, we observe a net absorption.

The FP interferences will not be observable using light propagating in the MM core due to modal dispersion in the OF cable and in the FP cavity. Assuming the propagation in the FP cavity can be described using Hermite-Gaussian beams with indexes (l, m) , the higher-order modes $((l, m) > (0, 0))$ propagate with an excess phase $(l + m) \tan^{-1}(\frac{z}{z_0})$, where z_0 is the Rayleigh range [26]. The DCOF carries several thousand modes (V-parameter is approximately 100) resulting in the same number of Hermite-Gaussian modes in the FP cavity. Therefore, the visibility of the FP interference will effectively be reduced to zero and will not be observable. Adding modal dispersion in the OF will further reduce the visibility.

3. Materials and Methods

Two sets of experiments were performed with two different GNR–hydrogel fiber-optic (FO) sensors; (1) the FSR and LSPR peak positions were measured as a function of pH and RI; (2) the LSPR peak positions were determined for nonfunctionalized GNRs in hydrogel, biotin-functionalized GNRs in hydrogel, and for the biotin–streptavidin recombination on the surface of the GNRs immobilized in the hydrogel.

3.1. Fabricating the GNR–Hydrogel

The FO sensors were fabricated as described from previous work [15,16]. Citrate-stabilized 670 nm-resonant GNRs (50 nm in length, 19 nm in diameter, 1.14×10^{13} particles/mL, 2 mM citrate buffer, nanoCompix) were used to make pregel solutions of 10 wt % acrylamide (AAM)–acrylic acid (AAC) (molar ratio 1/2 AAM/AAC) and 2 mol % *N,N*-methylenebisacrylamide (BIS).

3.2. Setup of the FO Sensor Instrument

The FO-sensor setup illustrated in Figure 3 consist of the following components; λ_{II} broadband source (MBB1F1, 470–850 nm, Thorlabs, Newton, NJ, USA), λ_I broadband source (S5FC1005S, 1550 nm, 50 nm bandwidth, Thorlabs), 50:50 coupler MM (50/50, FCMH2-FC, 400–1600 nm, Thorlabs), 50:50 coupler SM (50/50, 84075633, 1550 nm, Bredengen, Oslo, Norway), double-clad optical fiber (DCOF) coupler (DC1300LEB, MM 400–1700 nm, SM 1250–1550 nm, Thorlabs), λ_{II} spectrometer (QE65Pro, Ocean Optics, Dunedin, FL, USA), λ_I spectrometer (NIRQuest-512-1.7, Ocean Optics), loose fiber-end terminated with index-matching gel (G608N3, Thorlabs), LSPR and FP sensor segment with $\varnothing 125 \mu\text{m}$ DCOF (DCF13, Thorlabs).

Data acquisition was performed with the Spectrasuite program software (Ocean Optics) and the OFs were spliced using a Fitel Fusion Splicer (Furukawa Electric, Yokohama City, Japan).

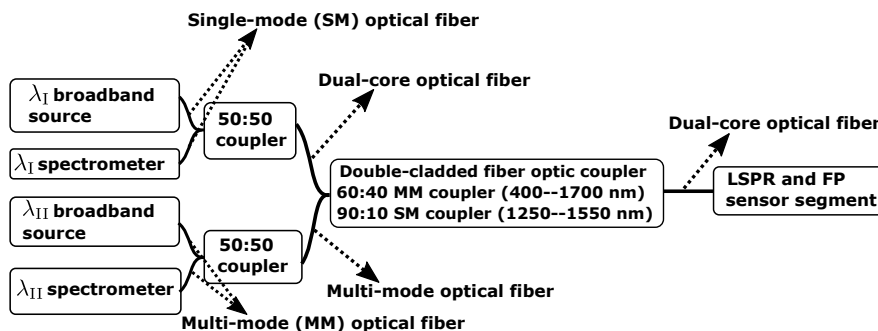


Figure 3. Setup of the fiber-optic instrument based on reflection measurements.

3.3. Preparation of Solutions for Hydrogel Swelling and LSPR Shifts

Hydrochloric acid (HCl) or sodium hydroxide (NaOH) (1.0 M, Sigma Aldrich, St. Louis, MI, USA) were added to Milli-Q water to prepare pH solutions to stimulate a change in volume of the hydrogel. pH was controlled with a pH meter (inoLab pH/ION 7320, WTW, New York, NY, USA), pH electrode (pHenomenal MIC 220, Van Water & Rogers (VWR) Collection, Radnor, PA, USA), and temperature sensor (pHenomenal TEMP21, VWR Collection). Glycerol (>99%, VWR) or Sucrose (>99.5%, VWR) were added to Milli-Q water to prepare RI solutions to induce shift in the LSPR peak position. The bulk RI values for different wt % (between 0 and 40 wt %) of glycerol and sucrose in Milli-Q water were obtained from the Handbook of Chemistry and Physics at $\lambda = 589 \text{ nm}$ [27].

3.4. Functionalizing GNRs in Hydrogel with Biotin for Biotin–Streptavidin Recombination

3.4.1. Functionalizing GNRs in Hydrogel with Biotin

Biotin with polyethylene glycol (PEG) chains terminated with a thiol group (Biotin-PEG (5k)-SH, powder, PG2-BNTH-5k, NANOCS Inc., New York, NY, USA) were reconstituted in Milli-Q solution to 0.01 M. Further, tris(2-carboxyethyl)phosphine hydrochloride (TCEP, powder, Sigma Aldrich) with 10 molar equivalents to biotin-PEG(5k)-SH were added to the 0.01 M biotin solution and stirred for 10 min to ensure that disulfide bonds were reduced to thiol groups. Next, the GNR–hydrogel on OF was immersed in the biotin solution for 10 min to let the thiol group bind to the GNRs. Last, the GNR–hydrogel on OF was transferred to Milli-Q water solution with pH 4.5 to remove any residues of biotin in the hydrogel.

3.4.2. Biotin–Streptavidin Recombination on GNRs in Hydrogel

Streptavidin (*Streptomyces avidinii*, powder, S4762, Sigma Aldrich) was reconstituted in phosphate-buffered solution (PBS, Sigma Aldrich) to a concentration of 1 mg/mL and readjusted to a pH of 4.5. The fiber–gel with biotin-functionalized GNRs was then immersed in the streptavidin solution for 10 min and transferred to Milli-Q water solution with pH 4.5.

3.5. Reflection Measurements of GNRs Embedded in Hydrogel in λ_{II} and λ_I

The reflectance spectra were estimated from the measured raw spectra, S_λ , normalized to a measured reference spectra, R_λ . Before normalization, we subtracted the measured dark spectrum, D_λ (recorded with the light source turned off), from both the raw spectra and a reference spectrum. The normalized reflectance spectra were then computed as

$$I_R = \left(\frac{S_\lambda - D_\lambda}{R_\lambda - D_\lambda} \right) \quad (16)$$

The hydrogel swelling, or deswelling, was induced by immersing the hydrogel–fiber in solutions with pH between 4.5 and 3.0. The change in LSPR was induced by immersing the hydrogel–fiber in glycerol or sucrose solutions with bulk RI between 1.330 and 1.385 at pH 4.5 and 3.0. For the biotin–streptavidin measurements, all spectra were recorded in Milli-Q water with pH at 4.5. For each solution, the hydrogel was left for 1 minute to reach equilibrium before sampling the spectrum. For convenience, we used different reference spectra for the different experiments:

- For the FP experiments, we used the reflection spectrum of the bare DCOF in Milli-Q water solution.
- For the LSPR experiments, we used the reflection spectra from the hydrogel without GNRs for each pH, glycerol and sucrose solution, to compensate for the artefacts in the LSPR spectra caused by the reflections at the fiber–gel interface.

3.6. Estimating the FSR and the LSPR Peak Position

We determined the FSR from the autocorrelation function of the reflectance spectra to relax the dependence on signal normalization. The autocorrelation function is symmetric and measures the correlation between $I_{R(i)}$ and $I_{R(i+k)}$ for lag time $k = 0, 1, 2 \dots (N-1)$, where N is the length of the vector received from the spectrometer. The autocorrelation coefficients for lag time k are described as

$$r_k = \frac{\sigma^2}{N-1} \sum_{i=1}^{N-k} (I_{R(i)} - \bar{I}_R)(I_{R(i+k)} - \bar{I}_R) \quad (17)$$

where \bar{I}_R is the mean of I_R , and σ^2 is the sample variance of the lag time-series [28]. To find the FSR, the centered and scaled smoothing spline function was applied on the first peak of the autocorrelation

function with a smoothing parameter at 0.99. With smoothing parameter $p = 0$, the smoothing spline function produces a least-squares line fit to the data, whereas with $p = 1$, the smoothing spline function produces a cubic spline interpolant. By choosing a fixed smoothing parameter, the balance between residual error and local variation is also fixed [29].

For λ_{II} reflectance measurements of GNPs, the LSPR spectrum was fitted with a centered and scaled smoothing spline function with smoothing parameter at 0.995.

4. Results

The quality of the interferometric and LSPR signals were first assessed and compared to previous work. Secondly, the FSR and the LSPR were measured as a function of hydrogel swelling degree to assess the influence of GNPs on the interferometric signal and to assess the influence of hydrogel deswelling on LSPR, respectively. Thirdly, the LSPR response and optical length were measured as a function of RI solutions. In addition, the LSPR peak positions were determined for constant and dynamic reference spectra for pH and RI measurements to determine the influence of the change in reflections at the gel–fiber interface on the LSPR signal. Last, the LSPR peak position was determined for the biotin–streptavidin recombination on GNPs in hydrogel.

4.1. Acquisition of LSPR and Interferometric Signals

The λ_I reflectance spectrum from a GNP–hydrogel in pH 4.5, together with the resulting autocorrelation function of the reflectance spectrum used to find the FSR, are shown in Figure 4.

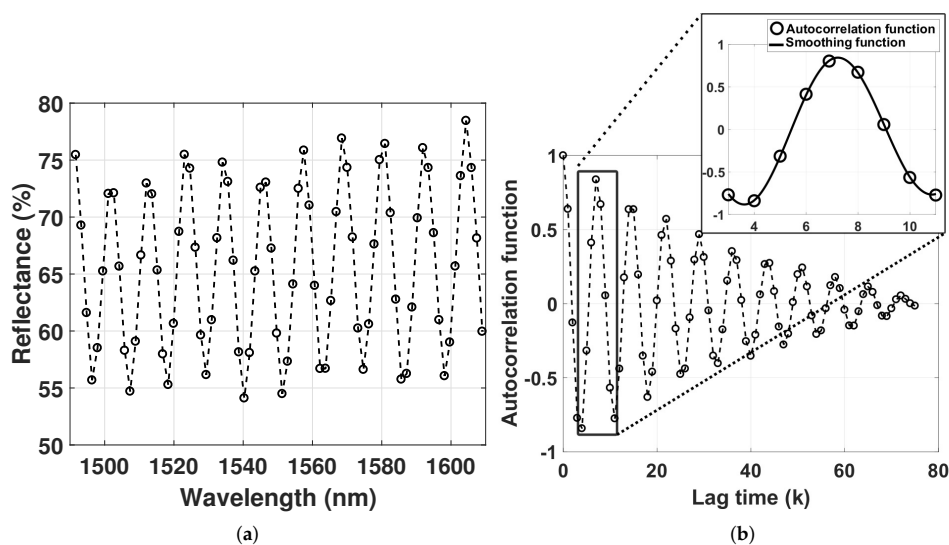


Figure 4. (a) Reflectance in the λ_I range from the hydrogel with GNPs in pH of 4.5; (b) autocorrelation function of the interferometric spectrum.

The smallest FSR in our experiments, at pH 4.5, corresponds to optical lengths of the hydrogel of around 100 μm , with visibility of approximately 0.15. Aggregation of GNPs in the hydrogel would significantly reduce the visibility of the interferogram. Thus, the degree of GNP aggregation can be assessed by monitoring the quality of the interferogram. The visibility in Figure 4a is, however, comparable to previously fabricated extrinsic Fabry–Perot interferometers (EFPI) despite using a GNP particle density of $1.14 \times 10^{13} \text{ mL}^{-1}$ [13] compared to $1.9 \times 10^{11} \text{ mL}^{-1}$ used in our earlier work [11,12].

The measured LSPR reflectance spectrum from the GNR-hydrogel in pH 4.5 shows a transverse plasmon mode at 519 nm and a longitudinal plasmon mode at 689 nm (Figure 5a). Due to the MM propagation and multi-transverse-mode hydrogel FP cavity, no interference fringes are observed. The longitudinal LSPR in Milli-Q water at pH 4.5 is redshifted by 19 nm compared to the LSPR in the citrate-buffered solution, due to the increased RI of the polymer network compared to the citrate-buffered solution.

The LSPR reflectance spectrum in Figure 5a rides on top of an 82% background dominated by the wavelength-independent Fresnel reflection at the fiber-hydrogel interface. In addition, there will be a small wavelength-dependent reflection from the hydrogel, both scattering from hydrogel inhomogeneities and from the hydrogel-solution interface. This signal contribution will also be modulated by any spectrally dependent propagation absorption in the hydrogel. As discussed in Section 3.5, to account for this, the LSPR spectrum is found by normalizing the measured reflected intensity from the GNR-hydrogel to the reflected intensity from another hydrogel without GNRs exposed to the same solution. However, due to sensor-to-sensor variation in hydrogel preparation, this normalization procedure is prone to errors. To explore this, we have quantified the effect of using a fixed reference spectrum for all LSPR reflectance spectra. As we can see from Figure 5b, for the sensor in Milli-Q water with varying pH, the effect of keeping the reference spectrum constant is insignificant.

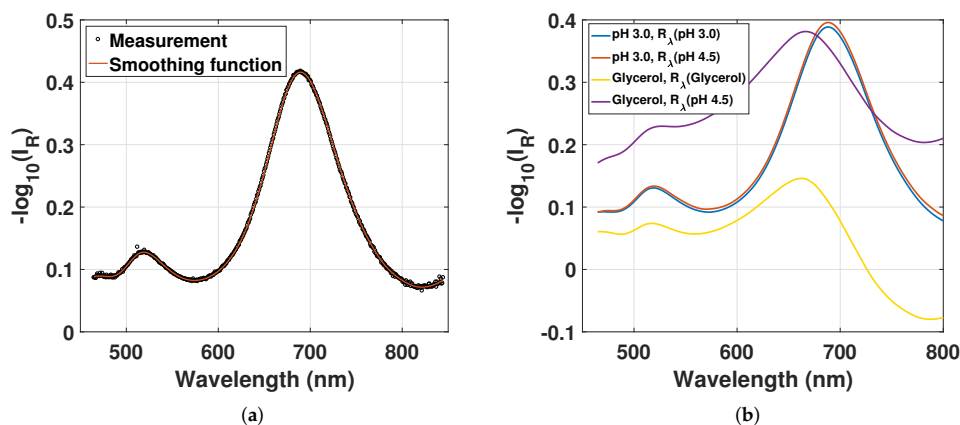


Figure 5. (a) Reflectance from the GNR-hydrogel with smoothing function, in pH 4.5 with R_λ (pH 4.5); (b) reflectance from the GNR-hydrogel in (1) pH 3.0 with R_λ (pH 3.0) and R_λ (pH 4.5) and (2) 40 wt % glycerol at pH 4.5 with R_λ (40 wt % glycerol, pH 4.5) and R_λ (pH 4.5).

This is due to the insignificant variation in RI with varying pH. On the other hand, in the experiments using solutions with glycerol (or sucrose), the effect of keeping the reference spectrum constant is large, as we see from the two glycerol traces in Figure 5b. The largest effect is due to the reduced Fresnel reflection at the fiber-hydrogel interface with increasing solution RI (increasing glycerol). However, the resulting shift in the estimated LSPR is moderate, since the reflection spectra from the hydrogel without GNRs are practically constant in the wavelength range of the longitudinal LSPR wavelength. These variations of the LSPR signal for constant or variable reference spectra are further discussed in Section 4.3. We define a resonant wavelength “error” as the resulting wavelength shift due to variation in the reference spectra used.

The figure of merit is expected to be larger for the longitudinal plasmon mode than the transverse plasmon mode. We have therefore used the longitudinal plasmon mode in both pH and RI measurements.

4.2. FSR Response for pH and RI

Figure 6 shows the measured FSR as a function of pH and bulk RI. We note that the GNRs do not disrupt the FSR measurements. The sensitivity of the interferometric sensor should therefore be similar to previous work on EFPI and sufficient for many applications [13]. The sensitivity can, however, be improved by detecting the change in phase, in addition to measuring the FSR [13,14].

The FSR as a function of increasing bulk RI prepared with glycerol and sucrose shows to have small variations at pH 4.5. At pH 3.0 there is, however, a slight decrease in FSR for increasing bulk RI. With initial FSR of 12 nm and 22 nm, the resulting change in optical lengths are $3.76 \mu\text{m}$ and $1.88 \mu\text{m}$ (from Equation (4)), respectively, for increasing RI from 1.33 to 1.38. A change in optical length of $3 \mu\text{m}$ due to increased RI will result in a 1.5 nm change in FSR ($\frac{\Delta\text{FSR}}{\text{FSR}} \propto \frac{\Delta l_0}{l_0}$ and $l_0 = 50 \mu\text{m}$). From Figure 6b, the change in FSR is, however, larger than this at pH 3.0. Thus, the decrease in FSR at pH 3.0 is most likely a result of the hydrogel swelling due to increased wt % of glycerol or sucrose.

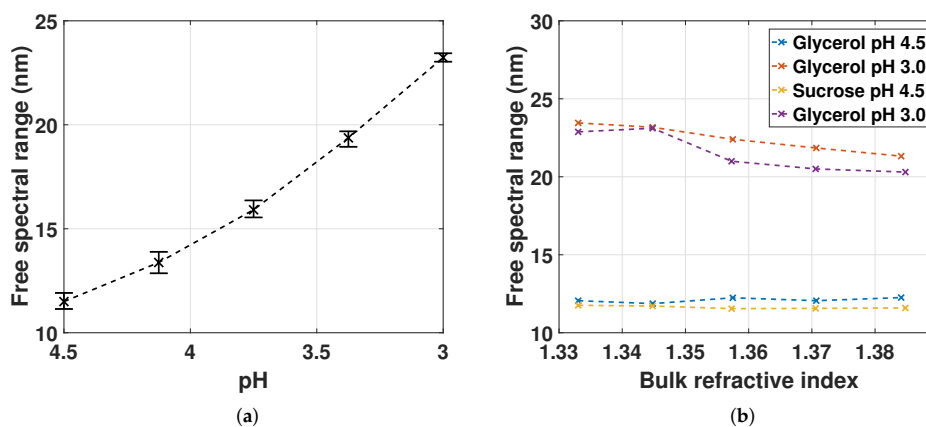


Figure 6. (a) FSR measured for the hydrogel deswelling from pH 4.5 to 3.0 for two sampled series with mean, minimum and maximum values from 4 sampled FSRs; (b) FSR measured for increasing bulk RI with pH 4.5 and 3.0 for one sampled series.

4.3. LSPR Response for pH and RI

Figure 7a shows the LSPR peak position as a function of pH from 4.5 to 3.0. The mean LSPR peak position for hydrogel deswelling shows a blueshift of 0.8 nm. Variations in the LSPR peak position can occur as a result of change in polymer density of the hydrogel or change in the interparticle distances between the GNRs, inducing electromagnetic interactions between longitudinal plasmon modes. As described in Section 2.2, decreasing interparticle distances for GNRs in an e-e configuration leads to an LSPR redshift, whereas for GNRs in an s-s orientation, decreasing interparticle distance leads to an LSPR blueshift. The observed blueshift of the mean LSPR peak position with hydrogel deswelling suggests increasing dipole–dipole interactions for a large fraction of the GNRs in the s-s configuration. The large fraction of GNRs in the s-s configuration might be due to many factors, for example, the polymerization process or the negatively charged polymer network. Investigations concerning the orientation of GNRs in hydrogel are works in progress. The variations of the LSPR peak positions for each pH value suggest that there is a weak dependence on the polymer density. This weak dependence is likely due to the low polymer density of the gel, as well as the small dimension of the RI “probes” of GNRs with size of $\sim 50 \text{ nm}$.

The estimated LSPR wavelength error due to variations in the reference spectra (Equation (16)) for decreasing pH is shown in Figure 7b. The estimate is computed from the measured mean LSPR

peak position using constant R_λ (pH 4.5) subtracted from the mean LSPR peak position from Figure 7a. The LSPR reflection spectrum concerning the background intensity was also discussed in Figure 5. The small wavelength resonance error for decreasing pH demonstrates that the change in background intensity (Fresnel reflection coefficients) from the fiber–gel interface introduces negligible change in the LSPR peak position when keeping the reference spectrum constant at R_λ (pH 4.5). Thus, despite the large variations in the optical length of a hydrogel cavity, it is feasible to use one reference spectrum from the hydrogel without GNRs in the λ_{II} range.

Figure 8a shows the LSPR peak position measured for increasing bulk RI at pH 4.5 and 3.0. The LSPR peak position is blueshifting with a nonlinear trend for increasing bulk RI. The blueshifts at pH 3.0 are larger than at pH 4.5 for both glycerol and sucrose solutions. The LSPR response is also different for glycerol and sucrose solutions. The total change in LSPR peak position for the change in RI is ~ 677 nm/RIU. This is in contrast to the expected linear redshift for a LSPR RI probe (from Equation (10) the redshift should be approximately 500 nm/RIU). The RI on the outside and the inside of the GNR–hydrogel is expected to be similar, since glycerol and sucrose are water soluble, and therefore solvents for the hydrogel. The observed blueshift must therefore be due to the nature of the local surrounding medium [17–20]. In previous work, the optical properties of cetylpyridinium chloride-stabilized gold nanoparticles when exposed to various solvents were studied [19]. The LSPR peak position was shown to be greatly influenced by the properties of the solvent and the removal or donation of electron density onto gold particles. In another study, the LSPR peak position of chitosan-stabilized gold nanoparticles exhibited a blueshift for the specific detection of increasing concentration of mercury in liquid solutions [20]. The blueshift observed in Figure 8a for increasing bulk RI could then be a result of the alteration of the surface electronic structure of the GNRs donated by the charged AAM–AAC polymer network and the glycerol or sucrose solutions. At pH 4.5, the hydrogel has a large fraction of negatively charged AAC, as opposed to the small fraction at pH 3.0. The increase in LSPR blueshift from pH 4.5 to pH 3.0 could be due to the decrease in the negative charge of the gel, changing the donation of electron density onto the GNRs. In addition, the sucrose solutions decrease the LSPR peak position compared to the glycerol solutions. This is also an indication of a change in the solvent properties of the water in gel that is different for glycerol and sucrose.

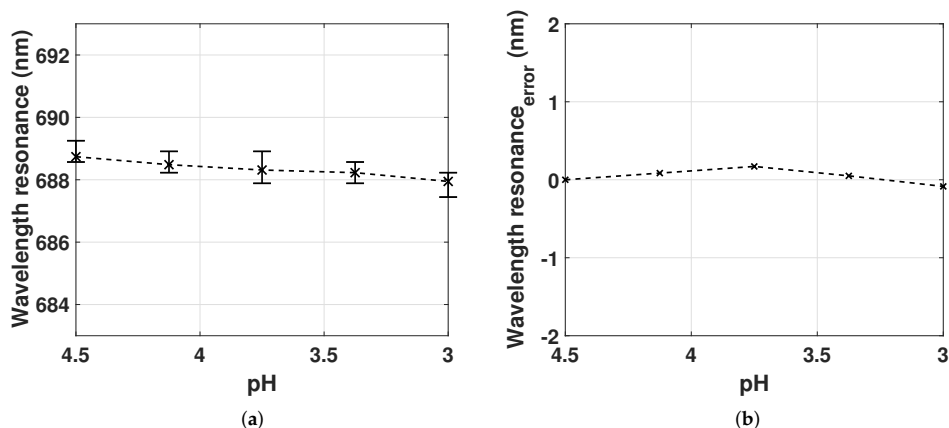


Figure 7. (a) LSPR peak position measured for the hydrogel deswelling from pH 4.5 to 3.0 for two sampled series with mean, minimum and maximum values from 4 sampled LSPR peak positions; (b) the error of the LSPR peak position by holding the reference spectrum constant at R_λ (pH 4.5) for pH 4.5 to 3.0. RI = 1.33 (Milli-Q water).

The LSPR wavelength error for increasing bulk RI is presented in Figure 8b. It is computed from the measured LSPR peak position with constant R_λ (pH 4.5) subtracted the LSPR peak position from Figure 8a. The uncertainty from the change in reflection at the fiber–gel interface is increasing for increasing bulk RI. This is likely caused by the change in background intensity from the fiber–gel interface as a result of the change in Fresnel reflection coefficients for increasing glycerol or sucrose wt%. The uncertainty values are similar for increasing bulk RI up to 1.37 for all solutions, except for sucrose at pH 3.0. The Fresnel reflection coefficients at the fiber–gel interface are therefore similar for all solutions up to RI of 1.37, except for sucrose at pH 3.0.

The maximum estimated LSPR wavelength error (up to 10 nm) is still smaller than the total LSPR blueshift observed in Figure 8a. The blueshift is therefore not due to the uncertainties in the reference spectra used in our measurements. The study of the influence of the hydrogel and solvents on the LSPR of gold nanospheres or rods is a work in progress.

Note that for label-free biosensing with LSPR, it is only the surface of the GNRs that senses changes in RI. The Fresnel reflection coefficients at the fiber–gel interface are therefore not expected to change upon receptor–analyte recombination. The results obtained in Figures 6–8 therefore prove the utility of immobilizing GNRs in hydrogel to measure both interferometric and LSPR signals with acceptable levels of crosstalk [14,30].

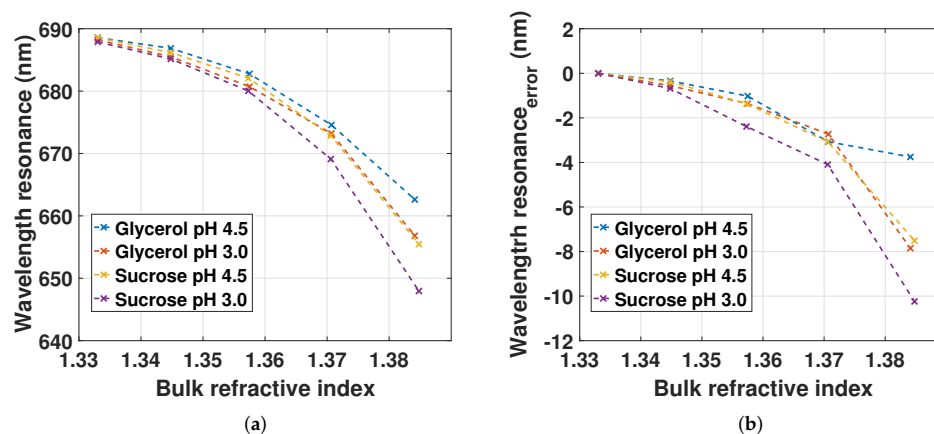


Figure 8. (a) LSPR peak position as a function of bulk RI with pH 4.5 and 3.0 for one sampled series; (b) the error of the LSPR peak position by holding the reference spectrum constant at R_λ (pH 4.5) for increasing bulk RI with pH 4.5 and 3.0

4.4. Biotin–Streptavidin Recombination on GNRs in Hydrogel

Figure 9 shows the λ_{II} reflectance for nonfunctionalized GNRs, biotin-functionalized GNRs and biotin–streptavidin recombination on GNRs in hydrogel in Milli-Q water with pH at 4.5. The transverse and longitudinal LSPR peak positions of the nonfunctionalized GNRs are at 518.75 and 672.35 nm, respectively. The LSPR peak position deviates from the peak positions for the FO sensor used for the pH and RI measurements. The difference in LSPR peak positions obtained for different fabricated OF sensors may be due to the different RI “probing” of the polymer network due to the polymerization process resulting in polymer chains in close proximity to the plasmonic waves on the GNRs.

By functionalizing the GNRs with biotin, the transverse LSPR redshifts by 1.52 nm, whereas the longitudinal LSPR redshifts by 1.45 nm. The changes in transverse and longitudinal LSPRs indicate that the biotin–PEG thiol group is distributed on both the sides and ends of the GNRs. Recombination of biotin–streptavidin on the GNRs changes the transverse and the longitudinal LSPRs by another 0.76 and 7.62 nm, respectively, which also indicates that streptavidin is distributed on both the sides and

ends. The interferometric signal was unstable during the biotin functionalization due to the low pH, around 2, of the biotin solution, but recovered approximately to the initial signal and initial FSR value after the functionalization in solution of pH 4.5. During streptavidin recognition, the interferometric signal and FSR were approximately constant.

The 7.6 nm redshift for the streptavidin recognition is similar to previous studies on the LSPR response of GNR towards analytes [31]. The ratio between the total shift of the longitudinal and the transverse plasmon mode is 3.97 (9.05 nm/2.28 nm). From Equation (10) we estimate the expected longitudinal-to-transverse LSPR shift ratio to be 4.1 ($\frac{\partial\lambda_L}{\partial\lambda_T} = \frac{\kappa_L\lambda_T}{\kappa_T\lambda_L}$, AR = 2.63, $\kappa_L = \frac{1-L}{L}$, $\kappa_T = \frac{1+L}{1-L}$, $\kappa_L = 6.85$, $\kappa_T = 1.29$), which is consistent with the observed shift ratio.

While the LSPR in Figure 8a is dependent on the RI and the solvent attributes of increasing wt % of glycerol or sucrose within the gel, the LSPR in Figure 9 is only dependent on the change in RI on the surface of the GNRs in the hydrogel due to the biotin–streptavidin recombination. As the discrimination is made between the change in local RI and bulk RI from the measurements obtained in Figures 8a and 9, this indicates that the blueshift for increasing glycerol or sucrose is a result of the solvent properties of water–glycerol or water–sucrose and the gel, changing the donation of electron density onto the GNRs as discussed in Section 4.3.

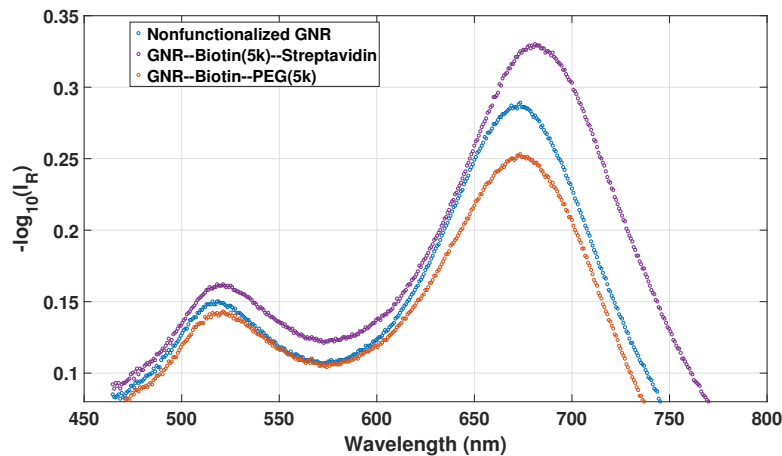


Figure 9. λ_{II} reflectance spectra for bare GNRs, biotin-functionalized GNR and biotin–streptavidin recombination on GNRs in hydrogel in Milli-Q water with pH at 4.5.

4.5. Summary of Results

We have created a summary of the results, shown in Tables 1 and 2, to present an overview of the main findings.

Table 1. Summary of results for interferometric sensor in the λ_I range.

Stimuli	Free Spectral Range Shift	Mechanism
Hydrogel deswelling	Large increase	Decreased physical length
Bulk refractive-index increase	Small decrease	Hydrogel swelling due to solvent

Table 2. Summary of results for LSPR sensor in the λ_{II} range.

Stimuli	LSPR Shift	Mechanism
Hydrogel deswelling	Small blueshift	Increased plasmon coupling
Bulk refractive-index increase	Large blueshift	Change in local surrounding media
Analyte binding to receptors	Redshift	Local refractive index increase

5. Conclusions

We have reported on the characterization of an optical fiber-based multi-parameter sensor concept based on combining the LSPR signal and interferometric sensing using a double-clad optical fiber. The sensor consists of a micro-Fabry–Perot in the form of a hemispherical stimuli-responsive hydrogel with immobilized gold nanorods on the facet of a cleaved fiber. The swelling degree of the hydrogel is measured interferometrically using the single-mode inner core, while the LSPR signal is measured using the multi-mode inner cladding.

We have explored the effect of hydrogel swelling and variation of bulk solution RI on the LSPR peak wavelength, demonstrating that pH-induced hydrogel swelling causes only weak redshifts of the longitudinal LSPR mode of the nanorods, while increased bulk RI using glycerol and sucrose causes large blueshifts. The redshifts with hydrogel swelling are likely due to the reduced plasmon coupling in the side-by-side configuration, as the interparticle distance increases with increasing swelling. The total redshift is less than 1 nm for an optical cavity length change from 55 μm to 100 μm , corresponding to a volume-swelling degree of 6. Thus, the variations of the LSPR peak position will be negligible for optical length changes within a smaller range in the volumetric measurements of stimuli-responsive hydrogel. The blueshifts with increasing bulk RI are likely due to alteration of the surface electronic structure of the GNRs donated by the charged AAM–AAC polymer network and glycerol or sucrose solutions. Therefore, care must be taken when using this sensor concept for bulk RI sensing. Both the hydrogel properties and the molecular species causing the RI change must be accounted for.

To explore the feasibility of using the sensor concept for biosensing, that is, measuring the local RI change due to binding to receptors at the GNR surfaces, we used the biotin–streptavidin system. The recombination of biotin–streptavidin on GNRs in hydrogel in Milli-Q water at pH 4.5 showed a 7.6 nm redshift of the longitudinal LSPR. The LSPR response of biotin–streptavidin recombination is due to the change in local RI, which is possible to discriminate from the LSPR response due to changes in bulk RI.

The quality of the interferometric signal is comparable to previous work on EFPI hydrogel-based FO systems, despite having GNRs immobilized in the gel. The FSR increased monotonically for hydrogel deswelling controlled with pH solution, demonstrating the feasibility of utilizing stimuli-responsive hydrogel containing GNRs for label-free sensing. Detecting the phase of the interferometric signal in addition to the FSR would further improve the sensitivity [13].

The FSR and LSPR measurements of the hydrogel swelling degree and biotin–streptavidin recombination prove the utility of immobilizing GNRs in hydrogels to measure both interferometric and LSPR signals with acceptable levels of crosstalk for use in, for example, medical applications [14,30]. Further work will consist of realizing the LSPR and interferometric FO system as a biosensor towards medical applications where specific markers will be detected [14,30,32,33]. The influence of hydrogel and solvent on gold nanospheres and nanorods will also be studied further, in terms of characterizing their configuration and LSPR response.

Acknowledgments: This work was supported by strategic research funding from Norwegian University of Science and Technology (NTNU). The work was also supported in part by the Interreg Sweden-Norway program (IR2015.01) and Energy and Sensor Systems (ENERSENSE, strategic research program at NTNU).

Author Contributions: Harald Ian Muri, Andon Bano and Dag Roar Hjelme conceived and designed the experiments; Harald Ian Muri and Andon Bano performed the experiments; Harald Ian Muri, Andon Bano and Dag Roar Hjelme analyzed the data; Harald Ian Muri and Dag Roar Hjelme wrote the paper.

Conflicts of Interest: The authors declare no conflict of interest

References

- Dahlin, A.B. Size Matters: Problems and Advantages Associated with Highly Miniaturized Sensors. *Sensors* **2012**, *12*, 3018–3036.
- Gorris, H.H.; Blicharz, T.M.; Walt, D.R. Optical-fiber bundles. *FEBS J.* **2007**, *274*, 5462–5470.
- Choudhary, T.R.; Tanner, M.G.; Megia-Fernandez, A.; Harrington, K.; Wood, H.A.; Chankeshwara, S.; Zhu, P.; Choudhury, D.; Yu, F.; Thomson, R.R.; et al. Multiplexed Fibre Optic Sensing in the Distal Lung (Conference Presentation). Presented at the SPIE BiOS, San Francisco, CA, USA, 28 January–2 February 2017; Volume 10058, p. 100580E.
- Vindas, K.; Engel, E.; Garrigue, P.; Livache, T.; Arbault, S.; Sojic, N.; Leroy, L. Nano-structured optical fiber bundles for remote SPR detection: A first step toward in vivo biomolecular analysis. In Proceedings of the 2017 25th Optical Fiber Sensors Conference (OFS), Jeju, Korea, 24–28 April 2017; Volume 10323, pp. 1–4.
- Zhang, Z.; Chen, Y.; Liu, H.; Bae, H.; Olson, D.A.; Gupta, A.K.; Yu, M. On-fiber plasmonic interferometer for multi-parameter sensing. *Opt. Express* **2015**, *23*, 10732–10740.
- Albert, J.; Shao, L.Y.; Caucheteur, C. Tilted fiber Bragg grating sensors. *Laser Photonics Rev.* **2013**, *7*, 83–108.
- Guo, T.; Liu, F.; Guan, B.O.; Albert, J. [INVITED] Tilted fiber grating mechanical and biochemical sensors. *Opt. Laser Technol.* **2016**, *78*, 19–33.
- Epstein, J.R.; Walt, D.R. Fluorescence-based fibre optic arrays: A universal platform for sensing. *Chem. Soc. Rev.* **2003**, *32*, 203–214.
- Michael, K.L.; Taylor, L.C.; Schultz, S.L.; Walt, D.R. Randomly Ordered Addressable High-Density Optical Sensor Arrays. *Anal. Chem.* **1998**, *70*, 1242–1248, doi:10.1021/ac971343r, PMID:9553489.
- Sciacca, B.; Monro, T.M. Dip Biosensor Based on Localized Surface Plasmon Resonance at the Tip of an Optical Fiber. *Langmuir* **2014**, *30*, 946–954, doi:10.1021/la403667q, PMID:24397817.
- Muri, H.I.D.I.; Bano, A.; Hjelme, D.R. First step towards an interferometric and localized surface plasmon fiber optic sensor. In Proceedings of the 25th Optical Fiber Sensors Conference (OFS), Jeju, Korea, 24–28 April 2017.
- Muri, H.I.D.I.; Bano, A.; Hjelme, D.R. A single point, multiparameter, fiber optic sensor based on a combination of interferometry and LSPR. *JLT* **2018**, Accepted for publication.
- Tierney, S.; Hjelme, D.R.; Stokke, B.T. Determination of Swelling of Responsive Gels with Nanometer Resolution. Fiber-Optic Based Platform for Hydrogels as Signal Transducers. *Anal. Chem.* **2008**, *80*, 5086–5093.
- Tierney, S.; Falch, B.M.H.; Hjelme, D.R.; Stokke, B.T. Determination of Glucose Levels Using a Functionalized Hydrogel Optical Fiber Biosensor: Toward Continuous Monitoring of Blood Glucose in Vivo. *Anal. Chem.* **2009**, *81*, 3630–3636.
- Muri, H.I.D.I.; Hjelme, D.R. Novel localized surface plasmon resonance based optical fiber sensor. *Proc. SPIE* **2016**, *9702*, 97020L-1.
- Muri, H.I.D.I.; Hjelme, D.R. LSPR Coupling and Distribution of Interparticle Distances between Nanoparticles in Hydrogel on Optical Fiber End Face. *Sensors* **2017**, in press.
- Wang, C.; Ohodnicki, P.R.; Su, X.; Keller, M.; Brown, T.D.; Baltrus, J.P. Novel silica surface charge density mediated control of the optical properties of embedded optically active materials and its application for fiber optic pH sensing at elevated temperatures. *Nanoscale* **2015**, *7*, 2527–2535.
- Ohodnicki, P.R., Jr.; Wang, C. Optical waveguide modeling of refractive index mediated pH responses in silica nanocomposite thin film based fiber optic sensors. *J. Appl. Phys.* **2016**, *119*, 064502, doi:10.1063/1.4941103.
- Ghosh, S.K.; Nath, S.; Kundu, S.; Esumi, K.; Pal, T. Solvent and Ligand Effects on the Localized Surface Plasmon Resonance (LSPR) of Gold Colloids. *J. Phys. Chem. B* **2004**, *108*, 13963–13971, doi:10.1021/jp047021q.
- Radhakumary, C.; Sreenivasan, K. Gold nanoparticles generated through “green route” bind Hg²⁺ with a concomitant blue shift in plasmon absorption peak. *Analyst* **2011**, *136*, 2959–2962.

21. Mie, G. Beiträge zur Optik trüber Medien, speziell kolloidaler Metallösungen. *Ann. Phys.* **1908**, *330*, 377–442.
22. Gans, R. The Form of Ultramicroscopic Gold Particles. *Ann. Phys.* **1912**, *37*, 881–900.
23. Jensen, T.R.; Duval, M.L.; Kelly, K.L.; Lazarides, A.A.; Schatz, G.C.; Van Duyne, R.P. Nanosphere Lithography: Effect of the External Dielectric Medium on the Surface Plasmon Resonance Spectrum of a Periodic Array of Silver Nanoparticles. *J. Phys. Chem. B* **1999**, *103*, 9846–9853.
24. Jain, P.K.; Eustis, S.; El-Sayed, M.A. Plasmon Coupling in Nanorod Assemblies: Optical Absorption, Discrete Dipole Approximation Simulation, and Exciton-Coupling Model. *J. Phys. Chem. B* **2006**, *110*, 18243–18253, doi:10.1021/jp063879z, PMID:16970442.
25. Klimov, V.V.; Guzatov, D.V. Optical properties of an atom in the presence of a two-nanosphere cluster. *Quantum Electron.* **2007**, *37*, 209.
26. Saleh, B.E.A.; Teich, M.C. *Fundamentals of Photonics*, 2nd ed.; Wiley: Hoboken, NJ, USA, 2007; Chapter 3.2.
27. Haynes, W.M. *Handbook of Chemistry and Physics*, 97th ed.; CRC Taylor and Francis Group: Boca Raton, FL, USA, 2016; pp. 2016–2017.
28. Box, G.E.; Jenkins, G.M.; Reinsel, G.C.; Ljung, G.M. *Time Series Analysis: Forecasting and Control*; John Wiley & Sons: Hoboken, NJ, USA, 2015.
29. Silverman, B.W. Some Aspects of the Spline Smoothing Approach to Non-Parametric Regression Curve Fitting. *J. R. Stat. Soc. Ser. B (Methodol.)* **1985**, *47*, 1–52.
30. Sanders, M.; Lin, Y.; Wei, J.; Bono, T.; Lindquist, R.G. An enhanced {LSPR} fiber-optic nanoprobe for ultrasensitive detection of protein biomarkers. *Biosens. Bioelectron.* **2014**, *61*, 95–101.
31. Marinakos, S.M.; Chen, S.; Chilkoti, A. Plasmonic Detection of a Model Analyte in Serum by a Gold Nanorod Sensor. *Anal. Chem.* **2007**, *79*, 5278–5283, doi:10.1021/ac0706527, PMID:17567106.
32. Hjelme, D.R.; Aune, O.; Falch, B.; Østling, D.; Ellingsen, R. Fiber-Optic Biosensor Technology for Rapid, Accurate and Specific Detection of Enzymes. In *Advanced Photonics*; Optical Society of America: Washington, DC, USA, 2014; p. JTU6A.3.
33. Jeong, H.H.; Erdene, N.; Park, J.H.; Jeong, D.H.; Lee, H.Y.; Lee, S.K. Real-time label-free immunoassay of interferon-gamma and prostate-specific antigen using a Fiber-Optic Localized Surface Plasmon Resonance sensor. *Biosens. Bioelectron.* **2013**, *39*, 346–351.



© 2018 by the authors. Licensee MDPI, Basel, Switzerland. This article is an open access article distributed under the terms and conditions of the Creative Commons Attribution (CC BY) license (<http://creativecommons.org/licenses/by/4.0/>).

PAPER IV

Mapping the Distribution of Particles in Hydrogel in Use for Nanoplasmonic Biosensors: A Comparison of Preparation Methods

Harald Ian Muri, Linh Hoang, and Dag Roar Hjelm

Norwegian University of Science and Technology, Gunnerus Gate 1, 7012 Trondheim, Norway; harald.muri@ntnu.no (H.I.M.) Department of Electronic Systems; linh.hoang@ntnu.no (L.H.) Department of Clinical and Molecular Medicine/Cellular and Molecular Imaging Core Facility; dag.hjelme@ntnu.no (D.R.H.) Department of Electronic Systems

Abstract

The distribution of noble metal nanoparticles in hydrogels are influencing their nanoplasmonic response and signal used for biosensor purposes. By controlling the particle distribution, it is possible to obtain new nanoplasmonic features with new sensing modalities. Particle distributions can be characterized by using volume-imaging methods such as the focused ion beam-scanning electron microscope (FIB-SEM) or the serial block-face scanning electron microscopy (SBFSEM) techniques. Since the pore structure of hydrogels is contained by the water absorbed in the polymer network it may pose challenges for volume-imaging based on electron microscope techniques since the sample must be in a vacuum chamber. The structure of hydrogels can be conserved by choosing appropriate preparation methods, which also depends on the composition of the hydrogel used. In this paper, we have prepared low weight-percentage hydrogels, with and without gold nanorods (GNR) for conventional SEM imaging by using two different drying techniques; (1) the critical point drying (CPD) technique and (2) hexamethyldisilazane (HMDS) drying of hydrogels. A qualitative characterization of the GNR-hydrogels was carried out to study the GNRs positioned in the polymer network. The effect of the two different drying methods on the hydrogel morphology were also compared. The use of HMDS as an alternative to the CPD has several advantages involving less parametrical variables for drying, involving less effort, being cost-effective, and requires no equipment use. Also, choosing an optimized sample preparation method for SEM with optimized imaging parameters is important for obtaining accurate information about materials that is not correlated to artifacts. The results obtained from the preparation methods and SEM imaging parameters in this paper are useful for developing methods for mapping the metal particle distributions in micro-hydrogels by using FIB-SEM or SBFSEM techniques.

Keywords: metal nanocomposite hydrogels; particle distribution; nanoplasmonic sensor; preparation methods; SEM imaging; volume imaging;

1. Introduction

The ability of a hydrogel to absorb large amounts of water without being dissolved have shown to be useful in a significant number of applications such as drug delivery systems, wound healing, protein purification, crystallization of minerals, distillation, pollutant capturing and sensor technologies [1–10]. The synthesis of hydrogels with properties as defined by the application in mind is possible by controlling the crosslinking density of the hydrogel, the polymer hydrophilicity, type of recognition entities as co-monomers in the polymer network, polymer ionicity, or polymer elasticity. The common functions of the polymer network consist of responding volumetrically to external stimuli such as pH [11–13], temperature [14–16], ionic strength [17–19], or receptor-analyte recombinations [20–23]. Some of these stimuli-responsive features have shown to be very useful in controlling drug release [1] or to be useful for label-free and specific sensing of biomolecules [21, 24]. Other properties of the gel-polymer network may also be of importance for the crystallization of minerals [4, 25] or for the nucleation and growth of metal nanoparticles made by chemical reduction in the nano-fillers of the hydrogel matrix [26, 27]. These hydrogels embedded with noble metal nanoparticles (NMNP) are fascinating materials often utilized for wound healing [28, 29], but also impressive materials as nanoplasmonic systems [30, 31]. In membrane technology, NMNPs have also shown to be a

potential candidate for developments in thermoplasmonics that may improve nanofiltration, pervaporation processes or oil-in-water nanoemulsions [32–35]. NMNPs distributed in hydrogels exhibit intense optical scattering at specific light frequencies. This phenomena arise from light interacting with confined collective oscillations of electron clouds in the NMNPs at a resonance frequency, also known as localized surface plasmon resonance (LSPR) [36–38]. LSPR of NMNPs may occur in the visible or infrared light-range and are frequently used in label-free biosensor applications due to the fast response times, high sensitivity, high selectivity and possibility for multianalyte sensing in complex mixtures [36, 39–41]. LSPR of NMNP-hydrogels are dependent on the particle shape, size, the refractive index (RI) of the surrounding medium and the interparticle distances [42]. Coupling may occur between the resonant modes of the localized surface plasmons of NMNPs in close proximity to each other [43–46]. The scattering of NMNPs in a hydrogel may have a LSPR frequency for a random distribution of particles that is different from the LSPR frequency for an inhomogeneous particle distribution.

We have in earlier work developed proof-of-concepts fiber optic (FO) sensors based on using NMNPs immobilized in polyacrylamide hydrogels and combining LSPR and interferometric sensing modalities [47–49]. The interferometric sensing modality detects the change in volume of a stimuli-responsive hydrogel whereas the LSPR sensing modality detects receptor-analyte recombinations on the NMNP surface. The dipole-dipole coupling and RI sensitivity of the LSPR in NMNPs may as well be utilized for detecting the change in volume of stimuli responsive hydrogels for significant swelling and deswelling. The LSPR response of spherical or spheroidal GNPs in hydrogels showed to be deviating from the LSPR response of randomly distributed spherical or spheroidal GNPs [47–49]. The plasmon coupling between spherical GNPs occurred for larger interparticle distances than expected [47]. This was found to be due to the inhomogeneous distribution of the particles in the hydrogel. The LSPR response for decreasing interparticle distances where dominated by the side-by-side plasmon coupling between spheroidal GNPs [49]. This was likely due to an ordered tendency of the spheroidal particles in the hydrogel. To further understand and engineer the LSPR properties of GNP-hydrogels for biosensing purposes, it is possible to identify how the particles are ordered and distributed from morphological characterizations.

Morphological characterizations of hydrogels are often performed by using scanning electron microscopy (SEM). By using specialized SEM techniques, such as cryoSEM or environmental-SEM, it is possible to characterize the morphology of hydrogels in their swelled state [50, 51]. Specialized SEM may have limit accessibility due to being a state-of-art technology. Conventional SEM techniques requires the samples to be in a vacuum, which can pose challenges for conserving the native hydrated state of the hydrogel since its structure is contained by the water absorbed in the polymer network. To prevent a complete collapse of the hydrogel in the SEM vacuum chamber one can use drying methods such as high or low temperature drying [52–54] or critical point drying (CPD) [51, 53, 55, 56] to conserve its pore structure. Different collapsing characteristics occurs depending on the drying methods used and the composition of the hydrogel [53, 57, 58]. By using transmission electron microscopy, the high contrast of metal nanoparticles embedded in hydrogels can be observed, though, only a two dimensional particle distribution can be quantized [27, 59]. To map the three-dimensional distribution of particles in hydrogels with volume imaging methods, such as the focused ion beam-SEM technique (FIB-SEM) [60–62], conventional drying methods must be used. The CPD technique is a common method for drying hydrogels to conserve the morphology in SEM imaging [51, 53, 55, 56]. An alternative to CPD is to dry the samples with hexamethyldisilazane (HMDS) solvent in air. The surface tension of the sample is reduced by using HMDS and it may also cross-link proteins for biological materials [63]. This is adding strength to the sample during air-drying and prevents collapse or fracturing. Qualitative comparison of samples dried with CPD or HMDS for SEM have in previous work often been performed for biological specimen [64–67]. The air-drying with HMDS as an alternative to the CPD technique has its advantages; (1) less effort and fewer variables are involved; (2) it is cost-effective and (3) the method requires no equipment use. The HMDS may reduce surface tension for all hydrophilic materials and, therefore, serve as a useful drying method for hydrogels. The HMDS drying of fibrin or elastin hydrogels have been described in earlier work [68–71]. Also, the sputter coating of the sample maybe have to be optimized concerning coating thickness and coating material. Samples with significant differences in the topography may require a thicker coating than for samples with small differences in topography, i.e. the SEM imaging of the GNPs and the hydrogel structure may have conflicting requirements. The optimization of the sputter coating is out of scope in this article.

In this paper the morphology of 10 wt% polyacrylamide (AAM-BIS) and poly(acrylamide-co-acrylic acid) (AAM-AAC-BIS) hydrogels, with and without gold nanorods (GNR), by using conventional SEM have been studied. The hydrogels were prepared for SEM by using the CPD and the drying with HMDS. The effect of the two different drying

methods on the hydrogels morphology was compared. The comparison of the drying methods are useful for assessing HMDS as a drying method for acrylamide based hydrogels. Furthermore, a qualitative characterization of the GNR-hydrogels was carried out to study the GNRs positioned in the polymer network. Choosing an optimized sample preparation method for SEM with optimized imaging parameters is important for obtaining accurate information about materials that is not correlated to artifacts. The morphological results of the GNR-hydrogels obtained in this paper are useful as a first step in developing methods for mapping the distribution of particles in a micro-hydrogel by using volume imaging methods such as the FIB-SEM and the serial block-face scanning electron microscopy (SBFSEM) techniques [60–62, 72, 73]. By identifying how the particles are ordered and distributed in GNP-hydrogels, the LSPR properties can be defined and further engineered.

2. Experimental Section

2.1. Materials for synthesizing hydrogels

The materials used for synthesizing hydrogels, with and without GNPs, are as follows; acrylamide (AAM) (99%, Sigma Aldrich, Schnelldorf, Germany), acrylic acid (AAC) (99%, Sigma Aldrich), *N,N*-methylenebisacrylamide (BIS) ($\geq 99.5\%$, Sigma Aldrich), 1-hydroxycyclohexyl phenyl ketone (99%, Sigma Aldrich), dimethyl sulfoxide (DMSO) ($\geq 99.9\%$, Sigma Aldrich), citrate-stabilized 670 nm-resonant GNRs (50 nm in length, 19 nm in diameter, 1.14×10^{13} particles/mL, 2 mM citrate buffer, nanoCompix), phosphate-buffered saline (PBS) (Tablet, Sigma Aldrich), squalane (99%, Sigma Aldrich) and milli-Q (mQ) water (resistivity 18.2 M/cm, Millipore Simplicity 185), pentane (Van Water & Rogers, VWR, Radnor, PA, USA).

2.2. Synthesizing Bulk Volume of Hydrogel With and Without Gold Nanoparticles

Two stock solutions were prepared and used later for making pre-gel samples. First stock solution was prepared by dissolving AAM and BIS in PBS solution (30 wt% AAM-BIS and 2 mol% BIS). Second stock solution was prepared by dissolving AAM, AAC, and BIS in PBS solution (30 wt% AAM-AAC-BIS, 2 mol% BIS, molar ratio AAM/AAC = 1/2). The stock solutions were stored at 4 °C until further use for up to two weeks. 10 wt% AAM-BIS and 10 wt% AAM-AAC-BIS pre-gel samples were further prepared by diluting the stock solutions with PBS or GNP solution. Four types of pre-gel samples were made; (1) 10 wt% AAM-BIS in PBS solution; (2) 10 wt% AAM-BIS in GNP solution; (3) 10 wt% AAM-AAC-BIS in PBS solution; (4) 10 wt% AAM-AAC-BIS in GNP solution. The pre-gel samples were stored at 4 °C until further use for up to 24 hours. Next, 1-hydroxycyclohexyl phenyl ketone photoinitiator (PI) was diluted in DMSO (0.01 M). Before photopolymerization, the PI-DMSO solution was added to the pre-gel sample (PI/pre-gel = 31/2000). 0.2 mL pre-gel with PI solution was further transferred by a pipette (Finnpipette F2, Thermo Scientific, VWR) to a glass rod surrounded by 1.3 mL squalane-PI oil (2.7 mg/mL PI) in a 1.5 mL Eppendorf tube (211-2164, VWR) as shown in Figure 1. The deposited pre-gel with PI solution on glass rod forms a hemispherical shape since it is immiscible in the squalane-PI oil. The hemispherical pre-gel with PI on the glass rod was illuminated with light at 365 nm by using a 400 μ m multimode OF (QP400-2-UV-VIS, Ocean Optics, Dunedin, FL, USA) coupled to a LED (M365F1, Thorlabs, Newton, NJ, USA). The pre-gel with PI was photopolymerized for 15 minutes, subsequently transferred to pentane to remove impurities for 5 s and stored in PBS solution (pH of PBS adjusted to 4.5 for AAM-AAC-BIS hydrogel) until further use.

2.3. Preparing Hydrogels for Scanning Electron Microscopy

The materials used for preparing hydrogels for SEM are as follows; 2.5% glutaraldehyde (Chemi-Teknik AS, Oslo, Norway) in Sorensens phosphate buffer (SPBS) (pH 7.2), ethanol (absolute alcohol, Antibac AS, Oslo, Norway), and hexamethyldisilazane (HMDS) ($\geq 99\%$, Sigma-Aldrich).

The AAM-BIS and AAM-AAC-BIS hydrogels, with and without GNP, were fixated in 2.5 % glutaraldehyde (Chemi-Teknik AS, Oslo, Norway) in SPBS (pH 7.2) for 2 hours at room temperature and left for 12 hours at 4 °C. After fixation, the hydrogels were washed two times for 5 minutes in SPBS. The pre-gel samples were further cut in half by a razor where one half was prepared for the critical point drying technique (CPD) (Polaron) and the other half was prepared for drying using HMDS solvent. Before drying, the hydrogels were dehydrated with increased ethanol concentrations of 10, 25, 50, 70, 90 and 100%, 5 minutes for each concentration. Further, one gel serie from the razor cutting was transferred to the CPD, while the other gel serie from the razor cutting was transferred to HMDS



Figure 1: Image of Eppendorf tube with glass rod inside used for photopolymerizing pre-gel in squalane-PI.

solvent. With the CPD technique, the ethanol was replaced with liquid carbon dioxide and further sublimed entirely. With HMDS solvent, the gel was transferred first to 50% HMDS diluted in ethanol for 20 min and then transferred to 100% HMDS. Two times for 20 min each round. The hydrogels in HMDS solvent were further dried overnight in a desiccator. The dried samples were cut or cracked in two by a razor, mounted on pins using double sided carbon tape, and sputter-coated (E5100, Polaron) with 30 nm of gold-palladium (Au/Pd). The samples were examined using a scanning electron microscope (Teneo Volumscope, Thermo Scientific Fisher), using Everhart-Thornley detector (ETD) in SE mode and Trinity detector (T1) in BSE mode.

2.4. Preparing GNPs on Carbon Tape for Scanning Electron Microscopy

An aliquot of GNP solution was transferred to double sided carbon tape, dried overnight in a desiccator and sputter coated with 30 nm gold-palladium (Au/Pd).

3. Results and Discussion

3.1. Morphology of AAM-BIS Hydrogel With and Without GNRs

SEM images from CPD and HMDS dried hydrogels with GNRs in secondary electron (SE) and backscattered electron (BSE) mode are shown in Figure 2. Figure 2a and 2b shows hydrogels prepared with CPD, without and with GNRs in SE mode, respectively. In the SE mode SEM image of GNR-hydrogel in Figure 2b, no small-sized high contrast features can be observed. We may expect to observe high-density materials as high contrast features such as from NMNPs in BSE mode at high electron beam voltages, since high-density materials have more substantial electron-backscattering intensities than low-density materials.

SEM images of HMDS dried hydrogels in BSE mode, with and without GNRs, are shown in Figure 2c and 2d, respectively. The pore sizes of the HMDS dried hydrogels are comparable to the SEM images of CPD hydrogels. This shows that using HMDS for drying hydrogels for SEM imaging may serve as a suitable alternative to the CPD technique. The embedding of GNRs in the hydrogel have minor influence on the polymer network structure. In BSE mode, there are high contrast features along the edges of the pore structures in Figure 2d (indicated with white arrows), which could represent dense materials such as NMNPs. The high contrast features are similar for hydrogel, with and without GNRs, which makes the quantizing of the distribution of GNRs in the polymer network uncertain. The small-sized contrast features shown with white arrows in Figure 2d could be characterized as distributed GNRs, but may also be difficult to distinguish from artifacts associated to the sample preparation [74, 75]. Figure 3 shows SEM images of CPD and HMDS dried hydrogels with GNRs at a higher magnification than the SEM-images in Figure 2. SEM image of GNR solution dried on carbon tape in Figure 3b is presented as a reference sample. The GNRs in

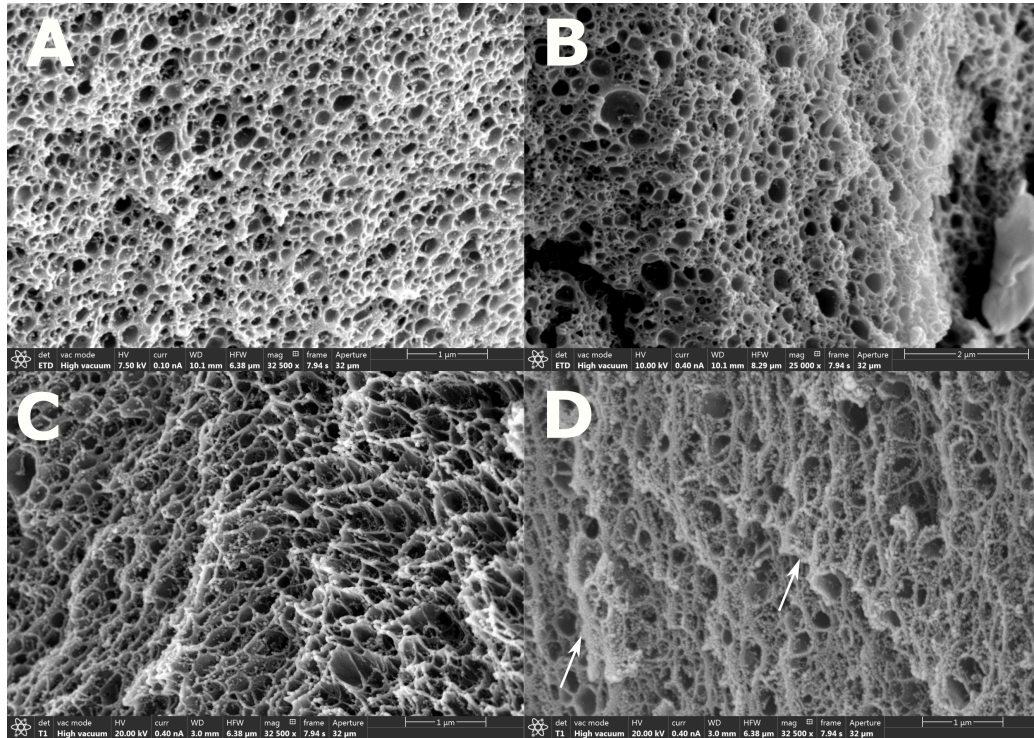


Figure 2: (a) SEM image of CPD AAM-BIS hydrogel without GNRs in SE mode; (b) SEM image of CPD AAM-BIS hydrogel with GNRs in SE mode; (c) SEM image of HMDS dried AAM-BIS hydrogel without GNP in BSE mode; (d) SEM image of HMDS dried AAM-BIS hydrogel with GNP in BSE mode. Note that the scalebar in (b) is different from the other images. The white arrows clarifies the small-sized high contrast features observed that could indicate distributed GNRs.

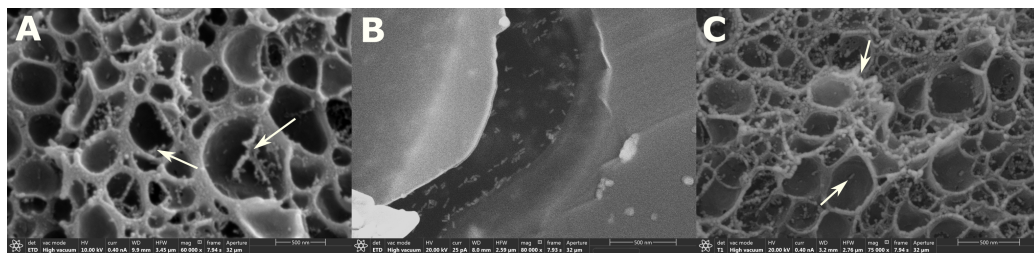


Figure 3: (a) SEM image of CPD AAM-BIS hydrogel with GNRs in SE mode; (b) Air-dried GNR solution on carbon tape in SE mode for comparison with SEM images of GNP-hydrogels; (c) SEM image of HMDS dried AAM-BIS hydrogel with GNP in BSE mode. The white arrows clarifies the small-sized high contrast features observed that could indicate distributed GNRs.

Figure 3b have length and width similar to the specifications received from the producer and is used for comparison to the small-sized high contrast features observable in Figure 3a and 3c (shown with white arrows). The pore structure of the hydrogel dried with CPD technique is similar to the HMDS dried GNR-hydrogel, which again demonstrates that drying with HMDS may serve as a useful alternative to the CPD technique. The BSE mode SEM image in Figure 3c shows few small-sized high contrast features (indicated with white arrows), which could indicate the presence

of GNRs since they are denser than the polymer network. The dimension of the contrast features in Figure 3a and 3c are comparable to the size of GNRs in Figure 3b, but difficult to quantize with respect to estimating the particle distributions. The contrast of NMNPs in gel-like samples may be improved by omitting the metal sample coating and by including highly conductive sample holders instead [76]. The detection of SE and BSE can also be combined to obtain density dependent contrasts that highlights the high densities areas in the image [77].

3.2. Morphology of AAM-AAC-BIS Hydrogel With and Without GNRs

SEM images of CPD and HMDS dried hydrogels, with and without GNRs, in SE and BSE mode are shown in Figure 4. Figure 4a and 4b shows CPD hydrogels without and with GNRs in SE mode, respectively. Some collapsing

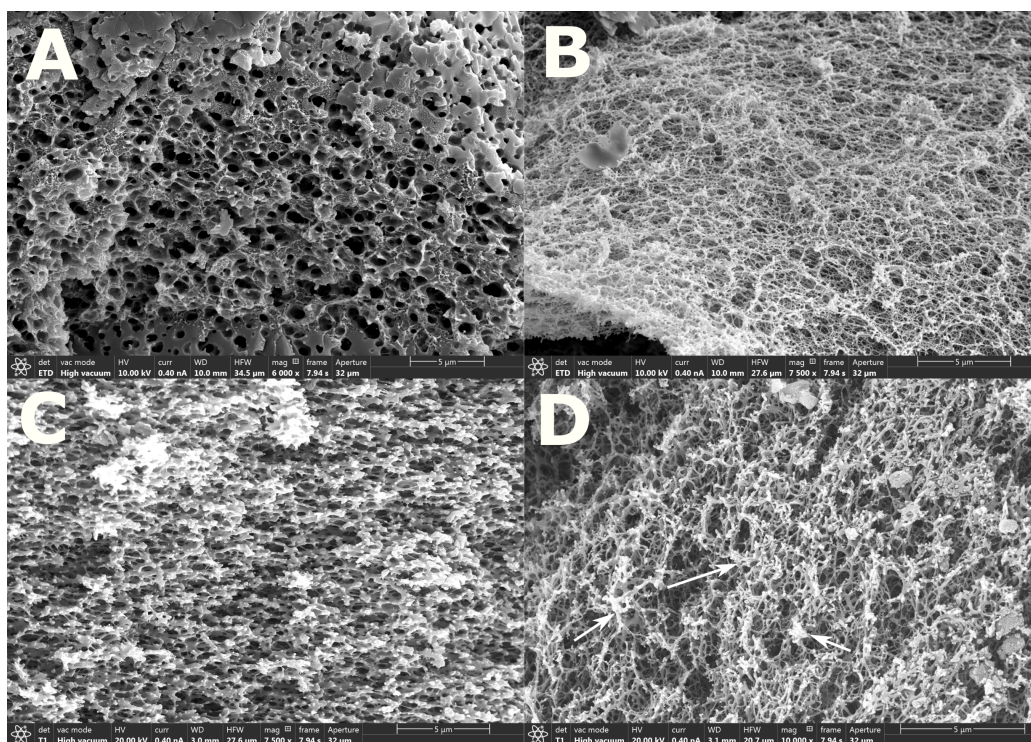


Figure 4: (a) SEM image of CPD AAM-AAC-BIS hydrogel without GNRs in SE mode; (b) SEM image of CPD AAM-AAC-BIS hydrogel with GNRs in SE mode; (c) SEM image of HMDS dried AAM-AAC-BIS hydrogel without GNP in BSE mode; (d) SEM image of HMDS dried AAM-AAC-BIS hydrogel with GNP in BSE mode. Note that the scalebar in the images is 5 μ m. The white arrows clarifies the small-sized high contrast features observed that could indicate distributed GNRs.

characteristics can be observed for the hydrogel without GNRs. The collapse could be a result of insufficient dehydration considering that the AAM-AAC-BIS hydrogels have 2/1 (AAC/AAM) molar ratio of hydrophilic anionic AAC co-monomers. The hydrogels may have been rehydrated due to the humidity at room temperature while transferring it to the CPD. In the CPD, ethanol will only exchange efficiently with liquid carbon dioxide. A partly rehydrated hydrogel will be more susceptible to a collapse. For hydrogels with GNRs, there are fewer collapse characteristics. The GNR-hydrogel exhibits rather a highly entropic polymer network. The complexity of the polymer network could be due to the hydrophilicity of the AAM-AAC-BIS hydrogels. The anionic AAC co-monomer may contribute to absorb a more substantial fraction of water in the small pores of the polymer network. The preparation methods may also influence the pore structures as discussed in Section 3.3 [52, 53].

Figure 4c and 4d shows HMDS dried hydrogels without and with GNRs in BSE mode, respectively. HMDS dried hydrogel without GNRs shows collapsed networks similar to the CPD hydrogel without GNRs. The hydrogel may have been rehydrated while substituting ethanol with HMDS. HMDS may also only exchange efficiently with ethanol. This might indicate that the HMDS dried hydrogel is also susceptible to collapse due to rehydration as with the CPD dried hydrogel. For HMDS dried hydrogel with GNRs, the polymer network is highly entropic with few collapsing features. The complexity of the polymer network could be due to the hydrophilicity of the AAM-AAC-BIS anionic hydrogel.

As for the results obtained in Section 3.1 there are high contrast features along the edges of the polymer networks in Figure 4d in BSE mode (indicated with white arrows), which could represent dense materials. The high contrast features are similar for hydrogel, with and without GNRs, and makes the quantizing of the distribution of GNRs in the polymer network uncertain. The sizes and shapes of the contrast features could be a result of the artifacts introduced from the sample preparations [74, 75].

Figure 5 shows SEM images of CPD and HMDS dried hydrogels with GNRs at a higher magnification than the SEM images in Figure 4. SEM image of GNR solution dried on carbon tape in Figure 5b is presented as a reference sample and used for comparison to the small-sized high contrast features observable in Figure 5a and 5c shown with white arrows. The branched and highly entropic polymer networks of AAM-AAC-BIS GNR-hydrogels

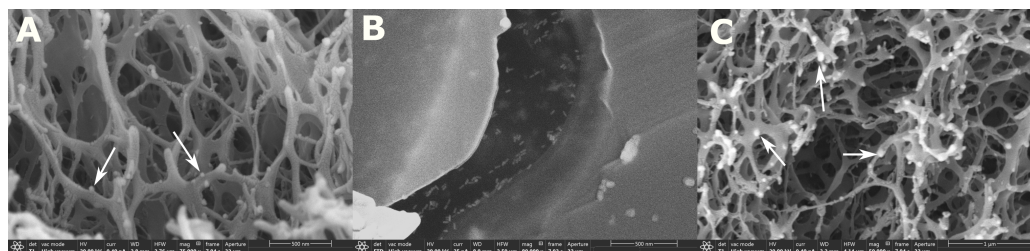


Figure 5: (a) SEM image of CPD AAM-AAC-BIS hydrogel with GNRs in BSE mode; (b) Air-dried GNR solution on carbon tape in SE mode for comparison with SEM images of GNP-hydrogels; (c) SEM image of HMDS dried AAM-AAC-BIS hydrogel with GNP in BSE mode. Note that the scalebar in (c) is different from the other images. The white arrows clarifies the small-sized high contrast features observed that could indicate distributed GNRs.

can be qualitatively assessed in Figure 5a and 5c. The pore size and shapes are more irregular for AAM-AAC-BIS GNR-hydrogels as compared to the AAM-BIS hydrogels. The irregular pore size and shapes of AAM-AAC-BIS GNR-hydrogels could be due to the hydrophilic nature of the anionic polymer network as discussed above.

The small-contrast features in Figure 5a and 5c (shown with white arrows) are similar results to those in Figure 3a and 3c which could indicate the presence of GNRs since they are denser than the polymer network. As discussed for the results in Figure 3, these small-sized contrast features are difficult to quantize as a distribution of GNRs due to the low contrast intensity, but could be improved by using results from [76, 77].

3.3. Influence of Fixation, Dehydration and Drying on the Morphological Structures of the GNR-Hydrogel

The AAM-BIS hydrogel is sensitive towards ethanol concentrations, but insensitive to pH for the solutions used in this paper [78]. The fixation with glutaraldehyde at pH 7.2 will, therefore, introduce small changes in the hydrogel swelling equilibrium with respect to changes in pore size and shapes. For the dehydration with ethanol, the hydrogel will decrease in size, which can be assumed to result in considerable changes in size and shape of pores of the polymer network. The pore sizes observed in Figure 2 and 3 are, therefore, likely to be smaller than the pore size of the hydrogel in a hydrated state. The dried hydrogels may also in most cases exhibit an uncertain degree of collapsing characteristics [52, 53, 57, 58, 79]. Any degree of collapsing characteristics of the hydrogel may result in a close packing of the GNRs. The amount of close-packed GNRs in the BSE mode SEM images were difficult to characterize in our results due to the low contrast of GNRs. Other microscopy techniques may be used to study its native hydrated state such as by using cryogenic or environmental SEM that omits the fixation, dehydration and the drying [50, 51].

The AAM-AAC-BIS hydrogel is sensitive to both ethanol and pH [78, 80]. The fixation with glutaraldehyde at pH 7.2 causes the hydrogel to swell significantly due to the deprotonation of the AAC making the polymer network

highly anionic. This may pose strain on the polymer network beyond the elastic limit. The irregular shapes of the polymer network in Figure 4b and 4d can be caused by the swelling of the hydrogel. The dehydration of the hydrogel with ethanol causes the hydrogel to contract significantly. The pore size observed in Figure 4 and 5 is assumed to be smaller than the pore size of the hydrogel in its native hydrated state.

4. Conclusions

The morphology of low weight percentage polyacrylamide and poly(acrylamide-co-acrylic acid) hydrogels, with and without GNRs, have been characterized by using conventional SEM. A comparison was made between the CPD and HMDS drying methods of hydrogels. Results from CPD and HMDS techniques shows to have comparable pore structures. Using HMDS solvent for drying may serve as a suitable alternative to the CPD technique. The HMDS technique is a cost-effective substitution of the CPD technique that omits equipment use as well as less time consuming. The pores of poly(acrylamide-co-acrylic acid) hydrogels shows to have irregular structures while the pores of polyacrylamide hydrogels shows to have slightly more regular structures. This difference is assumed to be due to the more substantial hydrophilicity of poly(acrylamide-co-acrylic acid) anionic hydrogel. The pore structures of the dehydrated and dried hydrogels are likely smaller than the pore structures of hydrated hydrogels due to the water exchange with ethanol in the dehydration. The effect of dehydrating and drying hydrogels may in most cases exhibit an uncertain degree of collapsing characteristics [52, 53, 57, 58, 79]. By comparing the morphology of dried hydrogels with cryoSEM or environmental SEM images of hydrated hydrogels [50, 51] it is possible to estimate the presence of these collapsing features.

Small-sized high contrast features can be observed from the BSE mode SEM images of GNR-hydrogels, which may indicate the presence of GNRs since they are denser than the polymer network. The contrast of these features were not significant enough for distinguishing them from artifacts associated to the sample preparations [74, 75]. The contrast of NMNPs in gel-like samples may be improved by omitting the sample coating and by including highly conductive sample holders instead [76], or by using both SE and BSE detectors to obtain density dependent contrasts that highlights the high densities areas in the image [77]. Any hydrogel collapse may result in close packing of the GNRs. The amount of close-packed GNRs in the BSE mode SEM images were difficult to characterize in our results due to the low contrast of the GNRs.

Future work will consist of developing methods for enhancing the contrast of high-density materials in a low-density matrix for conventional SEM imaging. Furthermore, volume-imaging methods such as the FIB-SEM or the SBFSEM techniques will be used to map the distribution of metal nanoparticles in hydrogels.

References

- [1] Todd R. Hoare, Daniel S. Kohane, Hydrogels in drug delivery: Progress and challenges, *Polymer* 48 (8) (2008) 1993–2007. doi:<http://dx.doi.org/10.1016/j.polymer.2008.01.027>.
- [2] B. RATNER, A. HOFFMAN, Synthetic Hydrogels for Biomedical Applications, in: *Hydrogels for Medical and Related Applications*, Vol. 31 of ACS Symposium Series, AMERICAN CHEMICAL SOCIETY, 1976, p. 1. doi:<https://doi.org/10.1021/bk-1976-0031.ch001>. URL <https://doi.org/10.1021/bk-1976-0031.ch001>
- [3] E. Caló, V. V. Khutoryanskiy, Biomedical applications of hydrogels: A review of patents and commercial products, *European Polymer Journal* 65 (2015) 252–267. doi:<https://doi.org/10.1016/j.eurpolymj.2014.11.024>. URL <http://www.sciencedirect.com/science/article/pii/S0014305714004091>
- [4] M. Xie, M. Ø. Olderoy, J.-P. Andreassen, S. M. Selbach, B. L. Strand, P. Sikorski, Alginate-controlled formation of nanoscale calcium carbonate and hydroxyapatite mineral phase within hydrogel networks, *Acta Biomaterialia* 6 (9) (2010) 3665–3675. doi:<https://doi.org/10.1016/j.actbio.2010.03.034>. URL <http://www.sciencedirect.com/science/article/pii/S1742706110001601>
- [5] K. Gawel, D. Barriet, M. Sletmoen, B. T. Stokke, Responsive Hydrogels for Label-Free signal transduction within biosensors (2010). doi:[10.3390/s100504381](https://doi.org/10.3390/s100504381).
- [6] K. Y. Lee, D. J. Mooney, Hydrogels for Tissue Engineering, *Chemical Reviews* 101 (7) (2001) 1869–1880. doi:[10.1021/cr000108x](https://doi.org/10.1021/cr000108x). URL <https://doi.org/10.1021/cr000108x>
- [7] J. H. Holtz, S. A. Asher, Polymerized colloidal crystal hydrogel films as intelligent chemical sensing materials, *Nature* 389 (1997) 829. URL <http://dx.doi.org/10.1038/39834> <http://10.0.4.14/39834>
- [8] V. L. Alexeev, A. C. Sharma, A. V. Goponenko, S. Das, I. K. Lednev, C. S. Wilcox, D. N. Finegold, S. A. Asher, High Ionic Strength Glucose-Sensing Photonic Crystal, *Analytical Chemistry* 75 (10) (2003) 2316–2323. doi:[10.1021/ac030021m](https://doi.org/10.1021/ac030021m). URL <https://doi.org/10.1021/ac030021m>

- [9] S. Goenka, V. Sant, S. Sant, Graphene-based nanomaterials for drug delivery and tissue engineering, *J Control Release* 173 (1) (2014) 75–88. doi:10.1016/j.jconrel.2013.10.017.
URL <http://www.sciencedirect.com/science/article/pii/S016836591300847X>
- [10] J. N. Tiwari, K. Mahesh, N. H. Le, K. C. Kemp, R. Timilsina, R. N. Tiwari, K. S. Kim, Reduced graphene oxide-based hydrogels for the efficient capture of dye pollutants from aqueous solutions, *Carbon* 56 (2013) 173–182. doi:10.1016/j.carbon.2013.01.001.
URL <http://www.sciencedirect.com/science/article/pii/S0008622313000158>
- [11] B. A. Firestone, R. A. Siegel, Dynamic pH-dependent swelling properties of a hydrophobic polyelectrolyte gel, *Polymer communications Guildford* 29 (7) (1988) 204–208.
URL <papers://fae851fc-58bd-493b-8b72-2955f37392a5/Paper/p6750>
- [12] L. Brannon-Peppas, N. A. Peppas, Dynamics and equilibrium swelling behaviour of pH-sensitive hydrogels containing 2-hydroxy methacrylate, *Biomaterials* 11 (9) (1990) 635–644. doi:https://doi.org/10.1016/0142-9612(90)90021-H.
URL <http://www.sciencedirect.com/science/article/pii/014296129090021H>
- [13] G. R. Deen, C. H. Mah, Influence of external stimuli on the network properties of cationic poly(N-acryloyl-N'-propyl piperazine) hydrogels, *Polymer (United Kingdom)* 89 (2016) 55–68. doi:10.1016/j.polymer.2016.02.027.
- [14] J. H. Kim, S. B. Lee, S. J. Kim, Y. M. Lee, Rapid temperature/pH response of porous alginate-g-poly(N-isopropylacrylamide) hydrogels, *Polymer* 43 (26) (2002) 7549–7558. doi:10.1016/S0032-3861(02)00675-4.
URL <https://www.sciencedirect.com/science/article/pii/S0032386102006754>
- [15] S. J. Lue, C.-H. Chen, C.-M. Shih, Tuning of Lower Critical Solution Temperature (LCST) of Poly(N-Isopropylacrylamide-co-Acrylic acid) Hydrogels, *Journal of Macromolecular Science, Part B* 50 (3) (2011) 563–579. doi:10.1080/00222341003784550.
URL <http://www.tandfonline.com/doi/abs/10.1080/00222341003784550>
- [16] T. Tanaka, Collapse of gels and the critical endpoint, *Physical Review Letters* 40 (12) (1978) 820–823. doi:10.1103/PhysRevLett.40.820.
URL <https://link.aps.org/doi/10.1103/PhysRevLett.40.820>
- [17] J. Rička, T. Tanaka, Swelling of Ionic Gels: Quantitative Performance of the Donnan Theory, *Macromolecules* 17 (12) (1984) 2916–2921. doi:10.1021/ma00142a081.
URL <https://doi.org/10.1021/ma00142a081>
- [18] T. G. Park, A. S. Hoffman, Sodium Chloride-Induced Phase Transition in Nonionic Poly(N-isopropylacrylamide) Gel, *Macromolecules* 26 (19) (1993) 5045–5048. doi:10.1021/ma00071a010.
URL <https://doi.org/10.1021/ma00071a010>
- [19] L. Brannon-Peppas, N. A. Peppas, Time-Dependent Response of Ionic Polymer Networks to Ph and Ionic-Strength Changes, *International Journal of Pharmaceutics* 70 (1) (1991) 53–57. doi:https://doi.org/10.1016/0378-5173(91)90163-I.
- [20] T. Miyata, N. Asami, T. Uragami, A reversibly antigen-responsive hydrogel, *Nature* 399 (1999) 766.
- [21] M. Takashi, N. Asami, T. Uragami, Structural design of stimuli-responsive bioconjugated hydrogels that respond to a target antigen, *Journal of Polymer Science, Part B: Polymer Physics* 47 (21) (2009) 2144–2157. arXiv:0406218, doi:10.1002/polb.21812.
URL <http://dx.doi.org/10.1002/polb.21812>
- [22] T. Miyata, N. Asami, T. Uragami, Preparation of an antigen-sensitive hydrogel using antigen-antibody bindings, *Macromolecules* 32 (6) (1999) 2082–2084. doi:10.1021/ma981659g.
- [23] T. Miyata, M. Jige, T. Nakaminami, T. Uragami, Tumor marker-responsive behavior of gels prepared by biomolecular imprinting., *Proceedings of the National Academy of Sciences of the United States of America* 103 (5) (2006) 1190–1193. doi:10.1073/pnas.0506786103.
- [24] S. Tierney, B. M. H. Falch, D. R. Hjelm, B. T. Stokke, Determination of Glucose Levels Using a Functionalized Hydrogel Optical Fiber Biosensor: Toward Continuous Monitoring of Blood Glucose in Vivo, *Anal. Chem.* 81 (9) (2009) 3630–3636. doi:10.1021/ac900019k.
URL <http://dx.doi.org/10.1021/ac900019k>
- [25] S. H. Bjørnøy, D. C. Bassett, S. Ucar, J. P. Andreassen, P. Sikorski, Controlled mineralisation and recrystallisation of brushite within alginate hydrogels, *Biomedical Materials (Bristol)* 11 (1) (2016) 15013. doi:10.1088/1748-6041/11/1/015013.
URL <http://stacks.iop.org/1748-605X/11/i=1/a=015013>
- [26] V. Thomas, M. Namdeo, Y. Murali Mohan, S. K. Bajpai, M. Bajpai, Review on Polymer, Hydrogel and Microgel Metal Nanocomposites: A Facile Nanotechnological Approach, *Journal of Macromolecular Science, Part A* 45 (1) (2007) 107–119. doi:10.1080/10601320701683470.
URL <https://doi.org/10.1080/10601320701683470>
- [27] Y. Murali Mohan, K. Lee, T. Premkumar, K. E. Geckeler, Hydrogel networks as nanoreactors: A novel approach to silver nanoparticles for antibacterial applications, *Polymer* 48 (1) (2007) 158–164. doi:https://doi.org/10.1016/j.polymer.2006.10.045.
URL <http://www.sciencedirect.com/science/article/pii/S0032386106012080>
- [28] A. Das, A. Kumar, N. B. Patil, C. Viswanathan, D. Ghosh, Preparation and characterization of silver nanoparticle loaded amorphous hydrogel of carboxymethylcellulose for infected wounds, *Carbohydrate Polymers* 130 (2015) 254–261. doi:https://doi.org/10.1016/j.carbpol.2015.03.082.
URL <http://www.sciencedirect.com/science/article/pii/S0144861715003021>
- [29] D. Liang, Z. Lu, H. Yang, J. Gao, R. Chen, Novel Asymmetric Wetttable AgNPs/Chitosan Wound Dressing: In Vitro and In Vivo Evaluation, *ACS Applied Materials & Interfaces* 8 (6) (2016) 3958–3968. doi:10.1021/acsami.5b11160.
URL <https://doi.org/10.1021/acsami.5b11160>
- [30] I. Tokarev, I. Tokareva, V. Gopishetty, E. Katz, S. Minko, Specific Biochemical-to-Optical Signal Transduction by Responsive Thin Hydrogel Films Loaded with Noble Metal Nanoparticles, *Advanced Materials* 22 (12) (2010) 1412–1416. doi:10.1002/adma.200903456.
URL <http://dx.doi.org/10.1002/adma.200903456>
- [31] R. G. Deen, V. Chua, Synthesis and Properties of New Stimuli Responsive Nanocomposite Hydrogels Containing Silver Nanoparticles (2015). doi:10.3390/gels1010117.
- [32] A. Politano, P. Argurio, G. Di Profio, V. Sanna, A. Cupolillo, S. Chakraborty, H. A. Arafat, E. Curcio, Photothermal Membrane Distillation for Seawater Desalination, *Advanced Materials* 29 (2) (2017) 1603504. arXiv:9809069v1, doi:10.1002/adma.201603504.
URL <https://doi.org/10.1002/adma.201603504>

- [33] A. Politano, A. Cupolillo, G. Di Profio, H. A. Arafat, G. Chiarello, E. Curcio, When plasmonics meets membrane technology, *Journal of Physics Condensed Matter* 28 (36) (2016) 363003. doi:10.1088/0953-8984/28/36/363003
URL <http://stacks.iop.org/0953-8984/28/i=36/a=363003>
- [34] A. Politano, G. Di Profio, E. Fontananova, V. Sanna, A. Cupolillo, E. Curcio, Overcoming temperature polarization in membrane distillation by thermoplasmonic effects activated by Ag nanofillers in polymeric membranes, *Desalination* doi:10.1016/j.desal.2018.03.006.
URL <http://www.sciencedirect.com/science/article/pii/S0011916417321707>
- [35] U. Calabria, A. Politano, U. Calabria, N. Scaramuzza, U. Calabria, Tailoring the physical properties of nanocomposite films by the insertion of graphene and metal nanoparticles *Composites : Part B, Composites Part B* 60 (2014) 29–35. doi:<https://doi.org/10.1016/j.compositesb.2013.12.011>.
URL <http://www.sciencedirect.com/science/article/pii/S1359836813007129>
- [36] K. M. Mayer, J. H. Hafner, Localized Surface Plasmon Resonance Sensors, *Chem. Rev.* 111 (6) (2011) 3828–3857. doi:10.1021/cr100313v.
URL <http://dx.doi.org/10.1021/cr100313v>
- [37] S. A. Maier, *Plasmonics: Fundamentals and applications*, Springer Science & Business Media, 2007. arXiv:arXiv:1011.1669v3, doi:10.1007/0-387-37825-1.
- [38] V. Klimov, *Nanoplasmonics*, Pan Stanford Publishing, 2014.
URL <https://books.google.no/books?id=KqfSBQAAQBAJ>
- [39] T. Endo, K. Kerman, N. Nagatani, H. M. Hiepa, D.-K. Kim, Y. Yonezawa, K. Nakano, E. Tamiya, Multiple Label-Free Detection of Antigen-Antibody Reaction Using Localized Surface Plasmon Resonance-Based Core-Shell Structured Nanoparticle Layer Nanochip, *Analytical Chemistry* 78 (18) (2006) 6465–6475. doi:10.1021/ac0608321.
URL <https://doi.org/10.1021/ac0608321>
- [40] M.-C. Estevez, M. A. Otte, B. Sepulveda, L. M. Lechuga, Trends and challenges of refractometric nanoplasmonic biosensors: A review, *Analytica Chimica Acta* 806 (2014) 55–73. doi:<https://doi.org/10.1016/j.aca.2013.10.048>.
URL <http://www.sciencedirect.com/science/article/pii/S0003267013013913>
- [41] E. S. Gil, S. M. Hudson, Stimuli-responsive polymers and their bioconjugates, *Progress in polymer science* 29 (12) (2004) 1173–1222.
- [42] K. L. Kelly, E. Coronado, L. L. Zhao, G. C. Schatz, The optical properties of metal nanoparticles: The influence of size, shape, and dielectric environment, *Journal of Physical Chemistry B* 107 (3) (2003) 668–677. arXiv:NIHMS150003, doi:10.1021/jp026731y.
URL <https://doi.org/10.1021/jp026731y>
- [43] P. K. Jain, M. A. El-Sayed, Plasmonic coupling in noble metal nanostructures, *Chemical Physics Letters* 487 (4&6) (2010) 153–164.
URL <http://www.sciencedirect.com/science/article/pii/S0009261410001193>
- [44] P. K. Jain, S. Eustis, M. A. El-Sayed, Plasmon Coupling in Nanorod Assemblies: Optical Absorption, Discrete Dipole Approximation Simulation, and Exciton-Coupling Model, *The Journal of Physical Chemistry B* 110 (37) (2006) 18243–18253. doi:10.1021/jp063879z.
URL <http://dx.doi.org/10.1021/jp063879z>
- [45] P. K. Jain, W. Huang, M. A. El-Sayed, On the universal scaling behavior of the distance decay of plasmon coupling in metal nanoparticle pairs: A plasmon ruler equation, *Nano Letters* 7 (7) (2007) 2080–2088. arXiv:1106.1690, doi:10.1021/nl071008a.
URL <https://doi.org/10.1021/nl071008a>
- [46] U. Kreibig, M. Vollmer, *Optical Properties of Metal Clusters*, Vol. 25, Springer Science & Business Media, 1995. arXiv:arXiv:1011.1669v3, doi:10.1007/978-3-662-09109-8.
URL <http://link.springer.com/10.1007/978-3-662-09109-8>
- [47] H. I. Muri, D. R. Hjelme, LSPR coupling and distribution of interparticle distances in hydrogel on optical fiber end face, *Sensors (Switzerland)* 17 (12) (2017) 2723. doi:10.3390/s17122723.
URL <http://www.mdpi.com/1424-8220/17/12/2723>
- [48] H. I. D. I. H. Muri, A. Bano, D. R. D. Hjelme, A Single-Point, Multiparameter, Fiber Optic Sensor Based on a Combination of Interferometry and LSPR, *Journal of Lightwave Technology* 36 (4) (2018) 1159–1167. doi:10.1109/JLT.2018.2791722.
- [49] H. I. Muri, A. Bano, D. R. D. Hjelme, LSPR and Interferometric Sensor Modalities Combined Using a Double-Clad Optical Fiber, *Sensors* 18 (1) (2018) 187. doi:10.3390/s18010187.
URL <http://www.mdpi.com/1424-8220/18/1/187>
- [50] F. M. Plieva, M. Karlsson, M.-R. Aguilar, D. Gomez, S. Mikhailovsky, I. Y. Galaev', Pore structure in supermacroporous polyacrylamide based cryogels, *Soft Matter* 1 (4) (2005) 303–309.
URL <http://dx.doi.org/10.1039/B510010K>
- [51] J. Zhang, N. A. Peppas, Morphology of poly(methacrylic acid)/poly(N-isopropyl acrylamide) interpenetrating polymeric networks, *Journal of Biomaterials Science, Polymer Edition* 13 (5) (2002) 511–525. doi:10.1163/15685620260178373.
URL <http://dx.doi.org/10.1163/15685620260178373>
- [52] S.-Y. Lin, K.-S. Chen, L. Run-Chu, Drying methods affecting the particle sizes, phase transition, deswelling/reswelling processes and morphology of poly(N-isopropylacrylamide) microgel beads, *Polymer* 40 (23) (1999) 6307–6312. doi:[https://doi.org/10.1016/S0032-3861\(98\)00872-6](https://doi.org/10.1016/S0032-3861(98)00872-6).
URL <http://www.sciencedirect.com/science/article/pii/S0032386198008726>
- [53] R. Röchel, M. D. Brager, Scanning electron microscopic observations of polyacrylamide gels, *Analytical Biochemistry* 68 (2) (1975) 415–428. doi:[https://doi.org/10.1016/0003-2697\(75\)90637-5](https://doi.org/10.1016/0003-2697(75)90637-5).
URL <http://www.sciencedirect.com/science/article/pii/0003269775906375>
- [54] X.-Z. Zhang, Y.-Y. Yang, T.-S. Chung, K.-X. Ma, Preparation and Characterization of Fast Response Macroporous Poly(N-isopropylacrylamide) Hydrogels, *Langmuir* 17 (20) (2001) 6094–6099. doi:10.1021/la010105v.
URL <https://doi.org/10.1021/la010105v>
- [55] F. M. Plieva, I. N. Savina, S. Deraz, J. Andersson, I. Y. Galaev, B. Mattiasson, Characterization of supermacroporous monolithic polyacrylamide based matrices designed for chromatography of bioparticles, *Journal of Chromatography B* 807 (1) (2004) 129–137. doi:<https://doi.org/10.1016/j.jchromb.2004.01.050>.

- URL <http://www.sciencedirect.com/science/article/pii/S1570023204001126>
- [56] I. N. Savina, B. Mattiasson, I. Y. Galaev, Graft polymerization of acrylic acid onto macroporous polyacrylamide gel (cryogel) initiated by potassium doperiodatocuprate, *Polymer* 46 (23) (2005) 9596–9603. doi:<https://doi.org/10.1016/j.polymer.2005.07.091>.
URL <http://www.sciencedirect.com/science/article/pii/S0032386105011286>
- [57] H. H. Trieu, S. Qutubuddin, Polyvinyl alcohol hydrogels I. Microscopic structure by freeze-etching and critical point drying techniques, *Colloid and Polymer Science* 272 (3) (1994) 301–309. doi:[10.1007/BF00655501](https://doi.org/10.1007/BF00655501).
URL <https://doi.org/10.1007/BF00655501>
- [58] J. Chen, K. Park, Synthesis and characterization of superporous hydrogel composites, *Journal of Controlled Release* 65 (1) (2000) 73–82. doi:[https://doi.org/10.1016/S0168-3659\(99\)00238-2](https://doi.org/10.1016/S0168-3659(99)00238-2).
URL <http://www.sciencedirect.com/science/article/pii/S0168365999002382>
- [59] S. Park, P. S. K. Murthy, S. Park, Y. M. Mohan, W.-G. Koh, Preparation of silver nanoparticle-containing semi-interpenetrating network hydrogels composed of pluronic and poly(acrylamide) with antibacterial property, *Journal of Industrial and Engineering Chemistry* 17 (2) (2011) 293–297. doi:<https://doi.org/10.1016/j.jiec.2011.02.026>.
URL <http://www.sciencedirect.com/science/article/pii/S1226086X1100027X>
- [60] G. Möbus, B. J. Inkson, Nanoscale tomography in materials science, *Materials Today* 10 (12) (2007) 18–25. doi:[https://doi.org/10.1016/S1369-7021\(07\)70304-8](https://doi.org/10.1016/S1369-7021(07)70304-8).
URL <http://www.sciencedirect.com/science/article/pii/S1369702107703048>
- [61] K. Kulawik, P. A. Buffat, A. Kruk, A. M. Wusatowska-sarnek, A. Czyska-filemonowicz, Materials Characterization Imaging and characterization of γ' and γ'' nanoparticles in Inconel 718 by EDX elemental mapping and FIB - SEM tomography, *Materials Characterization* 100 (2015) 74–80. doi:[10.1016/j.matchar.2014.12.012](https://doi.org/10.1016/j.matchar.2014.12.012).
URL <http://dx.doi.org/10.1016/j.matchar.2014.12.012>
- [62] P. Schneider, M. Meier, R. Wepf, R. Müller, Serial FIB/SEM imaging for quantitative 3D assessment of the osteocyte lacuno-canalicular network, *Bone* 49 (2) (2018) 304–311. doi:[10.1016/j.bone.2011.04.005](https://doi.org/10.1016/j.bone.2011.04.005).
URL <http://dx.doi.org/10.1016/j.bone.2011.04.005>
- [63] F. Braet, R. De Zanger, E. Wisse, Drying cells for SEM, AFM and TEM by hexamethyldisilazane: a study on hepatic endothelial cells, *Journal of Microscopy* 186 (1) (1997) 84–87. doi:[10.1046/j.1365-2818.1997.1940755.x](https://doi.org/10.1046/j.1365-2818.1997.1940755.x).
URL <http://dx.doi.org/10.1046/j.1365-2818.1997.1940755.x>
- [64] D. F. Bray, J. Bagu, P. Koegler, Comparison of hexamethyldisilazane (HMDS), Peldri II, and criticalpoint drying methods for scanning electron microscopy of biological specimens, *Microscopy Research and Technique* 26 (6) (1993) 489–495. doi:[10.1002/jemt.1070260603](https://doi.org/10.1002/jemt.1070260603).
URL <https://doi.org/10.1002/jemt.1070260603>
- [65] J. Perdigao, P. Lambrechts, B. Van Meerbeek, G. Vanherle, A. L. Lopes, Field emission SEM comparison of four postfixation drying techniques for human dentin, *Journal of Biomedical Materials Research* 29 (9) (1995) 1111–1120. doi:[10.1002/jbm.820290911](https://doi.org/10.1002/jbm.820290911).
URL <https://doi.org/10.1002/jbm.820290911>
- [66] J. C. Araujo, F. C. Téran, R. A. Oliveira, E. A. Nour, M. A. Montenegro, J. R. Campos, R. F. Vazoller, Comparison of hexamethyldisilazane and critical point drying treatments for SEM analysis of anaerobic biofilms and granular sludge, *Journal of Electron Microscopy* 52 (4) (2003) 429–433. doi:[10.1093/jmicro/52.4.429](https://doi.org/10.1093/jmicro/52.4.429).
URL <http://dx.doi.org/10.1093/jmicro/52.4.429>
- [67] Y. Jusman, S. C. Ng, N. Azuan, A. Osman, Investigation of CPD and HMDS sample preparation techniques for cervical cells indeveloping computer aided screening system based on FE-SEM / EDX, *The Scientific World Journal* 2014.
- [68] N. Annabi, S. Mithieux, A. Weiss, F. Dehghani, The fabrication of elastin-based hydrogels using high pressure CO₂, *Biomaterials* 30 (1) (2009) 1–7. doi:[10.1016/j.biomaterials.2008.09.031](https://doi.org/10.1016/j.biomaterials.2008.09.031).
URL <http://www.sciencedirect.com/science/article/pii/S0142961208006510>
- [69] R. McMahon, M. Hahn, M. Pendleton, E. Ellis, A Simple Preparation Method for Mesh Fibrin Hydrogel Composites for Conventional SEM, *Microscopy and Microanalysis* 16 (S2) (2010) 1030–1031. doi:[10.1017/S1431927610058484](https://doi.org/10.1017/S1431927610058484).
URL <http://www.journals.cambridge.org/abstract.S1431927610058484>
- [70] J. T. Y. Lee, K. L. Chow, SEM sample preparation for cells on 3D scaffolds by freeze-drying and HMDS, *Scanning* 34 (1) (2012) 12–25. doi:[10.1002/sca.20271](https://doi.org/10.1002/sca.20271).
URL <https://doi.org/10.1002/sca.20271>
- [71] Y. M. Yoon, J. S. Lewis, M. R. Carstens, M. Campbell-Thompson, C. H. Wasserfall, M. A. Atkinson, B. G. Keselowsky, A combination hydrogel microparticle-based vaccine prevents type 1 diabetes in non-obese diabetic mice, *Scientific Reports* 5 (2015) 13155. doi:[10.1038/srep13155](https://doi.org/10.1038/srep13155).
URL <http://dx.doi.org/10.1038/srep13155> <http://10.0.4.14/srep13155>
- [72] E. Jurrus, M. Hardy, T. Tasdizen, P. T. Fletcher, P. Koshevoy, C.-B. Chien, W. Denk, R. Whitaker, Axon tracking in serial block-face scanning electron microscopy, *Medical Image Analysis* 13 (1) (2018) 180–188. doi:[10.1016/j.media.2008.05.002](https://doi.org/10.1016/j.media.2008.05.002).
URL <http://dx.doi.org/10.1016/j.media.2008.05.002>
- [73] W. Denk, H. Horstmann, Serial Block-Face Scanning Electron Microscopy to Reconstruct Three-Dimensional Tissue Nanostructure, *PLOS Biology* 2 (11) (2004) e329. doi:[10.1371/journal.pbio.0020329](https://doi.org/10.1371/journal.pbio.0020329).
URL <https://doi.org/10.1371/journal.pbio.0020329>
- [74] A. Mehdizadeh Kashi, K. Tahamanesh, S. Chaichian, M. T. Joghataei, F. Moradi, S. M. Tavangar, A. S. Mousavi Najafabadi, N. Lotfibakhshairesh, S. Pour Beyranvand, A. Fazel Anvari-Yazdi, S. M. Abed, How to Prepare Biological Samples and Live Tissues for Scanning Electron Microscopy (SEM), *Galen Medical Journal*; Vol 3, No 2 (2014): June 2014.
URL <http://www.gmj.ir/index.php/gmj/article/view/267/123>
- [75] B. Little, P. Wagner, R. Ray, R. Pope, R. Scheetz, Biofilms: An ESEM evaluation of artifacts introduced during SEM preparation, *Journal of Industrial Microbiology* 8 (4) (1991) 213–221. doi:[10.1007/BF01576058](https://doi.org/10.1007/BF01576058).
URL <https://doi.org/10.1007/BF01576058>

- [76] A. GOLDSTEIN, Y. SOROKA, M. FRUŠIĆ-ZLOTKIN, I. POPOV, R. KOHEN, High resolution SEM imaging of gold nanoparticles in cells and tissues, *Journal of Microscopy* 256 (3) (2014) 237–247. doi:10.1111/jmi.12179.
URL <http://dx.doi.org/10.1111/jmi.12179>
- [77] S. Bertazzo, E. Gentleman, K. L. Cloyd, A. H. Chester, M. H. Yacoub, M. M. Stevens, Nano-analytical electron microscopy reveals fundamental insights into human cardiovascular tissue calcification, *Nature Materials* 12 (2013) 576. doi:10.1038/NMAT3627.
- [78] K. Bouchal, Z. Sedláková, M. Ilavský, Phase transition in swollen gels, *Polymer Bulletin* 32 (3) (1994) 331–338. doi:10.1007/BF00308545.
URL <https://doi.org/10.1007/BF00308545>
- [79] W.-Y. Yeong, C.-K. Chua, K.-F. Leong, M. Chandrasekaran, M.-W. Lee, Comparison of drying methods in the fabrication of collagen scaffold via indirect rapid prototyping, *Journal of Biomedical Materials Research Part B: Applied Biomaterials* 82B (1) (2007) 260–266. doi:10.1002/jbm.b.30729.
URL <http://dx.doi.org/10.1002/jbm.b.30729>
- [80] M. Shibayama, F. Ikkai, S. Inamoto, S. Nomura, C. C. Han, pH and salt concentration dependence of the microstructure of poly(Nisopropylacrylamide-co-acrylic acid) gels, *The Journal of Chemical Physics* 105 (10) (1996) 4358–4366. doi:10.1063/1.472252.
URL <https://doi.org/10.1063/1.472252>